



**HAL**  
open science

# Optimization of the Ni-YSZ Fuel Electrode for a Better Stability of Solid Oxide Cell

Léa Rorato

► **To cite this version:**

Léa Rorato. Optimization of the Ni-YSZ Fuel Electrode for a Better Stability of Solid Oxide Cell. General Physics [physics.gen-ph]. Université Grenoble Alpes [2020-..], 2024. English. NNT : 2024GRALI013 . tel-04581123

**HAL Id: tel-04581123**

**<https://theses.hal.science/tel-04581123>**

Submitted on 21 May 2024

**HAL** is a multi-disciplinary open access archive for the deposit and dissemination of scientific research documents, whether they are published or not. The documents may come from teaching and research institutions in France or abroad, or from public or private research centers.

L'archive ouverte pluridisciplinaire **HAL**, est destinée au dépôt et à la diffusion de documents scientifiques de niveau recherche, publiés ou non, émanant des établissements d'enseignement et de recherche français ou étrangers, des laboratoires publics ou privés.

THÈSE

Pour obtenir le grade de

## DOCTEUR DE L'UNIVERSITÉ GRENOBLE ALPES

École doctorale : I-MEP2 - Ingénierie - Matériaux, Mécanique, Environnement, Energétique, Procédés, Production

Spécialité : 2MGE - Matériaux, Mécanique, Génie civil, Electrochimie

Unité de recherche : CEA Grenoble / LITEN

### Optimisation des électrodes de Ni-YSZ pour une meilleure stabilité des cellules à oxydes solides

### Optimization of the Ni-YSZ Fuel Electrode for a Better Stability of Solid Oxide Cell

Présentée par :

**Léa RORATO**

#### Direction de thèse :

**Jérôme LAURENCIN**

DIRECTEUR DE RECHERCHE, Université Grenoble Alpes

Directeur de thèse

**Karine COUTURIER**

INGENIEURE CHERCHEURE, Université Grenoble Alpes

Co-encadrante de thèse

#### Rapporteurs :

**Annie LE GAL LA SALLE**

CHARGÉE DE RECHERCHE HDR, CNRS délégation Bretagne et Pays de la Loire

**Armelle RINGUEDE**

DIRECTRICE DE RECHERCHE, CNRS délégation Paris Centre

#### Thèse soutenue publiquement le **14 mars 2024**, devant le jury composé de :

**Laurent DESSEMOND,**

PROFESSEUR DES UNIVERSITÉS, Université Grenoble Alpes

Président

**Jérôme LAURENCIN,**

DIRECTEUR DE RECHERCHE, CEA centre de Grenoble

Directeur de thèse

**Annie LE GAL LA SALLE,**

CHARGÉE DE RECHERCHE HDR, CNRS délégation Bretagne et

Pays de la Loire

Rapporteuse

**Armelle RINGUEDE,**

DIRECTRICE DE RECHERCHE, CNRS délégation Paris Centre

Rapporteuse

**Pascal LENORMAND,**

MAÎTRE DE CONFÉRENCES, Université de Toulouse III - Paul

Sabatier

Examineur

**Fédérico MONACO,**

DOCTEUR EN SCIENCES, CEA centre de Grenoble

Examineur

#### Invités :

**Karine COUTURIER**

INGENIEUR DOCTEUR, CEA-LITEN

**Maxime HUBERT**

DOCTEUR EN SCIENCES, CEA-LITEN





# Remerciements

Ces travaux de thèse ont été réalisés au CEA (Commissariat à l'Énergie Atomique et aux Énergies Alternatives) -Liten de Grenoble au sein du Laboratoire Essais et Systèmes (LES). Je tiens premièrement à remercier Armelle RINGUEDE (CNRS) ainsi que Annie LE GAL LA SALLE (CNRS) d'avoir accepté d'être rapporteure de ce travail. Je remercie également Pascal LENORMAND (CIRIMAT), ainsi que Fédérico MONACO (CEA de Grenoble) d'avoir participé au jury en tant qu'examineur. Enfin, je remercie Laurent DESSEMOND (UGA), pour avoir présidé le jury. Je remercie l'ensemble du jury pour les moments d'échange que nous avons pu avoir lors de la soutenance.

Ce travail de thèse a été possible grâce à l'implication et le support de mon directeur et de mes encadrants. À ce titre, je suis très reconnaissante envers Jérôme LAURENCIN, mon directeur de Thèse. Une thèse n'est jamais un long fleuve tranquille mais nous avons su faire face aux difficultés qu'elles soient de fond ou de forme et venir à bout des champs de phase ! Je te remercie pour tout ce que tu as pu m'apporter durant ces 3 années. Je remercie profondément Karine COUTURIER, mon encadrante CEA pour premièrement son aide sur le côté scientifique avec la réalisation des tests, qui ne fut pas une partie simple, la remercie également pour son soutien et sa bienveillance sur un plan plus personnel à travers les longues discussions que nous avons pu avoir. Enfin, je souhaite remercier Maxime HUBERT, mon second encadrant au CEA pour tout le temps qu'il a consacré à m'aider sur mes travaux en y incluant tous ces aspects (tests, caractérisation et modélisation). Son aide me fut indispensable, alors un très grand merci !

Un grand merci à toute l'équipe du G2 et du G1, notamment, Marie, Bertrand, Géraldine, Cyril, Mathias, Denis, Brigitte, Stéphane, Denis, Lionel, Simon, Jérôme A. et également l'équipe du labo pour votre grande aide pour mes manip mais aussi pour les moments de pause partagés : Thibault, Jérémy, Julien, Lucas et Bruno.

Merci à Thomas pour ces longues heures passées au MEB à m'apprendre, analyser et faire des reconstructions FIB-SEM, tu m'as bien aidé !

Merci du fond du cœur à la team Hydrogène : Quentin, Manon, Lydia, Elisa, Amira, Eduardo, les Giuseppe S., Cyntia, Kharty, Ozden, Zaman, Davide, Angel que j'ai pu apprendre à connaître durant ces 3 ans. Au-delà de la thèse, je suis heureuse de vous avoir rencontré et de vous compter parmi mes amis. J'ai hâte de vous retrouver un peu partout en France ou dans le monde !

Plus personnellement, je remercie tous mes amis pour leur soutien et leur amitié très chère à mes yeux que ce soit sur le plan de la thèse ou autre, que ce soit à distance où à travers vos et nos nombreux déplacements à Grenoble ou ailleurs.

Enfin, je remercie infiniment ma famille pour leur amour et leur soutien infaillible. Cette réussite n'aurait pas été possible sans vous, alors c'est aussi la vôtre.

## Abstract

The Solid Oxide Cells (SOCs) durability remains one of the main issues limiting the large-scale deployment of the high temperature fuel cell and electrolysis technology. The high operating temperature (700°C-850°C) and polarization can induce reactivity between the cell components or microstructure evolution in the electrodes especially in electrolysis mode (SOEC). Specifically, the classical Ni-YSZ cermet used as hydrogen electrode is subjected to local Ni particle coarsening and redistribution over large distance. Indeed, a substantial Ni migration away from the electrolyte/cermet interface is generally observed in electrolysis mode. Conversely, only a slight Ni enrichment of the electrolyte/hydrogen electrode interface is detected for long-term operation in fuel cell mode. However, the underlying mechanism for the Ni migration remains unclear. Therefore, this thesis has been dedicated to the understanding of the Ni migration using a coupled experimental and modelling approach. For this purpose, a new mechanism has been studied that takes into account the evolution of the electrochemical double layer and the Ni wettability on YSZ with the electrode polarization. For this purpose, a series of long-term tests has been conducted in order to investigate the effect of the different operating conditions (temperature, duration and operating mode) on the evolution of the Ni microstructure including post-test microstructural characterization. Then, a model based on the proposed mechanism has been developed in a finite element code (COMSOL®) using the phase-field theory to predict the evolution of the Ni migration on real microstructures. The phase-field model has been first validated on a simplified microstructure before being applied to a real one. It is worth noting that the gradient in Ni/YSZ wettability imposed as boundary conditions in the phase-field model has been computed with an electrochemical model calibrated to reproduce the behavior of the cells used in this work. The microstructural evolutions in the Ni-YSZ cermet have been simulated for an operation in SOEC and SOFC modes in the conditions of the experiments ( $\pm 1$  A/cm<sup>2</sup>, 750°C, 2000h each). The results have been discussed in the light of the bibliography and confronted to the experimental electrode reconstructions. The good agreement between the simulations and the experimental data tends to prove the relevance of the proposed mechanism.

## Résumé

La durabilité des Cellules à Oxydes Solides (SOCs) reste l'un des principaux problèmes limitant le déploiement à grande échelle de la technologie de pile à combustible et électrolyse haute température. La température de fonctionnement élevée (700°C-850°C) ainsi que la polarisation peuvent induire une réactivité entre les composants de la cellule ainsi qu'une évolution de la microstructure des électrodes, en particulier en mode électrolyse (SOEC). Plus précisément, le cermet de Ni-YSZ, classiquement utilisé comme électrode à hydrogène est soumis à un grossissement local des particules de Ni et à une redistribution sur une grande distance. En effet, une migration substantielle du Ni depuis l'interface électrolyte/cermet est généralement observée en mode électrolyse. Inversement, seul un léger enrichissement en Ni de l'interface électrolyte/électrode à hydrogène est détecté après un temps long de fonctionnement en mode pile à combustible. Cependant, le mécanisme sous-jacent à l'origine de la migration du Ni, est peu ou mal compris et fait l'objet de nombreuses études internationales. Cette thèse a donc été consacrée à la compréhension du mécanisme de migration du Ni, en utilisant une approche expérimentale couplée à de la modélisation. Dans ce cadre, un nouveau mécanisme a été finement étudié qui prend en compte l'évolution de la double couche électrochimique et la mouillabilité du Ni sur la YSZ avec la polarisation de l'électrode. Pour ce faire, une série de tests de longues durées a été menée afin d'étudier l'effet des différentes conditions de fonctionnement (température, durée et mode de fonctionnement) sur l'évolution de la microstructure du Ni, y compris la caractérisation post-test de la microstructure. Ensuite, un modèle basé sur le mécanisme proposé a été développé dans un code d'éléments finis (COMSOL®), utilisant la théorie de champ de phase pour la prédiction de l'évolution de la migration du Ni. Le modèle de champ de phase a initialement été validé sur une microstructure simplifiée avant d'être appliqué à une microstructure réelle. Il convient de noter que le gradient de mouillabilité Ni/YSZ imposé comme conditions limites dans le modèle de champ de phase a été calculé à l'aide d'un modèle électrochimique calibré pour reproduire le comportement des cellules utilisées dans le cadre de cette thèse. Les évolutions de microstructure du cermet ont été simulées en modes SOEC et SOFC dans les conditions des tests de durabilité (-/+1 A.cm<sup>-2</sup>, 750°C, 2000h chacun). Les résultats ont été discutés à la lumière de la bibliographie et confrontés aux reconstructions expérimentales des électrodes. Le bon accord entre les simulations et les données expérimentales a permis de confirmer la pertinence du mécanisme proposé.

# Table of contents

<b>Abstract and Résumé</b>	1
<b>Table of contents</b>	3
<b>List of figures</b>	5
<b>Résumé étendu en français</b>	8
<b>List of symbols</b>	13
<b>General introduction</b>	14
<b>1. Literature review on Solid Oxide Cells (SOCs): Degradation of the hydrogen electrode</b>	17
<b>1.1 SOC operation and architecture</b>	17
1.1.1 Principle	17
1.1.2 Architecture	19
<b>1.2 Materials</b>	20
1.2.1 Electrolyte	20
1.2.2 Oxygen electrode	21
1.2.3 Hydrogen electrode	22
<b>1.3 Electrochemistry of the cell</b>	23
1.3.1 Cell operation	23
1.3.2 Reaction Mechanism for the Hydrogen Electrode	26
<b>1.4 Cell degradations</b>	28
1.4.1 Electrolyte	28
1.4.2 Oxygen electrode	28
1.4.3 Hydrogen electrode	29
<b>1.5 The morphological evolution of the Ni</b>	30
<b>1.6 Conclusion</b>	33
<b>2. Materials and methods</b>	39
<b>2.1 Long-term tests</b>	39
2.1.1 Cell description	39
2.1.2 Test bench	41
2.1.3 Experimental setup, protocol for testing and data acquisition	42
<b>2.2 Post-test characterization</b>	44
2.2.1 SEM observations	44
2.2.2 EDX analysis	45
2.2.3 FIB-SEM reconstructions	45
2.2.4 Codes for the microstructure	46
<b>2.3 Multi-scale electrochemical model</b>	46

---

2.4	Conclusion	51
3.	Experimental evaluation of degradation tests	54
3.1	Initial cell performances	54
3.2	Study of the degradations under different operating conditions	57
3.2.1	Effect of the operating temperature	57
3.2.2	Effect of the ageing time	59
3.2.3	Effect of the operating mode	62
3.3	Post-test characterization	64
3.3.1	SEM-EDX analysis	64
3.3.2	FIB-SEM reconstruction	70
3.4	Conclusion	77
4.	Modeling the Ni migration	79
4.1	Electrochemical validation	79
4.2	Mechanism for the Ni migration in both SOEC and SOFC modes	81
4.2.1	Description of the proposed mechanism	81
4.2.2	Equation for the computation of the gradients in Ni/YSZ contact angle	84
4.3	Phase-field modeling	85
4.3.1	Validation of the numerical implementation	89
4.4	Elements of validation for the mechanism	90
4.4.1	Gradients of Ni/YSZ contact angle	90
4.4.2	Properties	93
4.5	Conclusion	100
5.	Conclusions and perspectives	103
APPENDIX A		107
1.	First-order phase transition in Landau's theory	108
2.	Fundamentals of the phase-field modeling	109
3.	Allen-Cahn equation	110
3.1	Expression of the energy functional	110
3.2	Minimization of the energy functional at equilibrium $\delta F \phi, \partial_x \phi, x = 0$ to obtain the stationary profile $\phi(x)$	112
3.3	Demonstration of the Allen-Cahn equation	115
3.4	Determination of the interfacial energy	116
3.5	Cahn-Hilliard equation	118
3.5.1	Demonstration of the Cahn-Hilliard equation	118
APPENDIX B		120

---

# List of figures

Figure 0-1: Evolution of the Earth temperature from 1850 until 2020 according to the IPCC [1].	15
Figure 1-1: Energy need for the electrolysis reaction as a function of temperature; enthalpy ( $\Delta H$ ), Gibbs enthalpy ( $\Delta G$ ), entropy ( $T\Delta S$ ) [1].	18
Figure 1-2: Operation principle of SOC in SOEC and SOFC modes.	18
Figure 1-3: Solid Oxide Cell designs: a) tubular and b) planar.	19
Figure 1-4: Ionic conductivity of 8YSZ and 3YSZ as a function of the operating temperature [7].	21
Figure 1-5: Comparison between the reaction mechanisms for a) a LSM-YSZ composite and b) a LSCF electrodes.	22
Figure 1-6: Illustration of a the Ni-YSZ cermet electrode microstructure.	23
Figure 1-7: Schematic representation of an i-U curve in SOEC and SOFC with the OCV and the overpotentials arising in the two operating modes.	24
Figure 1-8: Classical representation of the impedance spectra a) Nyquist plot and b) Bode plot.	26
Figure 1-9: Representation of a) the oxygen spillover and b) the hydrogen spillover mechanisms [28].	28
Figure 1-10: SEM images of the three samples; reference a) and d), SOFC b) and e), and SOEC c) and f). In the low voltage ESB images a)-c) porosity is black, YSZ is lightgray, and Ni is dark gray. In the low voltage images recorded with the Inlens detector d)-f) porosity is black, YSZ and non-percolating Ni are gray and the percolating Ni is white. The dashed lines in d)-f) indicate the area where the decrease of percolating Ni is more visible [53].	31
Figure 2-1: a) Schematic representation of the classical cell, b) SEM images in secondary electrons of the complete cell exhibiting all the layers.	40
Figure 2-2: Schematic representation of the experimental set-up for the durability experiments.	42
Figure 2-3: a) Experimental EIS and after its correction using the ECCM (OCV at 750 °C, $p_{H_2}/p_{H_2O} = 0.1/0.9$ and 12 Nml.cm <sup>-2</sup> .min <sup>-1</sup> ) and b) equivalent circuit model (EECM) used to analyze the EIS spectra.	43
Figure 2-4: Schematic representation of the FIB-SEM technic [3].	46
Figure 2-5: a) Reactions for the hydrogen electrode (expressed in electrolysis mode with the abbreviation CR and ER referring to the chemical and electrochemical reactions, respectively).	47
Figure 2-6: General flowchart of the multi-scale model as repertories in [10].	49
Figure 2-7: Polarization curves in a) SOEC $p_{H_2}/p_{H_2O} = 10/90$ and b) SOFC $p_{H_2}/p_{H_2O} = 100/0$ modes for a flux of 12 NmL.min <sup>-1</sup> .cm <sup>-2</sup> at 750°C [10]. Comparison between simulation and experimental data	49
Figure 2-8: a) Nyquist plot and b) Bode plot of the EIS at OCV (750°C, $p_{H_2}/p_{H_2O} = 10/90$ , total inlet flow rate=12 NmL.min <sup>-1</sup> .cm <sup>-2</sup> ). The ohmic losses have been removed from the impedance diagrams [11].	50
Figure 3-1: Initial i-U curves of the tested cells at the reference SOEC conditions (750°C, $p_{H_2}/p_{H_2O}=10/90$ and 12 Nml.cm <sup>-2</sup> .min <sup>-1</sup> ). The i-U curve of cell 6 is missing because of an experimental issue.	55
Figure 3-2: Initial EIS diagrams at OCV, in a) the Nyquist plot and b) the Bode plot for all the tested cells at 750°C, $p_{H_2}/p_{H_2O}=10/90$ and 12 Nml.cm <sup>-2</sup> .min <sup>-1</sup> .	56
Figure 3-3: Durability curves showing the cell voltage increase for the cells aged at 750°C, 800°C and 850°C for 2000h in SOEC mode at -1 A.cm <sup>-2</sup> , 64% SC, $p_{H_2}/p_{H_2O}=10/90$ and 12 Nml.cm <sup>-2</sup> .min <sup>-1</sup> .	57
Figure 3-4: EIS diagrams in the Nyquist and Bode plots, measured at OCV, $p_{H_2}/p_{H_2O}=10/90$ , 64% SC and 12 Nml.cm <sup>-2</sup> .min <sup>-1</sup> for initial and final plot of the cells aged at 750°C, 800°C and 850°C for 2000h. The diagrams have been corrected of the wires inductance using EEC showed in Figure 3-3 of chapter 2.	58
Figure 3-5: Durability curves showing the cell voltage increase for the cells aged at 800°C for 1000h, 2000h and 5000h in SOEC mode at -1 A.cm <sup>-2</sup> , 64% SC, $p_{H_2}/p_{H_2O}=10/90$ and 12 Nml.cm <sup>-2</sup> .min <sup>-1</sup> .	59
Figure 3-6: EIS diagrams in the Nyquist and Bode plots, measured at OCV, 750°C, $p_{H_2}/p_{H_2O}=10/90$ , 64% SC and 12 Nml.cm <sup>-2</sup> .min <sup>-1</sup> for initial and final plot of the cells aged 1000h, 2000h and 5000h at	

800°C. The diagrams have been corrected of the wires inductance using EEC showed in Figure 1-3 of chapter 2. ....	60
Figure 3-7: Evolution as a function of the time of the EIS diagrams in the a) Nyquist plot and b) Bode plot of the cell aged for 5000h in SOEC at 800°C. ....	61
Figure 3-8: Durability curve showing the cell voltage evolution for the cell aged at 800°C for 2000h in SOFC mode at 1 A·cm <sup>-2</sup> , 64% of fuel utilization, p <sub>H<sub>2</sub></sub> /p <sub>H<sub>2</sub>O</sub> =90/10 and 12 Nml·cm <sup>-2</sup> ·min <sup>-1</sup> . ....	62
Figure 3-9: EIS diagrams measured at OCV, 750°C, 90 vol.% H <sub>2</sub> O and 10 vol.% H <sub>2</sub> and 12 Nml·cm <sup>-2</sup> ·min <sup>-1</sup> for the initial and final plot of the cells aged for 2000h at 800°C in SOFC and SOEC mode. The diagrams have been corrected of the wires inductance using EEC showed in Figure 2-3 of chapter 2. ....	63
Figure 3-10: SEM images in back-scattering electrons of the Ni-YSZ/YSZ interface performed on a) the reference cell, and the cells aged b) at 750°C, c) at 800°C and d) at 850°C. The images are taken at the gas inlet (center of the cell). Ni coarsening is indicated by the orange dashed circles and Ni depletion by the green dashed lines. ....	65
Figure 3-11: SEM images in back-scattering electrons of the Ni-YSZ/YSZ interface for the cell aged 2000h at 800°C: a) at the gas inlet (center of the cell), b) at the gas outlet (cell periphery). The yellow arrows show the detachment of the remaining Ni particles in the depletion zone. ....	65
Figure 3-12: EDX analysis taken at the inlet of the Ni volume fraction for a) the samples aged at 750°C, 800°C and 850°C for 2000h in SOEC mode and b) for the samples aged at 800°C taken at the gas inlet and outlet in SOEC mode as a function of the electrode thickness (Cf. to the Annexe B to the EDX cartography for the Ni phase). ....	66
Figure 3-13: SEM images in secondary electrons of the Ni-YSZ/YSZ interface for a) the cell aged for 5000h at 800°C in SOEC mode, b) the zoomed interface and c) 2000h at 800°C in SOEC mode, taken all at the cell inlet. Pores in black. ....	67
Figure 3-14: EDX analysis of the Ni volume fraction for the samples aged for 2000h and 5000h in SOEC mode at 800°C as a function of the electrode thickness (Cf. to the Annexe B to the EDX cartography for the Ni phase). ....	68
Figure 3-15: SEM image in secondary electrons of the Ni-YSZ/YSZ interface for the cells aged for 2000h at 800°C in (a) SOFC and (b) SOEC mode. Pores in black. ....	69
Figure 3-16: EDX analysis of the Ni volume fraction for the samples aged at 800°C for 2000h in SOFC and SOEC mode as a function of the electrode thickness (Cf. to the Annexe B to the EDX cartography for the Ni phase). ....	70
Figure 3-17: 3D FIB-SEM reconstructions of the hydrogen electrode performed on the reference, and the cells aged for 2000h at 750°C, 800°C and 850°C. The reconstructions have been taken at around 0.7 cm from the cell center (gas inlet) and the electrolyte is located at the bottom of the volumes. ....	71
Figure 3-18: Mass center evolution of the cells aged for 2000h in SOEC mode as a function of the operating temperature. ....	72
Figure 3-19: Evolution of the a) Ni and c) YSZ volume fraction and b) the active TPB density as a function of the electrode thickness after 2000h in SOEC mode at 750°C, 800°C and 850°C. ....	72
Figure 3-20: 3D FIB-SEM reconstructions of the hydrogen electrode performed on the cells aged for 2000h and 5000h at 800°C. The reconstructions have been taken at around 0.7 cm from the cell center (gas inlet). ....	73
Figure 3-21: Mass center evolution of the cells aged at 800°C in SOEC mode as a function of the ageing time. ....	74
Figure 3-22: Evolution of a) the Ni volume fraction and b) the active TPB density as a function of the electrode thickness in SOEC mode after 2000h and 5000h at 800°C. ....	75
Figure 3-23 : 3D FIB-SEM reconstruction of the hydrogen electrode performed on the cell aged for 2000h at 800°C in SOEC and SOFC modes. The reconstruction has been taken at around 0.7 cm from the cell center (gas inlet). ....	75

Figure 3-24: Evolution of a) the Ni volume fraction and b) the active TPB density as a function of the electrode thickness in SOEC and SOFC modes after 2000h at 800°C. ....	76
Figure 4-1: Simulated and experimental i-U curves at 750°C in SOEC mode for $p_{H_2}/p_{H_2O} = 0.1/0.9$ and $12 \text{ Nml.cm}^{-2}.\text{min}^{-1}$ . ....	80
Figure 4-2: Simulated and experimental EIS spectra after correction with the EECM, at OCV, 750°C, $p_{H_2}/p_{H_2O} = 0.1/0.9$ and $12 \text{ Nml.cm}^{-2}.\text{min}^{-1}$ , a) in Nyquist plot, b) in Bode plot. ....	80
Figure 4-3: Evolution of the oxygen vacancies concentration in the Ni/YSZ double layer as a function of the electrode overpotential. ....	82
Figure 4-4: a) Schematic explanation of the Ni migration mechanism from the overpotential gradient to the contact angles one and b) Schematic representations of the Ni migration mechanism in both SOEC and SOFC modes with the system of coordinates. ....	83
Figure 4-1: Stationary profile of the phase field at the Ni/pore interface as a function of the distance $x$ in $\mu\text{m}$ for example. ....	87
Figure 4-6: Evolution of the mobility $M(\phi)$ as a function of the phase-field variable $\phi$ . ....	88
Figure 4-7: Mesh of the 3D geometry used for the validation of the phase-field model (the small cube inside parallelepiped is the initial Ni particle enclosed in the gas phase (i.e. air for the parallelepiped))	89
Figure 4-8: Evolution from an initial to a final state (after 10000s) of a particle under the application of a gradient in contact angle between the particle and the substrate for a window of $1.5 \mu\text{m}$ . ....	90
Figure 4-9: Distribution of the current density and the $p_{H_2}$ and $p_{H_2O}$ along the cell radius $r$ at 750°C, $12 \text{ Nml.cm}^{-2}.\text{min}^{-1}$ , $\pm 1 \text{ A.cm}^{-2}$ for a gas composition of $p_{H_2}/p_{H_2O} = 0.9/0.1$ and $p_{H_2}/p_{H_2O} = 0.1/0.9$ respectively (b) in SOFC and (a) SOEC modes. ....	91
Figure 4-10: Evolution of the electrode overpotential in SOEC and SOFC modes as a function of the electrode thickness for the local conditions corresponding to a radial position of 0.7 cm from the cell center (750°C, $12 \text{ Nml.cm}^{-2}.\text{min}^{-1}$ , $p_{H_2}/p_{H_2O}=0.28/0.72$ in SOEC mode and $p_{H_2}/p_{H_2O}=0.73/0.27$ in SOFC mode). ....	92
Figure 4-11: a) Evolution of the concentration of the oxygen vacancies in the double layer and b) evolution of the contact angle between the Ni and YSZ as a function of the electrode thickness at 750°C, $12 \text{ Nml.cm}^{-2}.\text{min}^{-1}$ , $\pm 1 \text{ A.cm}^{-2}$ for a gas composition of $p_{H_2}/p_{H_2O} = 0.9/0.1$ and $p_{H_2}/p_{H_2O} = 0.1/0.9$ in SOFC and SOEC modes respectively. DL = double layer. ....	93
Figure 4-12: Mesh of the $4 \times 4 \times 6 \mu\text{m}$ volume with a typical mesh size of 100 nm. ....	94
Figure 4-13: Evolution of the volumes in b),c) SOEC ( $-1 \text{ A.cm}^{-2}$ , $p_{H_2}/p_{H_2O} = 0.1/0.9$ , $12 \text{ Nml.cm}^{-2}.\text{min}^{-1}$ and 750°C and d),e) SOFC ( $1 \text{ A.cm}^{-2}$ , $p_{H_2}/p_{H_2O} = 0.9/0.1$ , $12 \text{ Nml.cm}^{-2}.\text{min}^{-1}$ and 750°C) after respectively 1000h (b) and d)) and 2000h (c) and e)) of simulation with the Ni/YSZ contact angle gradients calculated in Figure 1 11 b) and compared to a) the reference. ....	95
Figure 4-14: 3D microstructures of the Ni phase only for a) the reference, b),c) SOEC ( $-1 \text{ A.cm}^{-2}$ , $p_{H_2}/p_{H_2O} = 0.1/0.9$ , $12 \text{ Nml.cm}^{-2}.\text{min}^{-1}$ and 750°C) and c), d) SOFC ( $1 \text{ A.cm}^{-2}$ , $p_{H_2}/p_{H_2O} = 0.9/0.1$ , $12 \text{ Nml.cm}^{-2}.\text{min}^{-1}$ and 750°C), with the Ni/YSZ contact angle gradients calculated in Figure 1 11 b) after respectively 1000h (b) and d)) and 2000h (c) and e)) of simulation. The electrolyte is located at the top . ....	95
Figure 4-15: Evolution as a function of time of the mass center calculated over the electrode thickness for the Ni phase for an operation in SOEC ( $-1 \text{ A.cm}^{-2}$ , $p_{H_2}/p_{H_2O} = 0.1/0.9$ , $12 \text{ Nml.cm}^{-2}.\text{min}^{-1}$ and 750°C) and SOFC ( $1 \text{ A.cm}^{-2}$ , $p_{H_2}/p_{H_2O} = 0.9/0.1$ , $12 \text{ Nml.cm}^{-2}.\text{min}^{-1}$ and 750°C) with the Ni/YSZ contact angle gradients calculated in Figure 1-11 b).....	97
Figure 4-16: Phase fraction evolution of the Ni phase for the reference and after 1000h and 2000h of simulation in a) SOEC ( $-1 \text{ A.cm}^{-2}$ , $p_{H_2}/p_{H_2O} = 0.1/0.9$ , $12 \text{ Nml.cm}^{-2}.\text{min}^{-1}$ and 750°C) and b) SOFC ( $1 \text{ A.cm}^{-2}$ , $p_{H_2}/p_{H_2O} = 0.9/0.1$ , $12 \text{ Nml.cm}^{-2}.\text{min}^{-1}$ and 750°C) with the Ni/YSZ contact angle gradients calculated in Figure 1-11 b). ....	98

## Résumé étendu en français

Depuis plus de 50 ans, les avancées scientifiques mondiales ont largement contribué à améliorer le niveau de vie de nos sociétés. Ces améliorations et découvertes ont cependant entraîné une augmentation exponentielle de la demande mondiale d'énergie depuis les années 1970. Cette évolution a engendré une série de problèmes écologiques affectant dorénavant tous les écosystèmes. Un des problèmes majeurs liés à cette surconsommation d'énergie est l'émission massive de gaz à effet de serre ( $\text{CO}_2$ ,  $\text{CH}_4$  ...) qui induit un réchauffement climatique sans précédent. Dans son rapport spécial de 2018, le Groupe Intergouvernemental d'Experts sur l'évolution du Climat (GIEC) a proposé un modèle pour prédire les conséquences les plus probables d'une augmentation de la température moyenne de  $1,5^\circ\text{C}$ . Ce scénario implique de lourdes conséquences économiques, sociales et sanitaires. Une augmentation de la température plus importante que celle prévue actuellement aura des impacts d'autant plus désastreux, affectant toutes les parties du monde. La situation alarmante dans laquelle nous nous plaçons, nous impose de développer des solutions technologiques alternatives permettant de remplacer l'utilisation des combustibles fossiles. Afin d'être neutre en émission carbone, le mix énergétique à l'échelle mondiale doit être majoritairement remplacé par des énergies renouvelables, telles que l'énergie solaire, éolienne ou hydraulique. Cependant, en raison de l'intermittence des énergies renouvelables, il est également nécessaire de développer des technologies capables de stocker les surproductions d'énergie et de les redistribuer lorsque la demande dépasse la production. Dans ce contexte, le dihydrogène apparaît comme un vecteur énergétique intéressant car il a l'avantage d'être particulièrement énergétique et offre la possibilité d'être stocké et transporté relativement facilement. En outre, il peut être utilisé dans des convertisseurs électrochimiques transformant l'énergie chimique contenu dans ce gaz en électricité (mode pile à combustibles). Inversement, ces convertisseurs peuvent être employés pour produire du dihydrogène à partir d'électricité (mode électrolyseur). Ces dispositifs pourraient donc permettre d'absorber les pics de production électrique dus au caractère intermittent des énergies renouvelables et de réinjecter l'électricité dans le réseau en cas de besoin. Parmi les différentes possibilités, les Cellules à Oxydes Solides (SOCs) sont l'une des technologies les plus prometteuses en termes d'efficacité, de coût et de sécurité ainsi que pour son caractère réversible entre les modes pile et électrolyse. Ces cellules fonctionnent à haute température ( $650^\circ\text{C}$ - $900^\circ\text{C}$ ) avec une possibilité d'utilisation variée de gaz combustibles. La technologie SOC se compose d'un électrolyte dense qui est une céramique de Zircone Stabilisée à l'oxyde d'Yttrium (YSZ) séparant deux électrodes poreuses à hydrogène et oxygène. L'électrode à oxygène est composée d'une pérovskite à conduction mixte ionique et électronique (MIEC) tel que le Ferrite de Lanthane dopée au Strontium et Cobalt (LSCF),

$\text{La}_{0.6}\text{Sr}_{0.4}\text{Co}_{0.2}\text{Fe}_{0.8}\text{O}_{3-\delta}$ . L'électrode à hydrogène est composée d'un cermet Ni-YSZ où le Ni assure la conduction électronique tandis que la YSZ, assure la conduction ionique. L'électrode à hydrogène est constituée d'un réseau enchevêtré de phase Ni, YSZ et de pores afin d'obtenir une forte densité de lignes de contact triple entre les électrons, les ions  $\text{O}^{2-}$  et le gaz réactif (TPB), où se déroulent les réactions électrochimiques. La densité de TPB joue à ce titre un rôle crucial dans les performances globales des SOCs. Cependant, la durabilité insuffisante des SOCs reste à ce jour un problème majeur qui limite considérablement le déploiement industriel de cette technologie. Parmi les phénomènes de dégradation, l'évolution microstructurale de l'électrode à hydrogène (cermet de Ni-YSZ) et plus particulièrement la redistribution des particules de Ni dans l'électrode contribue fortement à baisser les performances de la cellule en fonctionnement. Les particules de Ni sont soumises à de l'agglomération dans les deux modes de fonctionnement (électrolyse et pile) ainsi qu'à de la redistribution sur de longues distances (mode électrolyse). En effet, on observe en mode électrolyse, une forte déplétion de Ni à l'interface avec l'électrolyte après seulement quelques heures de fonctionnement. En revanche, en mode pile, on observe un très léger enrichissement de Ni après un très long temps de fonctionnement. Le mécanisme sous-jacent à l'origine de la migration du Ni, est peu ou mal compris et fait l'objet de nombreuses études internationales.

Dans ce contexte, les objectifs de la thèse sont orientés sur la compréhension et la simulation d'un nouveau mécanisme de migration du Ni dans l'électrode à hydrogène. Un modèle électrochimique multi-échelle permettant de reproduire les performances de la cellule a été validé et calibré pour les cellules CEA utilisées dans ces travaux. Ce modèle est ensuite couplé à des simulations en champ de phase pour reproduire l'évolution microstructurale du Ni (migration vers le cœur de l'électrode à hydrogène et agglomération). Afin de mieux comprendre et de valider le mécanisme proposé, des tests électrochimiques en cellules complètes ont été effectués dans différentes conditions en faisant varier le mode de fonctionnement, la durée de vieillissement et la température de fonctionnement. A la suite de ces essais, des analyses post-tests comprenant des observations au Microscope Electronique à Balayage (MEB), des analyses EDX ainsi que des reconstructions 3D au FIB-SEM (Focused Ion Beam-Scanning Electron Microscopy) ont été réalisées afin de quantifier l'évolution microstructurale au travers notamment de calculs des propriétés de microstructure. Le modèle de champ de phase pour la simulation de l'évolution microstructurale du Ni (migration et agglomération) basé sur le mécanisme proposé a été développé puis validé afin d'être appliqué à des microstructures réelles. Les différentes études menées dans le cadre de cette thèse sont exposées dans le présent manuscrit, rédigé en quatre chapitres distincts.

Le premier chapitre est dédié à la présentation générale des SOCs. Le principe général de fonctionnement, les différents types d'architecture, les matériaux composants chacune des couches de la cellule CEA étudiée sont présentés dans ce chapitre. Les principes électrochimiques mis en jeu dans ces cellules ainsi que les mécanismes de réaction sont également décrits. Les mécanismes de dégradation de la cellule sont détaillés avec une attention particulière portée sur l'évolution microstructurale du cermet Ni-YSZ et notamment la migration du Ni, problème central de ce travail de thèse.

Le second chapitre présente les outils utilisés afin de répondre aux objectifs de la thèse. Une série de tests électrochimiques entre 750°C et 850°C pour des durées allant jusqu'à 5000h a été menée sur les cellules CEA afin d'investiguer l'effet de la température, du temps de vieillissement et du mode de fonctionnement sur les dégradations de la cellule. Pour cela, le banc de test utilisé pour l'étude est tout d'abord présenté dans cette partie. De plus, le protocole de tests employé est décrit en détails. Il inclut des mesures électrochimiques comprenant d'une part des courbes de durabilité permettant l'évaluation du taux de dégradation apparent de la tension de cellule, d'autre part des courbes de polarisation et des spectres d'impédance électrochimique (SIE) à l'état initial, intermédiaire et final. Ce deuxième type de mesures permet l'évaluation de la dégradation réelle des performances de la cellule dans des conditions de référence. A la suite des essais, des analyses post-tests ont été menées sur des échantillons de chaque cellule testée, qui ont été préalablement enrobés et polis. Les caractérisations microstructurales comprennent des observations au MEB, des analyses EDX ainsi que des reconstructions au FIB-SEM afin d'obtenir des volumes représentatifs de l'électrode à hydrogène. Un ensemble d'outils numériques a été déployé au sein de l'équipe et est utilisé dans ce travail pour quantifier l'évolution des propriétés microstructurales avant et après vieillissement. De plus, un modèle électrochimique multi-échelle élaboré au laboratoire depuis plusieurs années a également été calibré, validé puis couplé au modèle de champ de phase développé dans cette étude. Le modèle électrochimique a permis d'analyser les spectres d'impédance électrochimique et d'attribuer la partie hautes fréquences des spectres à l'électrode à hydrogène, la partie moyennes fréquences à l'électrode à oxygène et la partie basses fréquences à la conversion des gaz.

Concernant le chapitre trois, ce dernier est dédié aux résultats expérimentaux comprenant les données électrochimiques et les caractérisations post-tests. Dans la première partie, la validité et la reproductibilité des essais est commentée grâce à l'analyse de l'étanchéité, des courbes de polarisation initiales de chaque essai ainsi que des spectres d'impédance dans le plan de Nyquist. A la suite de cette section, les courbes de durabilité ainsi que les spectres d'impédance électrochimique initiaux et finaux de chaque

essai ont été analysés en fonction de la température, du temps de vieillissement et du mode de fonctionnement. Les dégradations réelles de la cellule sont mesurées et analysées grâce aux spectres d'impédance obtenus dans des conditions de référence avant et après fonctionnement sous courant. Concernant le vieillissement en mode électrolyse, la contribution à hautes fréquences ainsi que la résistance ohmique ont augmenté avec l'augmentation de la température (pour une durée de 2000h de fonctionnement) et du temps de vieillissement (à 800°C). Un ralentissement des phénomènes de dégradation dans le temps est également observé d'après ces mêmes données expérimentales. Ces évolutions sont attribuées à une dégradation conséquente de l'électrode à hydrogène plus particulièrement liée à l'agglomération et la migration du Ni. En revanche, pour le vieillissement en mode pile, seule une augmentation de la résistance hautes fréquences a été observée sans modification de la partie ohmique. De plus les caractérisations post-tests incluant les observations MEB, les mesures EDX et l'analyse des reconstructions 3D, ont permis de mettre en évidence que l'augmentation de la température provoque en électrolyse une augmentation du phénomène de migration du Ni, alors que l'effet du temps de vieillissement est moins clair (augmentation ou stabilisation). En revanche, en mode pile, aucune migration du Ni n'a été observée à part une forte agglomération.

Le quatrième et dernier chapitre est consacré à la modélisation de la redistribution du Ni dans l'électrode à hydrogène. Premièrement, le modèle multi-échelle électrochimique a été calibré et validé pour les cellules utilisées dans cette étude. Un modèle pour la migration du Ni a été présenté dans ce travail de thèse. Ce dernier repose sur l'évolution de la double couche électrochimique à l'interface Ni/YSZ lorsque la cellule est sous polarisation. Il est important de souligner que l'interface Ni/YSZ est caractérisée par des liaisons Ni-O. En effet, les surtensions cathodiques locales d'électrode (mode électrolyse) provoquent une accumulation de lacunes d'oxygène dans cette double couche électrochimique et la déstabilisent (baisse du travail d'adhésion -  $W_{adh}$  - entre le Ni et la YSZ) en remplaçant les atomes d'oxygène par des lacunes (et inversement pour la polarisation anodique, mode pile). La concentration en lacunes d'oxygène dans la double couche électrochimique est exprimée en fonction de la surtension d'électrode et de l'épaisseur de l'électrode pour une certaine position le long de la cellule. Ainsi le gradient de surtension calculé dans le modèle électrochimique provoque un gradient de concentration des lacunes d'oxygène dans toute l'épaisseur de l'électrode, qui induit un gradient de travail d'adhésion  $W_{adh}$  entre le Ni et la YSZ. En conséquence, l'angle de contact entre le Ni et la YSZ caractérisant la mouillabilité du Ni sur la YSZ, évolue également en fonction de l'épaisseur de l'électrode. On trouve, en mode électrolyse, un fort gradient d'angle de contact, avec de grandes valeurs à l'interface avec l'électrolyte qui diminuent pour atteindre une valeur d'équilibre au voisinage de l'interface avec le collecteur de courant. En mode pile, un faible gradient d'angle de contact est attendu avec des valeurs plus petites à l'interface avec

l'électrolyte. Ce gradient d'angle de contact entre le Ni et la YSZ est supposé être la force motrice de la migration du Ni. La méthode dite par champ de phase a été adoptée pour simuler la migration du Ni dans cette thèse. Le modèle de champ de phase a été implémenté dans un logiciel d'éléments finis (en utilisant la boîte à outils mathématiques de COMSOL®) pour simuler la migration du Ni dans les deux modes de fonctionnement et ainsi valider le mécanisme proposé dans ce travail. Des simulations de 2000h de vieillissement en mode électrolyse et pile ont été obtenues dans les conditions de test de durabilité suivantes : 750°C,  $\pm 1 \text{ A.cm}^{-2}$ ,  $12 \text{ NmL.min}^{-1}.\text{cm}^{-2}$  de débit gazeux total avec  $p_{\text{H}_2}/p_{\text{H}_2\text{O}} = 10/90$  et  $90/10$ , en mode électrolyse et pile respectivement.

Dans les deux cas d'étude, le modèle de champ de phase s'est montré capable de reproduire les résultats expérimentaux en étudiant les propriétés microstructurales entre les volumes initial et final telles que l'évolution de la fraction volumique et du centre de masse du Ni dans l'épaisseur de l'électrode.

Cependant, d'autres études expérimentales et de modélisation sont encore nécessaires afin de mieux appréhender le mécanisme sous-jacent complexe qui contrôle la migration du Ni.

# List of symbols

## Roman Symbols:

$a$	Chemical activities	
$C_{V\ddot{o}}^{bulk}$	Oxygen vacancy concentration at equilibrium	(mol.m <sup>3</sup> )
$C_{V\ddot{o}}^{int}$	Oxygen vacancy concentration at the Ni/YSZ interface	(mol.m <sup>3</sup> )
$C_{V\ddot{o}}^{max}$	Maximum oxygen vacancy concentration	(mol.m <sup>3</sup> )
$D$	Diffusion coefficient of Ni	(m <sup>2</sup> .s <sup>-1</sup> )
$E_a$	Activation energy	(kJ.mol <sup>-1</sup> )
$F$	Faraday's constant	(C.mol <sup>-1</sup> )
$K_a$	Oxygen adsorption coefficient	
$M$	Mobility	(m <sup>5</sup> .J.s <sup>-1</sup> )
$Na$	Avogadro's number	
$R$	Universal constant	(J.mol <sup>-1</sup> .K <sup>-1</sup> )
$R_s$	Ohmic resistance	(Ω.cm <sup>2</sup> )
$R_p$	Polarization resistance	(Ω.cm <sup>2</sup> )
$Sp_{ij}$	Specific interfacial surface areas between two phases i and j	(μm <sup>-1</sup> )
$U^0$	Cell voltage in the standard conditions	(V)
$V_{uc}$	Volume of the unit cell for cubic zirconia	(Å <sup>3</sup> )
$V_m$	Molar volume of Ni	(m <sup>3</sup> .mol <sup>-1</sup> )
$W_{adh}$	Work of adhesion at the Ni/YSZ interface	(J.m <sup>-2</sup> )
$w$	Height of the energy barrier for the transition from one phase to another	(J.m <sup>-3</sup> )
$z$	Number of exchanged electrons in the electrochemical reactions	

## Greek symbols:

$\alpha$	Symmetry factor or Charge transfer coefficient	
$\gamma^p$	Surface tension of pure Ni without oxygen adsorption	(N.m <sup>-1</sup> )
$\delta$	Half-thickness of the phase field interface	(m)
$\varepsilon$	Gradient coefficient	((J.m <sup>-1</sup> ) <sup>1/2</sup> )
$\varepsilon$	Volume fraction of each phase	
$\eta$	Overpotential	(V)
$\theta_{Ni/YSZ}^{max}$	Maximum contact angle between Ni and YSZ	(°)
$\theta_{Ni/YSZ}^{eq}$	Equilibrium contact angle between Ni and YSZ	(°)
$\phi$	Phase-field variable	
$\mu$	Chemical potential	
$\xi_{TPBLs}$	Density of active TPBLs	(μm <sup>-2</sup> )
$\sigma$	Interface energy	(J.m <sup>-2</sup> )
$\tau$	Apparent' tortuosity factors	
$\Gamma_O$	Saturation coverage of oxygen adsorption on Ni surface	(N.m <sup>-1</sup> )

# General introduction

The 21st century is marked by unprecedented challenges, with perhaps the most pressing one being the escalating threat of global warming. Indeed, global warming is an undeniable reality that demands our collective attention, understanding and action. Global warming refers to the long-term increase in the Earth's average surface temperature, primarily due to the high concentration of greenhouse gases in the atmosphere. Indeed, the combustion of fossil fuels, deforestation, industrial processes and other human activities have exponentially increased the levels of carbon dioxide, methane and other greenhouse gases in the atmosphere, trapping heat and disrupting the balance of the planet climate [1]. The consequences of these activities manifest in rising temperatures, extreme weather and climate events, impact on food, water security and human health, and damage on economies and society. At the heart of this environmental crisis is the energy sector, a cornerstone of modern civilization. Historically, our economy based on non-renewable energy sources has contributed significantly to the accumulation of greenhouse gases in the atmosphere, driving global warming. According to the Intergovernmental Panel on Climate Change (IPCC), Figure 0-1 shows the global temperature increase over the last 170 years, mainly due to greenhouse gas emissions. Indeed, the global surface temperature has increased by 1.1°C from 1850–1900 to 2011–2020 owing to the emissions of greenhouse gases. The urgency of this situation has led to a growing need for a transition to sustainable energy to mitigate the effects of climate change. It is imperative for the global community to reduce carbon emissions and to accelerate the transition towards a low-carbon economy. In this context, the importance of renewable energy sources such as solar, wind, hydro, and geothermal power cannot be undervalued. These sources not only offer a cleaner alternative to traditional fossil fuels but also present opportunities for economic growth, technological innovation and energy independence. However, they are intermittent so that their production of electricity is not constant over time. In fact, they need to be coupled with an effective system for storing and releasing excess energy depending on the electricity demand.

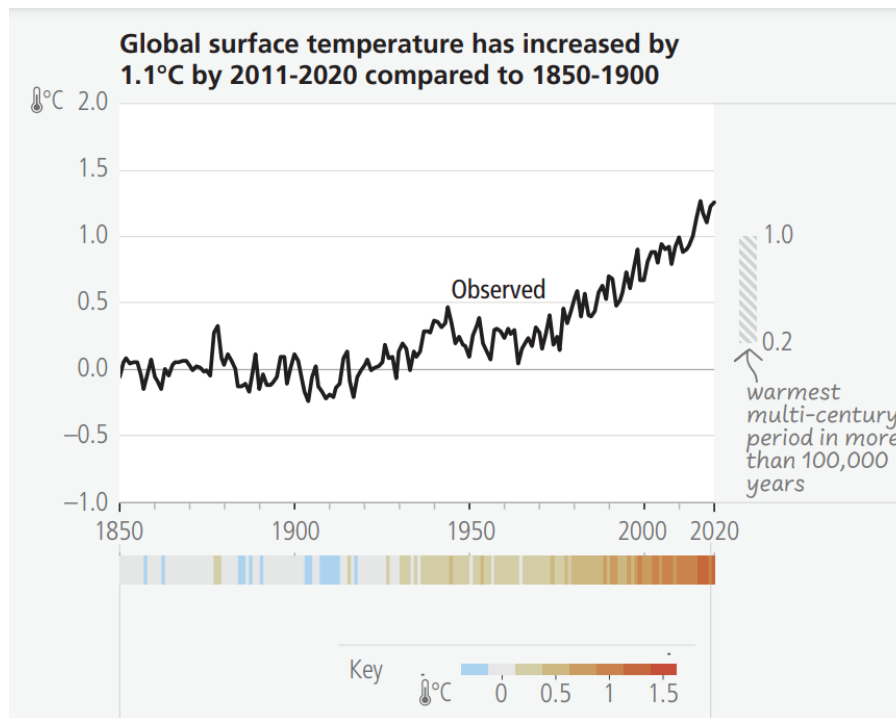


Figure 0-1: Evolution of the Earth temperature from 1850 until 2020 according to the IPCC [1].

It is in this context that hydrogen is nowadays considered as an interesting energy vector that could be used in a climate-neutral society [2]. It has to be combined with an efficient electrochemical system able to produce electricity in fuel cell mode during the peaks of consumption and hydrogen in electrolysis mode during the low demand periods [3]. Therefore, the high-temperature electrochemical devices based on Solid Oxide Cells (SOCs) are considered as one of the most promising technologies thanks to various advantages such as a high efficiency, a relatively low cost and a good reversibility between fuel cell and electrolysis modes [3]. Indeed, thanks to their flexibility, SOCs can be operated in fuel cell mode (SOFC mode) to convert chemical energy directly into electricity by oxidizing fuel, such as hydrogen, natural gas, or biofuels and in electrolysis mode (SOEC mode) where the process is reversed, with electricity driving the electrolysis of water to produce hydrogen or other valuable gases. All of these benefits make SOCs a key player in the transition to a sustainable energy future. However, the SOCs durability remains one of the main issue limiting the lifetime of this technology especially in electrolysis mode (SOEC). Indeed, the cell degradation is related to microstructural evolutions in the electrodes, active site poisoning, chemical-element interdiffusion and reactivity between the cell components [4] [5] [6] [7]. Then, a deeper understanding of these degradation mechanisms based on state-of-the-art materials is crucial for developing strategies to limit performance degradation over time and make this technology fully economically competitive.

## Bibliography of the General introduction

- [1] 'IPCC, 2023: Sections. In: Climate Change 2023: Synthesis Report. Contribution of Working Groups I, II and III to the Sixth Assessment Report of the Intergovernmental Panel on Climate Change [Core Writing Team, H. Lee and J. Romero (eds.)]. IPCC, Geneva, Switzerland, pp. 35-115, doi: 10.59327/IPCC/AR6-9789291691647'.
- [2] Q. Cai, C. S. Adjiman, and N. P. Brandon, 'Optimal control strategies for hydrogen production when coupling solid oxide electrolyzers with intermittent renewable energies', *J. Power Sources*, vol. 268, pp. 212–224, Dec. 2014, doi: 10.1016/j.jpowsour.2014.06.028.
- [3] A. Godula-Jopek, *Hydrogen Production: by Electrolysis*. John Wiley & Sons, 2015.
- [4] D. Papurello, A. Lanzini, S. Fiorilli, F. Smeacetto, R. Singh, and M. Santarelli, 'Sulfur poisoning in Ni-anode solid oxide fuel cells (SOFCs): Deactivation in single cells and a stack', *Chem. Eng. J.*, vol. 283, pp. 1224–1233, Jan. 2016, doi: 10.1016/j.cej.2015.08.091.
- [5] H. Madi *et al.*, 'Solid oxide fuel cell anode degradation by the effect of siloxanes', *J. Power Sources*, vol. 279, pp. 460–471, Apr. 2015, doi: 10.1016/j.jpowsour.2015.01.053.
- [6] K. Chen and S. P. Jiang, 'Review—Materials Degradation of Solid Oxide Electrolysis Cells', *J. Electrochem. Soc.*, vol. 163, no. 11, pp. F3070–F3083, 2016, doi: 10.1149/2.0101611jes.
- [7] H. Yokokawa, H. Tu, B. Iwanschitz, and A. Mai, 'Fundamental mechanisms limiting solid oxide fuel cell durability', *J. Power Sources*, vol. 182, no. 2, pp. 400–412, Aug. 2008, doi: 10.1016/j.jpowsour.2008.02.016.

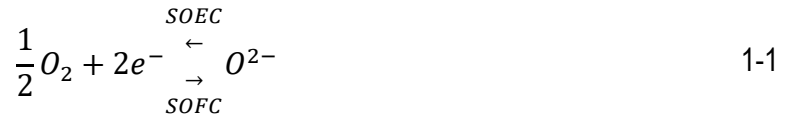
# 1. Literature review on Solid Oxide Cells (SOCs): Degradation of the hydrogen electrode

This chapter is dedicated to the technical and scientific context of the thesis and gives an overview of the Solid Oxide Cell (SOC) technology. First, the operation principles are described in both fuel cell and electrolysis modes. This chapter also presents the different architectures of the technology and the classical materials used as cell components. Moreover, the fundamentals of the solid-state electrochemistry as well as the basic reaction mechanisms occurring in the electrodes are discussed in another part. Finally, the last section of this chapter provides a review of the main degradation phenomena occurring in SOC for the different components. Based on this bibliography review, the objectives of the thesis as well as the methodology adopted are detailed at the end of the chapter.

## 1.1 SOC operation and architecture

### 1.1.1 Principle

SOCs are electrochemical devices using an oxide ion-conducting ceramic material as electrolyte, sandwiched between two porous electrodes exhibiting electronic or mixed conduction properties. The reversibility of these devices offers the possibility to work as a Solid Oxide Fuel Cell (SOFC) to produce electricity or as a Solid Oxide Electrolyzer Cell (SOEC) to produce hydrogen. On the one hand, in fuel cell mode, the reduction of the oxygen at the cathode generates oxide ions, which cross the electrolyte to be oxidized with the hydrogen at the anode to produce steam. On the other hand, in SOEC mode, the mechanism is reversed and the steam is reduced at the cathode to produce hydrogen as well as oxygen at the anode. These devices, which operate at high temperatures (700-900°C), use steam whose dissociation requires less energy compared to liquid water. Moreover, as shown in Figure 1-1, the electrical energy needed to dissociate the water molecule decreases with increasing the temperature (while the heat required for the reaction is increased). Therefore, the high-temperature electrolysis technology for hydrogen production can reach high efficiency at low cost, in particular when waste heat is available to produce the steam reactant [1]. The schematic operation principles of a SOC are shown in Figure 1-2. Considering the classical reactants and products as hydrogen, oxygen and steam, the global electrochemical reaction governing the SOC operation is deduced from the two half-reactions occurring in each electrode (equations 1-1 and 1-2 for oxygen and hydrogen electrodes respectively):



The total reaction equation is then given in equation 1-3:

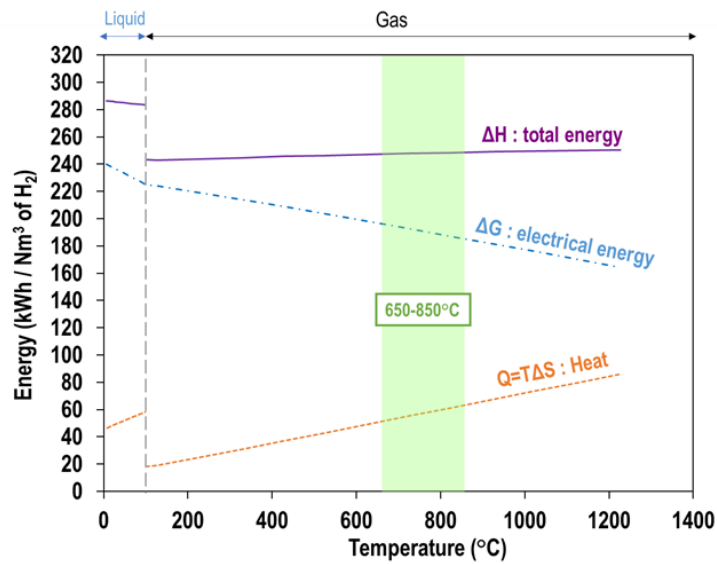
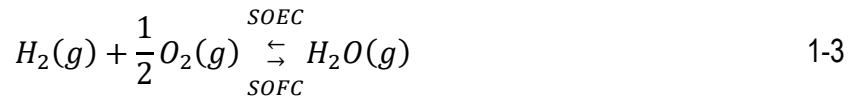


Figure 1-1: Energy need for the electrolysis reaction as a function of temperature; enthalpy ( $\Delta H$ ), Gibbs enthalpy ( $\Delta G$ ), entropy ( $T\Delta S$ ) [1].

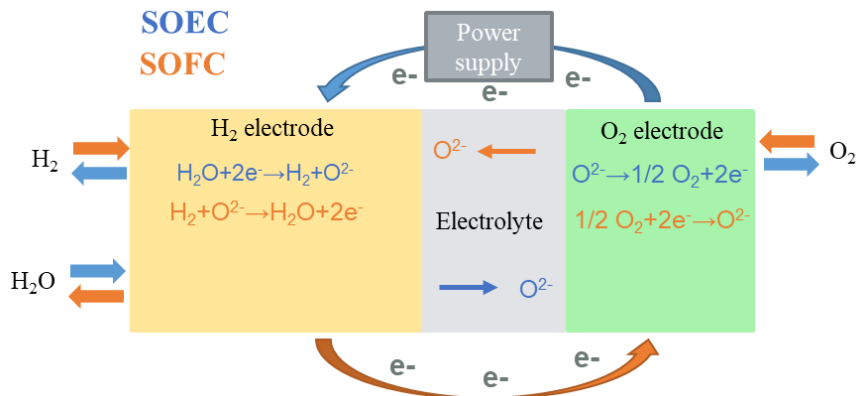


Figure 1-2: Operation principle of SOC in SOEC and SOFC modes.

### 1.1.2 Architecture

The planar and tubular configurations are the two main types of architecture for SOCs. Firstly, for the tubular architecture, the electrolyte and the two electrodes are combined to form a tube as shown in Figure 1-2 a). One of the electrode is located in the internal face of the cylinder and the other one is located on the external part (Figure 1-3, a)). In order to ensure the mechanical strength, tubular architecture can be anode supported, cathode supported or either electrolyte supported [2]. For the tubular SOEC, the cathode is located in the inner part of the tube where the steam can be reduced to hydrogen whereas the anode is located at the outer layer to extract the oxygen. [3] The current is collected by an interconnect deposited all along the tube and the cells are then assembled into bundles to form high power system. The main advantage of this design is a good mechanical robustness while avoiding gas-tight seals in the high temperature region of the system [4]. Moreover, the manufacturing method to produce the tubular cell is expensive and then increases the price of the system [4]. Secondly, the planar cells are more compact devices that present layers associated to the electrolyte and the two electrodes with square or circular shape (Figure 1-3, b)). This configuration offers also different possibilities for the mechanical support and can be electrolyte supported, hydrogen electrode supported or oxygen electrode supported. It has been shown that the hydrogen electrode supported cell offers the best compromise between electrochemical performances, mechanical robustness and manufacturing cost. The current collection and the gas distribution are ensured by a metallic interconnect. As shown in Figure 1-3 b), the two electrodes and the electrolyte together with the interconnect plates represent a Single Repeat Unit (SRU) which is assembled in series to form a stack with then higher power density. [5] [3]. Furthermore, this configuration gives the possibility to distribute air in a cross-flow configuration, additionally to classical parallel co- and counter-flow gas distributions. However, the sealing to avoid any leakage is more difficult to manage than for tubular design. Despite this issue, the planar configuration is the one, which is widely used nowadays because of its better performances, and an easier mass production [3].

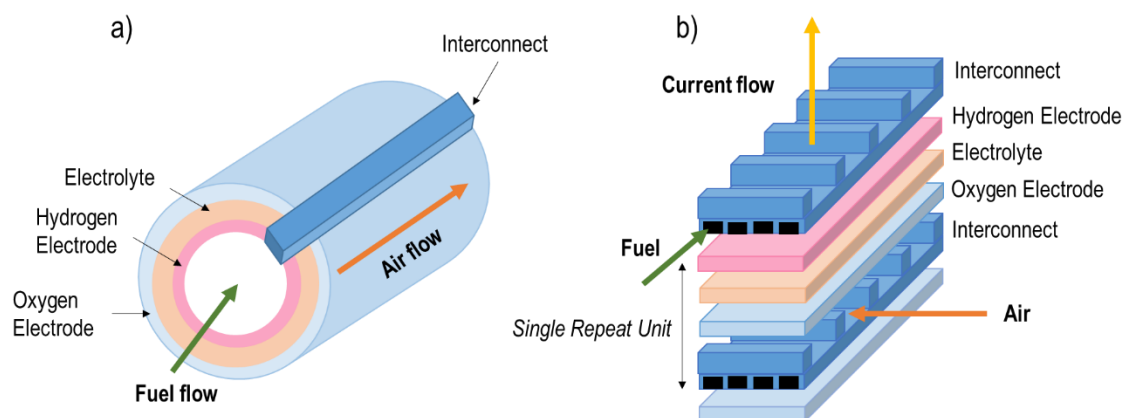


Figure 1-3: Solid Oxide Cell designs: a) tubular and b) planar.

## 1.2 Materials

### 1.2.1 Electrolyte

The choice of the electrolyte material depends on the following properties: a good ionic conductivity, a thermal expansion coefficient close to the ones of the electrodes (related to the limitation of the mechanical stress), physical and chemical stability in both oxidizing and reducing environments, high density with only closed pores and reliable mechanical properties to ensure good tightness between both gas chambers. The classical electrolyte composing SOC is a fluorite-type ceramic oxide ( $ZrO_2$ ). In particular, Yttria-Stabilised-Zirconia (YSZ) is the most commonly used material, which is generally doped with 8 mol% or 3 mol% of yttria (8YSZ or 3YSZ). Yttria is used as a dopant to stabilize the tetragonal (3YSZ) or cubic (8YSZ) structure and to create vacancies that allow the migration of oxygen ions through the volume of the material. According to the Kroger-Vink notation (equation 1-4):



Two  $Y^{3+}$  ions create one oxygen vacancy.  $2Y'_{Zr}$  (negative charge) represents two ions of  $Y^{3+}$  to replace the  $Zr^{4+}$ ,  $O_O^\times$  represents the creation of three oxygen (neutral charge) and  $V_O^{\cdot\cdot}$  (positive charge) represents the creation of an oxygen vacancy. The choice is done to achieve a good compromise between ionic conductivity and mechanical robustness. For this purpose, a doping level of 8 mol % is preferred, especially with electrode supported cell as the cell mechanical strength is not ensured by the thin electrolyte [6]. As reported in Figure 1-4, the ionic conductivity is thermally activated and is plotted as function of the temperature based on the data reported in [7]. Moreover, the table 1-1 gives the values of Thermal Expansion Coefficient (TEC) of the 8YSZ and the 3YSZ.

**Table 1-1: Thermal Expansion Coefficient (TEC)**

	TEC ( $10^{-6}/K$ ) (50-1000°C)
3YSZ	10.8 [8]
8YSZ	10.5-11 [8] [9]

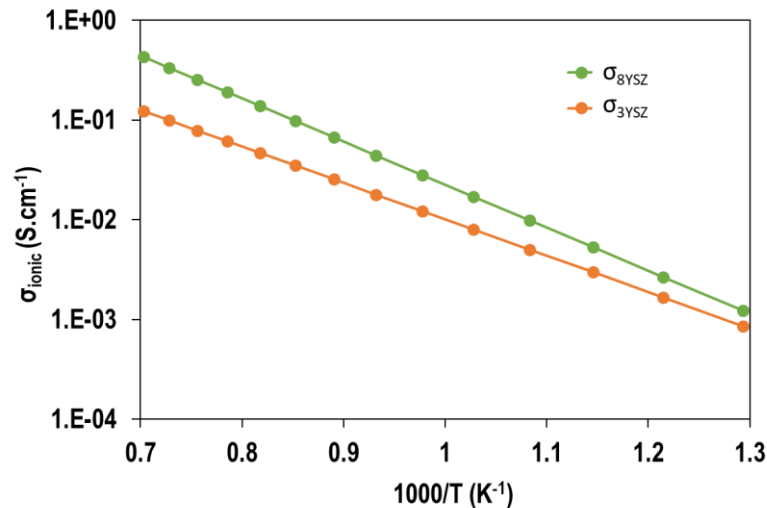


Figure 1-4: Ionic conductivity of 8YSZ and 3YSZ as a function of the operating temperature [7].

## 1.2.2 Oxygen electrode

The electrode is the place where the electrochemical reactions take place. In the SOC technology, these reactions occur at locations where the electronic, ionic and gas phases meet which are named Triple Phase Boundaries (TPBs). Therefore, the oxygen electrode must have (i) a high electronic conductivity, (ii) a thermal expansion coefficient which matches those of the electrolyte and interconnect materials, (iii) a good chemical compatibility with those neighboring components in oxidizing atmosphere, and (iv) a good porosity network for the diffusion of gaseous oxygen through the electrode from (SOEC) or to (SOFC) the electrode/electrolyte interface [10]. Thus, because of the oxidizing atmosphere at the oxygen side, it is not possible to use a cheap metal as electronic conductor. Among the existing electrode materials, the category of composite materials based on a pure electronic phase and a pure ionic one was traditionally used. The perovskite structure ( $ABO_3$ ) such as the  $La_{0.6}Sr_{0.4}Mn_{3-\delta}$  (Lanthanum Strontium Manganite (LSM)) material was classically used for its good properties of catalytic activity, electronic conductivity (table 1-2) and chemical stability. Whereas the material of the ionic phase was generally the 8YSZ or Cerium-Gadolinium Oxide (CGO or GDC). Nevertheless, in order to enhance the electrode performances another category of materials are nowadays used: the Mixed Ionic and Electronic Ceramic conductors (MIEC). Indeed, these materials present a single-phase compound for the electronic and ionic conduction (table 1-2) allowing to extend the electrochemical reactions to the whole surface (and not be limited to the TPB lines). Among these MIEC materials, the  $La_{0.6}Sr_{0.4}Co_{0.2}Fe_{0.8}O_{3-\delta}$  (Lanthanum Strontium Cobalt Ferrite-LSCF)) perovskite is the most commonly used. However, LSCF is a material which reacts with YSZ to form a non-conducting phase between the electrode and the

electrolyte [10]. Consequently, in order to limit the formation of this secondary phase, a thin layer of CGO is generally added as a diffusion barrier between LSCF and YSZ.

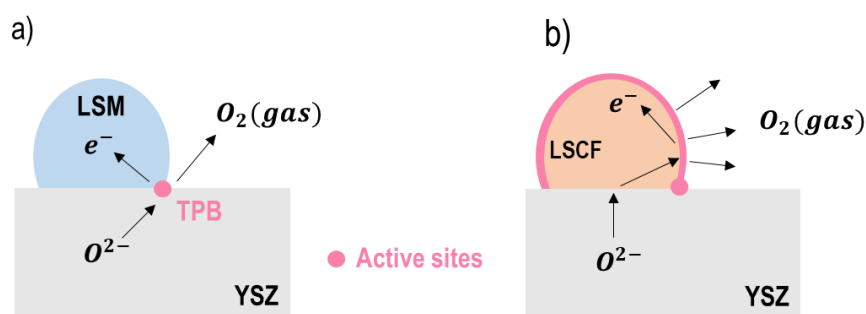


Figure 1-5: Comparison between the reaction mechanisms for a) LSM-YSZ composite and b) LSCF electrodes.

**Table 1-2: Values of the TEC, ionic and electronic conductivity of the principal oxygen electrodes materials.**

	TEC ( $10^{-6}/K$ ) (30-1000°C)	Ionic conductivity ( $S.cm^{-1}$ )	Electronic conductivity ( $S.cm^{-1}$ )
LSM	12.3 [11]	$6 \times 10^{-7}$ (900°C) [12]	$2.35 \times 10^2$ (900°C) [13]
LSCF	14-15 [14] [8]	$10^{-2}$ [8]	$3 \times 10^2$ (700°C) [15] [14]

### 1.2.3 Hydrogen electrode

The hydrogen electrode is classically made of a porous cermet of Ni for the electronic conduction (table 1-3) and YSZ for the ionic conduction, which is called Ni-YSZ cermet (Nickel-Yttria Stabilized Zirconia). The nickel is used as catalyst for hydrogen/steam oxidation/reduction in SOFC/SOEC respectively. It exhibits a very good electronic conductivity and low cost. YSZ ensures the good CET compatibility with the electrolyte. In addition, a sufficient porosity is mandatory in order to allow the diffusion of the gas species across the porous electrode. Similarly to the oxygen electrode, the electrochemical reactions take place at the TPBs where the ionic, electronic and gas phases meet. Consequently, in order to extend the TPB lines in the volume of the electrode and then improve the electrode performances, the microstructure is made of an interweaving network of Ni, YSZ and pores. The best compromise between both high electrochemical performance and good mechanical properties, especially for hydrogen electrode supported cell, is obtained with a two-layer hydrogen electrode composed by: the functional layer (FL) and the gas diffusion layer allowing a good current collection (CC) with the adjacent interconnect. The functional layer (FL), which must present a thin microstructure, is in direct contact with the electrolyte and is made of 8YSZ, which has a higher ionic conductivity than 3YSZ. The gas diffusion layer (CC) with larger

pores is usually made of 3YSZ which is more robust to ensure the mechanical support of the other cell layers [16].

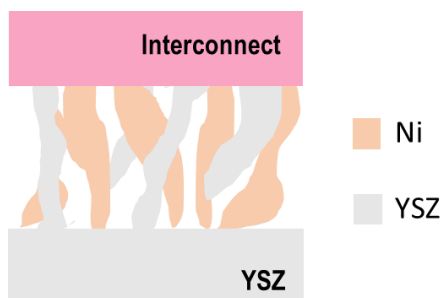


Figure 1-6: Illustration of a the Ni-YSZ cermet electrode microstructure.

**Table 1-3: Values of the TEC and electronic conductivity of the Ni used in hydrogen electrode.**

	TEC ( $10^{-6}/K$ )	Electronic conductivity ( $1000^{\circ}C$ ) ( $S.cm^{-1}$ )
Ni	13.3	$2 \times 10^{-4}$ [17]

## 1.3 Electrochemistry of the cell

### 1.3.1 Cell operation

In operation, the SOC's are affected by many reversible and irreversible phenomena inducing a modification of the cell voltage. In order to characterize the cell performances, the polarization curves ( $i$ - $V$ ) which plot the cell voltage  $E_{cell}$  as a function of the current density  $i$  are traditionally recorded. First, the Open Circuit Voltage (OCV) corresponds to the cell voltage at equilibrium  $U_{cell}(i = 0)$  without any current application. The cell voltage in open circuit condition can be expressed thanks to the Nernst law. Indeed the Nernst's equation is associated with the thermodynamically reversible processes occurring in an ideal cell and takes into account the pressures of reactants and products as follows:

$$U_{i=0}^{cell} = U^0 + \frac{RT}{zF} \ln \left( \frac{a_{H_2} (a_{O_2})^{\frac{1}{2}}}{a_{H_2O}} \right) \quad 1-5$$

$U^0$  is the cell voltage in the standard conditions,  $R$  is the universal gas constant ( $J.mol^{-1}.K^{-1}$ ),  $T$  is the absolute temperature (K),  $z$  is the number of exchanged electrons in the electrochemical reactions (i.e. 2 for a SOC operated with hydrogen and oxygen),  $F$  is the Faraday's constant ( $96485 C.mol^{-1}$ ), and  $a_{H_2}$ ,  $a_{O_2}$  and  $a_{H_2O}$  are the chemical activities of hydrogen, oxygen and steam, respectively, at the electroactive sites for  $i = 0$ .

Under current, the cell voltage deviates from the OCV due to reversible and irreversible processes. The losses are associated to the overpotential  $\eta$  arising in both polarizations according to the following equation for the cell voltage [1]:

$$U_{cell}(i) = U_{Nernst}(i) \pm \eta_{irreversible}(i) \quad \text{with } U_{Nernst} = U_{i=0}^{cell} \pm \eta_{reversible}(i) \quad 1-6$$

The reversible overpotential is associated to the gas conversion losses related to the change of the gas composition in the electrodes due to the species production and consumption. They are sometimes referred as the concentration overpotentials  $\eta_{reversible}(i) = \eta_{conc}(i)$ . Considering the electrolysis mode, the electrode overpotential consists of the increase in the electrical demand of the SOC when the current density increases (Figure 1-7). The irreversible overpotentials are the supplementary potential necessary to overcome the barrier induced by the energy dissipated by the whole electrochemical process [1]. The overpotential is negative in SOEC giving a cell voltage higher than the OCV under current whereas it is positive in SOFC giving a cell voltage lower than the OCV under current.

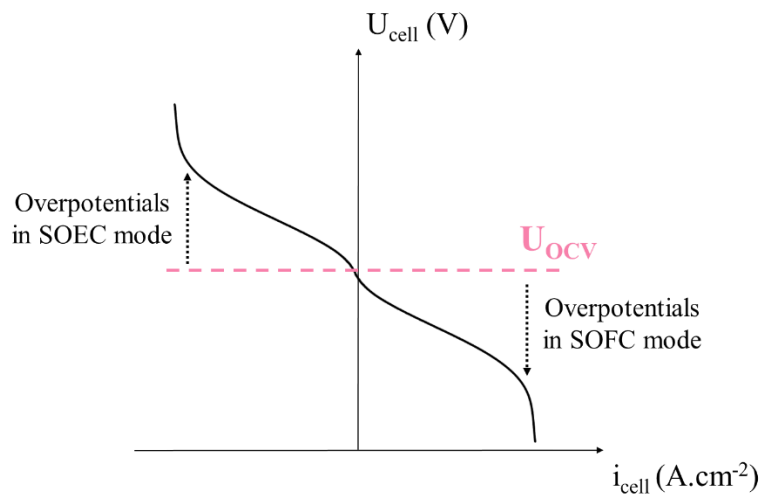


Figure 1-7: Schematic representation of an  $i$ - $U$  curve in SOEC and SOFC with the OCV and the overpotentials arising in the two operating modes.

Furthermore, the overpotential can be decomposed in different contributions depending on the current density (expressed in  $A \cdot cm^{-2}$ ) applied to the cell where  $i > 0$  in SOFC and  $i < 0$  in SOEC mode [1]:

$$U_{cell} = U_{Nernst}(i) \pm \eta_{ohmic}(i) \pm \eta_{diff}^{O_2 electrode}(i) \pm \eta_{diff}^{H_2 electrode}(i) \pm \eta_{act}^{O_2 electrode}(i) \pm \eta_{act}^{H_2 electrode}(i) \quad 1-7$$

The first contribution ( $\eta_{ohmic}(i)$ ) is associated with the ohmic resistance, which corresponds to the material resistance due to the passage of the flow of electrons in the electrodes and the flow of ions in the electrolyte. Moreover, the contact resistance between the electrodes and the current collectors also

contributes to the ohmic resistance. The ohmic overpotential can be describe using the classical Ohm's law, where  $R_s$  ( $\Omega \cdot \text{cm}^2$ ) expressed the general ohmic resistance of the complete cell [18].

$$\eta_{ohmic} = R_s \times i \quad 1-8$$

The second  $\eta_{diff}^{O_2 electrode}(i)$  and third  $\eta_{diff}^{H_2 electrode}(i)$  terms represent the respective diffusion overpotentials of the  $O_2$  and  $H_2$  electrodes caused by the limitation of the gas transport inside the porous electrode. The microstructure of the electrode and especially the arrangement of the porosity phase play a key role on the gas diffusion in the electrode [19].

The two last terms  $\eta_{act}^{O_2 electrode}(i)$  and  $\eta_{act}^{H_2 electrode}(i)$  are the activation overpotentials of the  $O_2$  and  $H_2$  electrodes. These last contributions are induced by the electrochemical reactions in the electrode active layers. The activation overpotential is expressed with the phenomenological Butler-Volmer relation:

$$i = i_0 \left\{ \exp\left(\frac{\alpha z F}{RT} \eta_{act(i)}\right) - \exp\left(-\frac{(1-\alpha) z F}{RT} \eta_{act(i)}\right) \right\} \quad 1-9$$

With  $\alpha$  the symmetrical transfer coefficient (usually equal to 0.5) and  $i_0$  the 'apparent' exchange current density depending on the operating temperature and the gas partial pressures [1].

Complementary to the polarization curves (i-U), the Electrochemical Impedance Spectroscopy (EIS) is a method that allows to study and characterize the phenomena occurring in the SOC, which differ in characteristic time constants and frequency responses. This method is based on the application of a small sinusoidal electrical perturbation to the system and the measure of the output signal, which will have the same frequency but a shifted phase and a different amplitude [20]. In order to display the evolution of the induced impedance, the Nyquist plot (the imaginary part of the impedance as a function of the real part) and Bode plot (the imaginary part as a function of the frequency) are commonly used. From the Nyquist plot, it is possible to obtain the serial resistance ( $R_s$ ) attributed to the ohmic contribution, which is the high frequency intercept with the real axis. Moreover, the plot gives the total resistance ( $R_{tot}$ ) which is the intercept at low frequency with the real axis and gives the steady-state resistance of the system. Finally, the polarization resistance ( $R_p$ ) is obtained by subtracting the serial resistance to the total resistance.

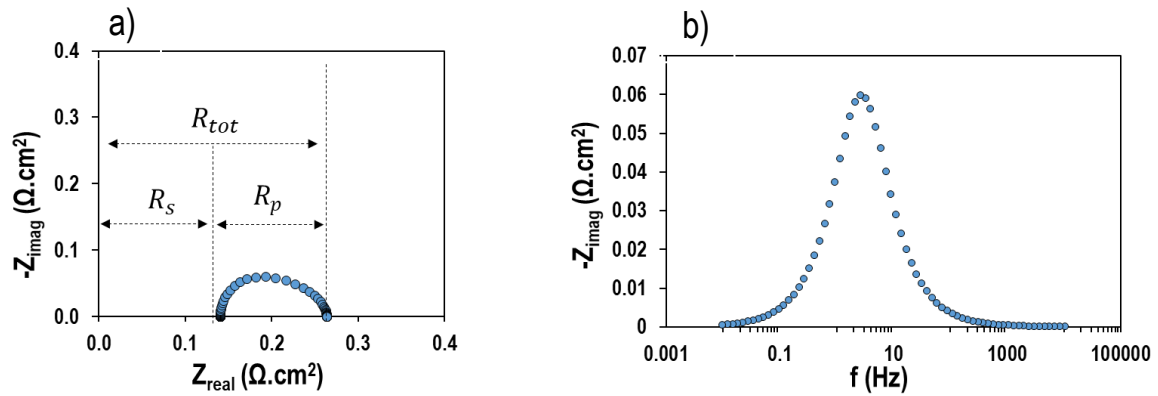


Figure 1-8: Classical representation of the impedance spectra a) Nyquist plot and b) Bode plot.

### 1.3.2 Reaction Mechanism for the Hydrogen Electrode

To study the reaction mechanism of the hydrogen electrode, a coupled experimental (using the polarization curves as well as the Electrochemical Impedance Spectra) and modeling approach is employed at the electrode scale in this work. It is worth noting that the complex Ni-YSZ microstructure can affect the reaction mechanism [21]. Focusing on the Ni-8YSZ cermet, it has been shown that the electrode reaction mechanism is strongly thermally-activated and its kinetic rate is proportional to the density of active TPBs [22]. Moreover, the charge transfer at TPBs should limit the overall electrode response [23]. From the study of the electrode polarization curves in both SOEC and SOFC modes, a strong dissymmetry between the two branches has been detected with a higher polarization resistance in cathodic polarization compared to the anodic one [24]. Finally, the study of the impact of the partial pressures has shown that the  $p_{\text{H}_2\text{O}}$  has a strong effect on the kinetic rates whereas the  $p_{\text{H}_2}$  effect is less pronounced [25]. According to [25], the interaction of steam molecules with the Ni and YSZ surfaces could co-limit the global kinetics. In a complementary way, modeling has been used to investigate the electrode reaction mechanism. The Density Functional Theory has been employed by several authors to study the interaction of steam and hydrogen with the Ni-YSZ cermet [26] [27]. Indeed, the most energetically favorable configuration consists in an adsorption of  $\text{H}_2$  molecules as two hydrogen adatoms on the Ni surface when  $\text{H}_2\text{O}$  molecules can be adsorbed on both Ni and YSZ surfaces. From the coupled DFT calculations and experimental analysis, two main mechanisms have been proposed: an oxygen spillover or a hydrogen spillover mechanism as represented on Figure 1-9.

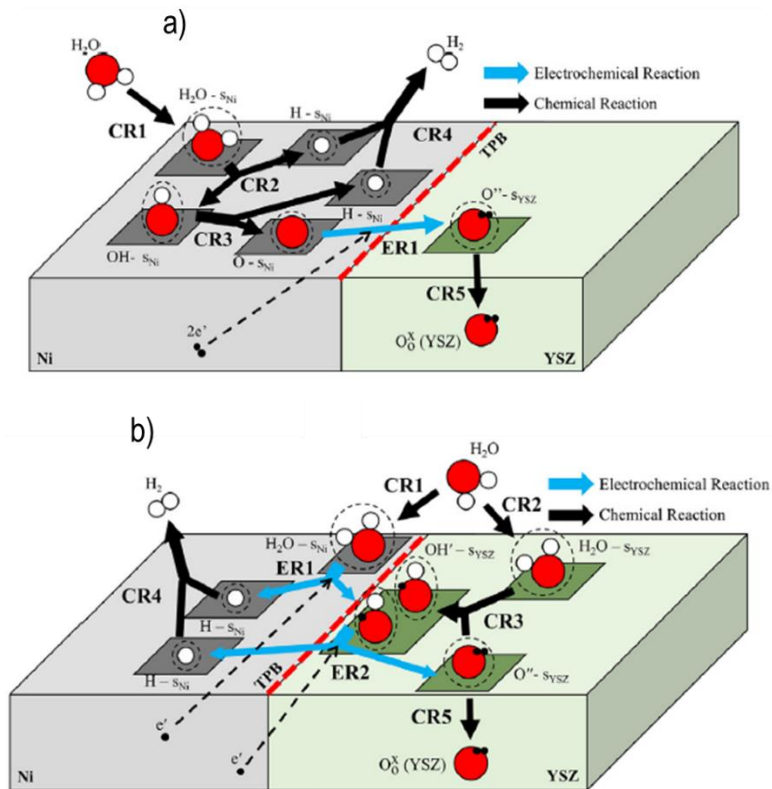


Figure 1-9: Representation of a) the oxygen spillover and b) the hydrogen spillover mechanisms [28].

In the oxygen spillover mechanism, under electrolysis mode, the steam can only interact with the Ni. The adsorption of steam on the Ni produces a hydroxyl and a hydrogen adatom on the Ni surface. The dissociation of the hydroxyl leads to an adsorbed oxygen and a second hydrogen adatom, which reacts with the first one to produce the  $H_2$  molecule. The charge transfer allows the production of the oxygen ions, which are incorporated in the YSZ lattice. In fuel cell mode, the reverse mechanism occurs. Concerning the hydrogen spillover mechanism, it implies two parallel pathways where the steam can interact with both Ni and YSZ surfaces whereas  $H_2$  interacts only with Ni. Under electrolysis mode, in the first pathway, the steam is reduced to form one H on the Ni surface and one  $OH^-$  on the YSZ surface. The second pathway allows the production of the second H species on the Ni surface by the adsorption of the steam on the YSZ surface and the reduction of the  $OH^-$ . Then, the two H species are associated to produce a  $H_2$  molecule and the oxygen ions are incorporated into the YSZ lattice. It has been shown that the hydrogen spillover mechanism is the most relevant mechanism to predict correctly the electrode response [29] [30] [9].

## 1.4 Cell degradations

During high temperature operation, the cell is subjected to the ageing of materials that induces degradations. Indeed, the SOC's durability remains one of the main issues limiting the deployment of the technology especially in electrolysis mode (SOEC). The degradation rates in performances for the cells made of the state-of-the-art materials are less than around  $\approx 1$  %/kh in fuel cell mode (SOFC) whereas they can reach up to  $\approx 2-3$  %/kh when operated under electrolysis current [31] [32] [33] [34] [35] [36] [37]. The cell degradations are related to material instabilities, which are triggered by the high operating temperature and the polarization. They can have several origins, such as microstructural evolutions in the electrodes, active sites poisoning, chemical-element interdiffusion and reactivity between the cell components [38] [39] [40] [41].

### 1.4.1 Electrolyte

The electrolyte is subjected to different degradation phenomena. One of them, the phase transformation from the cubic to the tetragonal YSZ induces a decrease of its ionic conduction. This phase transformation is attributed to the initial nickel diffusion into the electrolyte during the co-sintering with the hydrogen electrode [42]. However, this phenomenon seems to be limited. Nano-porosities are also usually detected at the grain boundaries close to the CGO barrier layer / electrolyte interface. According to Laurencin et al. [43], these nano-porosities could come from the loss of  $Zr^{4+}$  associated to the formation of poorly conductive zirconates at the interface between the electrolyte and the CGO barrier layer. Other works [44] also suggested that the precipitation of  $SrZrO_3$  at the CGO barrier layer / electrolyte interface could induce the migration of  $Zr^{4+}$  cations toward the CGO barrier YSZ leaving nano-porosities at the electrolyte grain boundaries close to this interface.

### 1.4.2 Oxygen electrode

A significant part of the cell degradation is attributed to degradation phenomena occurring in the oxygen electrode. Among these phenomena, the demixing of the LSCF is one of the main degradation contributions to the overall degradation of the SOC's. The LSCF demixing is associated to the release and the migration of strontium to the LSCF surface and the consequent reactivity with the electrolyte material. This phenomenon causes the formation of insulating phases such as strontium zirconates ( $SrZrO_3$ ) at the barrier layer interface with the electrolyte and a strontium oxide (SrO) on the LSCF surface. This degradation phenomenon would be accelerated in electrolysis mode since the accumulation of oxygen incorporated atoms in the LSCF could be the driving force for Sr segregation and formation of strontium

oxide on the electrode surface [43]. In order to limit the reactivity between the LSCF and the YSZ, a GDC layer is added in-between. Consequently, an Inter-Diffusional Layer (IDL) with a lower ionic conductivity is usually detected between the GDC and the YSZ. This IDL is formed during sintering of cell manufacturing and could act as a protective layer to limit the formation of strontium zirconate. It has been shown that this IDL could contribute to the increase of the ohmic losses in SOCs [45]. Additionally, the delamination at the electrolyte interface is another degrading mechanism of the oxygen electrode. This degradation consists of a detachment of the oxygen electrode from the electrolyte, which is specific of the LSM-YSZ composite. The delamination is due to the high oxygen partial pressure in the reaction zone close to the electrolyte when the cell is operated in electrolysis operation or is induced by thermomechanical stresses at the interface with the electrolyte [46] [47]. Finally, the oxygen electrode is subjected to Cr poisoning. The poisoning of the oxygen electrode is caused by the deposition of chromium coming from the interconnects. Chromium can diffuse into the electrode as volatile species, forming insulating phases such as chromia ( $\text{Cr}_2\text{O}_3$ ) on reaction sites. Moreover, the Cr can react with the strontium contained in the electrode material to form  $\text{SrCrO}_x$ , which implies a decrease of the electrode performances. This phenomenon could be limited by using dry air in the gas flow because the presence of steam increases the formation of volatile chromium-based species [48] and by depositing a protective coating on the neighbouring interconnect.

### 1.4.3 Hydrogen electrode

Considering the hydrogen electrode, it is worth noting that an important part of the electrode performance loss is caused by two main degradation mechanisms. First, the presence of impurities in the hydrogen electrode can affect the degradation. Indeed the glass sealing used for the gas tightness of test rigs and SOFC/SOEC stacks contains silica ( $\text{SiO}_2$ ), as well as the cell raw materials, that can be transported in the gas stream to be deposited at the TPBs [49]. Specifically, the Si is transported in the gas phase as hydroxide species ( $\text{Si}(\text{OH})_4$ ) and the phenomenon is accelerated with higher steam content. However, this poisoning can be limited by cleaning the inlet gases and pretreating the seal. Apart from the poisoning of the Ni-YSZ based hydrogen electrode by impurities, the morphological evolution of the Ni microstructure remains one of the main problems of the SOC durability. In fact, the Ni that ensures the electronic conductivity is subjected to coarsening and migration to the electrode volume. These evolutions of the microstructure lead to an important decrease of the TPB Lines (TBLs) that plays negatively on the cell performances.

## 1.5 The morphological evolution of the Ni

As mentioned in the last section 1.4.3, the Ni-YSZ electrode is subjected to a Ni agglomeration and migration in operation. Specifically, the Ni particles in the cermet are not stable in operation and their rearrangement in the microstructure can affect significantly the cell response. The coarsening of Ni is due to a local agglomeration related to the growth of the biggest particles to the detriment of the smallest ones [50]. It is characterized by an increase of the Ni mean particle diameter because of the sintering of the smallest ones. This behavior is purely thermally activated and is usually observed after operation in both SOFC and SOEC modes, i.e. under both anodic and cathodic polarizations. Ni coarsening is ascribed to an Arrhenius-type Ostwald ripening process associated to surface diffusion of Ni particles. This phenomenon induces a decrease of the Triple Phase Boundary (TPB) lines, where the ionic, electronic and gas phases meet, decreasing the number of active sites available for the electrochemical reactions. Nevertheless, it has been shown that the Ni agglomeration tends to slow down for long-term operation and can contribute up to 25 - 30% of the total loss in performances [51].

Aside from the local particle coarsening, Ni redistribution over long distance can also arise in the cermet. At very high temperature above 950°C, it has been shown that Ni can relocate at electrolyte interface in electrolysis mode [32]. However, a reverse trend is usually observed at the more classical SOEC operating temperature below 900°C. Indeed, a substantial Ni migration away from the electrolyte interface is observed in electrolysis mode, even after a relatively short-term operation [52]. For instance, Trini et al. [53] and Monaco et al. [54] both have detected a fully depleted layer of Ni at the electrolyte interface for cells operated at 800°C for 1000 h at a current density of respectively -0.5 A.cm<sup>-2</sup> and -1 A.cm<sup>-2</sup> and a steam conversion of 16% and 56% (Figure 1-10).

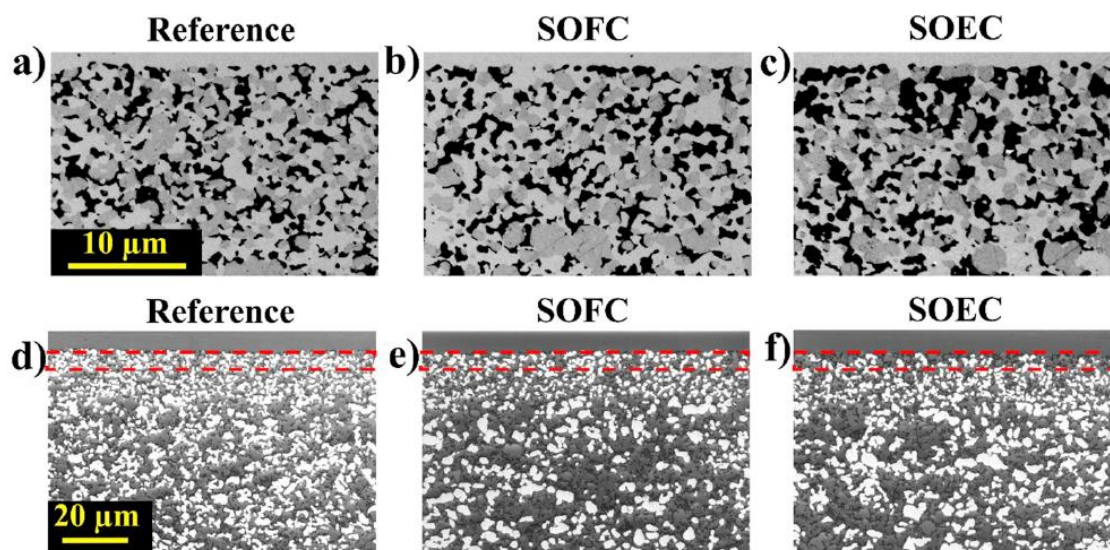


Figure 1-10: SEM images of three samples: reference a) and d), SOFC b) and e), and SOEC c) and f). In the low voltage ESB images a)-c) porosity is black, YSZ is lightgray, and Ni is dark gray. In the low voltage images recorded with the Inlens detector d)-f) porosity is black, YSZ and non-percolating Ni are gray and the percolating Ni is white. The dashed lines in d)-f) indicate the area where the decrease of percolating Ni is more visible [53].

On the contrary, as reported by Menzler et al. [55], a slight Ni enrichment can occur in fuel cell mode, which was only detected after a very long-term operation of 100,000 h at 700°C, a current density of 0.5 A.cm<sup>-2</sup> and a fuel utilization of 40%. It can be noticed that the Ni depletion in SOEC operation is also concomitant with some detachments of Ni particles from YSZ [56]. Moreover, it has been shown that the cermet microstructure plays a key role in the Ni migration. Indeed, a finer microstructure in the active layer seems to mitigate in part the Ni redistribution [57]. In electrolysis mode, the depleted layer of Ni in the vicinity of the electrolyte interface is responsible of a noticeable increase in the ohmic cell resistance [58]. The Ni migration also leads to a gradient of TPBs in the depth of the electrode that increases the cell polarization resistance [54]. Therefore, the Ni migration in electrolysis mode is considered as one of the most detrimental phenomena that must partially explain the difference in durability behavior between SOFC and SOEC modes. Even if the underlying mechanisms involved in the Ni migration are still not precisely understood, different scenarios have been already reported in the literature. Mogensen et al. [52] [59] have initially proposed a mechanism based on the migration of Ni via the phase gas. Depending on the working temperature (below or above 950°C), two cases must be considered. As mentioned below, for temperatures higher than 950°C, the Ni seems to migrate down the gradient of p<sub>H<sub>2</sub>O</sub> towards the electrolyte. In this case, Ni can be evaporated under Ni(OH)<sub>2</sub> molecules that can diffuse up to the electrolyte interface in electrolysis mode as shown in Monaco et al. [54]. Below 950°C, Mogensen et al. have proposed that the electrode is deactivated under cathodic polarization due to precipitation of contaminants at the TPBs (such as Silicon), reduction of impurities at the Ni/YSZ interface causing

delamination, loss of percolation due to the coarsening [52]. In the zone without electrochemistry, the gradient in  $\text{Ni}(\text{OH})_x$  partial pressure is reversed so that Ni can be transported by surface diffusion towards the new active region. However, Ni migration has been also observed under  $\text{CO}_2$  electrolysis without steam. Therefore, the Ni transport via hydroxyl species cannot explain the migration. To overcome this difficulty, Mogensen et al. have very recently proposed that the migration could involve  $\text{Ni}^+$  species attached on the YSZ surface that migrate under the electrical field [60]. This mechanism can also take place in SOFC mode with a migration down to the electrolyte interface. When the mechanism is controlled by surface diffusion at the classical operating temperatures (below  $950^\circ\text{C}$ ), Trini et al. [53] have suggested that Ni migration could be driven by the gradient in oxygen partial pressures associated to the local electrode polarizations arising in the electrode thickness. This gradient induces a variation of Ni wettability on YSZ depending on the position in the electrode. In electrolysis mode, the low wettability of Ni onto YSZ at the electrolyte interface induces a Ni migration towards the bulk of the electrode. The reverse gradient arising in fuel cell mode must account for the Ni relocation at the electrolyte interface. Nevertheless, in spite of the lower anodic polarizations with respect to the cathodic ones [53], this mechanism should lead to significant Ni migration towards the electrolyte interface in fuel cell mode, which is not experimentally observed [55]. Moreover, the wettability gradients calculated in SOEC mode with this hypothesis are insufficient to account for a substantial Ni depletion [61]. In that condition, this mechanism based on the Ni surface tension does not seem to play a major role in the Ni redistribution in porous electrode microstructure. In parallel, Nakajo et al. [62] have suggested that the mechanism could be related to an electrocapillarity phenomenon [63]. In this pure thermodynamic approach, the Ni/YSZ interfacial energy must also be affected by the electrode potential. Nevertheless, according to the Young–Lippmann equation, the Ni wettability onto YSZ should increase at high polarization in both electrolysis and fuel cell modes. In other words, as mentioned in [59], the effect of polarization must “result in a fairly symmetrical decrease of the interfacial energy around the electrocapillary maximum”. This evolution seems to contradict the experimental observations and cannot explain the Ni redistribution in each operating mode. Recently, Cheng et al. have proposed that the oxidation and reduction of Ni during operation at the electrolyte interface can also facilitate the coarsening and gas transport of Ni and then contribute to the relocalisation of Ni [64]. Finally, Monaco et al. [54] have suggested that the mechanism could be linked to the accumulation of charges in the electrochemical double layer at the Ni/YSZ interface. In SOEC mode, the strong accumulation of oxygen vacancies in the YSZ at the Ni/YSZ interface could decrease the Ni wettability onto YSZ. Conversely, the depletion of vacancies in SOFC mode should not affect significantly the wettability. It can be noticed that the Ni detachment observed after operation in electrolysis mode could also be explained by the decrease of the wetting behavior of the Ni/ YSZ interface related to a

decrease of the work of adhesion. Despite their differences, it is worth noting that all the mechanisms assume that the gradient in local polarization across the electrode controls the Ni migration.

## 1.6 Conclusion

This chapter was an overview of the state-of-the-art of the SOCs. A first section was dedicated to the description of the operation principles of this technology as well as the different architectures and materials used. It appears that SOCs are a promising technology for a clean production of energy (electricity and fuels) and a clean storage of electricity using hydrogen. The reaction mechanisms that occur in the electrodes are more complex and need more investigations to be fully understood. Moreover, despite many advantages the cell performances of SOCs need to be improved to make this technology economically more competitive and facilitate its industrialisation. In operation, many degradations arising in both electrodes are responsible of the decrease in cell performances. The morphological evolution of the Ni and especially the Ni migration in the Ni-YSZ cermet hydrogen electrode is among the most important degradation phenomena. However, the Ni migration mechanism is under debate and needs deeper understanding. Moreover, the contribution of this phenomenon to the total cell degradation remains unevaluated. Furthermore, relevant microstructural optimization should be very useful to mitigate the degradation. In this context, as a necessary step in this direction, this thesis aims to provide a better understanding of the Ni migration in both SOEC and SOFC modes via the modeling and discussion of an alternative mechanism that combines the evolutions of the electrochemical double layer and the Ni wettability on YSZ. To this end, a trifold experimental, post-test characterization and modelling approach has been used. First, long-term tests have been performed on classical CEA hydrogen electrode-supported cells in different operating conditions (mode, temperature and ageing time) in order to get electrochemical characterizations (i-U curves and EIS) necessary to the development of the models. After the durability tests, the microstructural properties are studied by FIB-SEM 3D reconstructions and SEM/EDX analysis in comparison with the pristine cell. These data are used as inputs in a multi-scale model calibrated and validated to reproduce the cell performances. This model is then coupled with a phase-field model that has been developed in this work to simulate the Ni migration in the hydrogen electrode and better understand this degradation phenomenon. In this frame, the chapter 2 provides a clear and detailed presentation of the tools used in this work; based on a series of experimental tests in different operating conditions, post-test characterization involving MEB images and FIB-SEM reconstructions as well as a set of numerical tools to obtain all the microstructural properties of the reconstructed volumes. In addition, a multi-scale electrochemical model has been used in this work to address the gradients of contact angles between the Ni and YSZ. All the experimental results are

presented and analyzed in chapter 3. Finally, chapter 4 is dedicated to the developed phase-field model for the simulation of the Ni migration in both SOEC and SOFC modes based on the original mechanism studied in this work. Moreover, this proposed mechanism to understand (at least part of) the Ni migration is intensively described in this part. The results of the simulation and the elements of validation of the mechanism are then presented and discussed in a final section.

## Bibliography of chapter 1

- [1] A. Godula-Jopek, *Hydrogen Production: by Electrolysis*. John Wiley & Sons, 2015.
- [2] N. M. Sammes and Y. Du, 'Fabrication and Characterization of Tubular Solid Oxide Fuel Cells', *Int. J. Appl. Ceram. Technol.*, vol. 4, no. 2, pp. 89–102, 2007.
- [3] M. Ni, M. Leung, and D. Leung, 'Technological development of hydrogen production by solid oxide electrolyzer cell (SOEC)', *Int. J. Hydrog. Energy*, vol. 33, no. 9, pp. 2337–2354, May 2008, doi: 10.1016/j.ijhydene.2008.02.048.
- [4] J. Larminie and A. Dicks, *Fuel cell systems explained*, 2nd ed. Chichester, West Sussex: J. Wiley, 2003.
- [5] V. Birss, E. El Sawy, S. Ketabi, P. Keyvanfar, X. Li, and J. Young, 'Electrochemical Energy Production Using Fuel Cell Technologies', in *Handbook of Industrial Chemistry and Biotechnology*, J. A. Kent, T. V. Bommaraju, and S. D. Barnicki, Eds., Cham: Springer International Publishing, 2017, pp. 1729–1779. doi: 10.1007/978-3-319-52287-6\_32.
- [6] C. Suci, E. Dorolti, and A. C. Hoffmann, 'Physico-chemical properties of nanocrystalline YSZ powders as a function of doping level and electrical properties after sintering', *Mater. Sci. Energy Technol.*, vol. 1, no. 2, pp. 136–145, Dec. 2018, doi: 10.1016/j.mset.2018.06.007.
- [7] E. Lay-Grindler, J. Laurencin, G. Delette, J. Aicart, M. Petitjean, and L. Dessemond, 'Micro modelling of solid oxide electrolysis cell: From performance to durability', *Int. J. Hydrog. Energy*, vol. 38, no. 17, pp. 6917–6929, Jun. 2013, doi: 10.1016/j.ijhydene.2013.03.162.
- [8] B. Fan, J. Yan, and X. Yan, 'The ionic conductivity, thermal expansion behavior, and chemical compatibility of La<sub>0.54</sub>Sr<sub>0.44</sub>Co<sub>0.2</sub>Fe<sub>0.8</sub>O<sub>3-d</sub> as SOFC cathode material', pp. 1835–1839, 2011.
- [9] F. Tietz, 'Thermal Expansion of SOFC Materials', *Ionics*, vol. 5, p. 129, 1999.
- [10] C. Sun, R. Hui, and J. Roller, 'Cathode materials for solid oxide fuel cells: a review', *J. Solid State Electrochem.*, vol. 14, no. 7, pp. 1125–1144, Jul. 2010, doi: 10.1007/s10008-009-0932-0.
- [11] M. Mori, N. M. Sammes, E. Suda, and Y. Takeda, 'Application of La<sub>0.6</sub>Ae<sub>0.4</sub>MnO<sub>3</sub> (Ae=Ca and Sr) to electric current collectors in high-temperature solid oxide fuel cells', *Solid State Ion.*, vol. 164, pp. 1–15, 2003.
- [12] S. Carter, A. Selcuk, R. J. Chater, J. Kajda, J. A. Kilner, and B. C. H. Steele, 'Oxygen transport in selected nonstoichiometric perovskite-structure oxides', *Solid State Ion.*, vol. 53–56, pp. 597–605, 1992.
- [13] S. Paydar, M. H. Shariat, and S. Javadpour, 'Investigation on electrical conductivity of LSM/YSZ8, LSM/Ce<sub>0.84</sub>Y<sub>0.16</sub>O<sub>0.96</sub> and LSM/ Ce<sub>0.42</sub>Zr<sub>0.42</sub>Y<sub>0.16</sub>O<sub>0.96</sub> composite cathodes of SOFCs', *Int. J. Hydrog. Energy*, no. 41, pp. 23145–23155, 2016.
- [14] L.-W. Tai, M. M. Nasrallah, H. U. Anderson, D. M. Sparlin, and S. R. Sehlin, 'Structure and electrical properties of La<sub>1-x</sub>Sr<sub>x</sub>Co<sub>1-y</sub>FeyO<sub>3</sub>. Part 2. The system La<sub>1-x</sub>Sr<sub>x</sub>Co<sub>0.2</sub>Fe<sub>0.8</sub>O<sub>3</sub>', *Solid State Ion.*, vol. 76, pp. 273–283, 1994.
- [15] E. Effori, J. Laurencin, E. Silva Da Rosa, M. Hubert, T. David, M. Petitjean, G. Geneste, L. Dessemond and E. Siebert, 'An Elementary Kinetic Model for the LSCF and LSCF-CGO Electrodes of Solid Oxide Cells: Impact of Operating Conditions and Degradation on the Electrode Response', *J. Electrochem. Soc.*, vol. 168, no. 4, p. 044520, Apr. 2021, doi: 10.1149/1945-7111/abf40a.
- [16] M. Ghatee, M. H. Shariat, and J. T. S. Irvine, 'Investigation of electrical and mechanical properties of 3YSZ/8YSZ composite electrolytes', *Solid State Ion.*, vol. 180, no. 1, pp. 57–62, Feb. 2009, doi: 10.1016/j.ssi.2008.10.006.
- [17] B. Shri Prakash, S. Senthil Kumar, and S. T. Aruna, 'Properties and development of Ni\_YSZ as an anode material in solid oxide fuel cell: A review', pp. 149–179, 2014.
- [18] Y. Patcharavorachot, A. Arpornwichanop, and A. Chuachuensuk, 'Electrochemical study of a planar solid oxide fuel cell: Role of support structures', *J. Power Sources*, vol. 177, no. 2, pp. 254–261, Mar. 2008, doi: 10.1016/j.jpowsour.2007.11.079.

- [19] L. Holzer, B. Iwanschitz, Th. Hocker, B. Münch, M. Prestat, 'Microstructure degradation of cermet anodes for solid oxide fuel cells: Quantification of nickel grain growth in dry and in humid atmospheres', *J. Power Sources*, vol. 196, no. 3, pp. 1279–1294, Feb. 2011, doi: 10.1016/j.jpowsour.2010.08.017.
- [20] A. Nechache, M. Cassir, and A. Ringuedé, 'Solid oxide electrolysis cell analysis by means of electrochemical impedance spectroscopy: A review', *J. Power Sources*, vol. 258, pp. 164–181, Jul. 2014, doi: 10.1016/j.jpowsour.2014.01.110.
- [21] J. Hanna, W. Y. Lee, Y. Shi, and A. F. Ghoniem, 'Fundamentals of electro- and thermochemistry in the anode of solid-oxide fuel cells with hydrocarbon and syngas fuels', *Prog. Energy Combust. Sci.*, vol. 40, pp. 74–111, Feb. 2014, doi: 10.1016/j.pecs.2013.10.001.
- [22] M. C. Doppler, J. Fleig, M. Bram, and A. K. Opitz, 'Hydrogen oxidation mechanisms on Ni/yttria stabilized zirconia anodes: Separation of reaction pathways by geometry variation of pattern electrodes', *J. Power Sources*, vol. 380, pp. 46–54, Mar. 2018, doi: 10.1016/j.jpowsour.2018.01.073.
- [23] Y. Luo, W. Li, Y. Shi, Y. Wang, and N. Cai, 'Reversible H<sub>2</sub>/H<sub>2</sub>O electrochemical conversion mechanisms on the patterned nickel electrodes', *Int. J. Hydrog. Energy*, vol. 42, no. 40, pp. 25130–25142, Oct. 2017, doi: 10.1016/j.ijhydene.2017.08.138.
- [24] O. A. Marina, L. R. Pederson, M. C. Williams, G. W. Coffey, K. D. Meinhardt, C. D. Nguyen and E.C. Thomsen, 'Electrode Performance in Reversible Solid Oxide Fuel Cells', *J. Electrochem. Soc.*, vol. 154, no. 5, p. B452, 2007, doi: 10.1149/1.2710209.
- [25] H. P. Dasari, S.-Y. Park, J. Kim, J.-H. Lee, B.-K. Kim, H.-W. Je and K. J. Yoon, 'Electrochemical characterization of Ni–yttria stabilized zirconia electrode for hydrogen production in solid oxide electrolysis cells', *J. Power Sources*, vol. 240, pp. 721–728, Oct. 2013, doi: 10.1016/j.jpowsour.2013.05.033.
- [26] D. T. Chaopradith, D. O. Scanlon, and C. R. A. Catlow, 'Adsorption of Water on Yttria-Stabilized Zirconia', *J. Phys. Chem. C*, vol. 119, no. 39, pp. 22526–22533, Oct. 2015, doi: 10.1021/acs.jpcc.5b06825.
- [27] A. Cadi-Essadek, A. Roldan, and N. H. de Leeuw, 'Density functional theory study of the interaction of H<sub>2</sub>O, CO<sub>2</sub> and CO with the ZrO<sub>2</sub> (111), Ni/ZrO<sub>2</sub> (111), YSZ (111) and Ni/YSZ (111) surfaces', *Surf. Sci.*, vol. 653, pp. 153–162, Nov. 2016, doi: 10.1016/j.susc.2016.06.008.
- [28] F. Monaco, E. Effori, M. Hubert, E. Siebert, G. Geneste, B. Morel, E. Djurado, D. Montinaro and J. Laurencin, 'Electrode kinetics of porous Ni-3YSZ cermet operated in fuel cell and electrolysis modes for solid oxide cell application', *Electrochimica Acta*, vol. 389, p. 138765, Sep. 2021, doi: 10.1016/j.electacta.2021.138765.
- [29] W. G. Bessler, M. Vogler, H. Störmer, D. Gerthsen, A. Utz, A. Weber and E. Ivers-Tiffée 'Model anodes and anode models for understanding the mechanism of hydrogen oxidation in solid oxide fuel cells', *Phys. Chem. Chem. Phys.*, vol. 12, no. 42, p. 13888, 2010, doi: 10.1039/c0cp00541j.
- [30] D. G. Goodwin, H. Zhu, A. M. Colclasure, and R. J. Kee, 'Modeling Electrochemical Oxidation of Hydrogen on Ni–YSZ Pattern Anodes', *J. Electrochem. Soc.*, vol. 156, no. 9, p. B1004, 2009, doi: 10.1149/1.3148331.
- [31] L. Blum, U. Packbier, I. C. Vinke, and L. G. J. de Haart, 'Long-Term Testing of SOFC Stacks at Forschungszentrum Jülich', *Fuel Cells*, vol. 13, no. 4, pp. 646–653, Aug. 2013, doi: 10.1002/face.201200151.
- [32] A. Hauch, S. D. Ebbesen, S. H. Jensen, and M. Mogensen, 'Solid Oxide Electrolysis Cells: Microstructure and Degradation of the Ni/Yttria-Stabilized Zirconia Electrode', *J. Electrochem. Soc.*, vol. 155, no. 11, p. B1184, Sep. 2008, doi: 10.1149/1.2967331.
- [33] T. L. Skafte, J. Hjelm, P. Blennow, and C. Graves, 'Quantitative review of degradation and lifetime of solid oxide cells and stacks', p. 20, 2016.
- [34] C. E. Frey, Q. Fang, D. Sebold, L. Blum, and N. H. Menzler, 'A Detailed Post Mortem Analysis of Solid Oxide Electrolyzer Cells after Long-Term Stack Operation', vol. 165, no. 5, pp. F357–F364, 2018, doi: 10.1149/2.0961805jes.

- [35] Q. Fu, J. Schefold, A. Brisse, and J. U. Nielsen, 'Durability Testing of a High-Temperature Steam Electrolyzer Stack at 700 °C', *Fuel Cells*, vol. 14, no. 3, pp. 395–402, 2014, doi: 10.1002/fuce.201300150.
- [36] G. Corre and A. Brisse, '9000 Hours Operation of a 25 Solid Oxide Cells Stack in Steam Electrolysis Mode', *ECS Trans.*, vol. 68, no. 1, pp. 3481–3490, Jun. 2015, doi: 10.1149/06801.3481ecst.
- [37] M. Lang, S. Raab, M. S. Lemcke, C. Bohn, and M. Pysik, 'Long Term Behavior of Solid Oxide Electrolyser (SOEC) Stacks', *ECS Trans.*, vol. 91, no. 1, pp. 2713–2725, 2019, doi: 10.1149/09101.2713ecst.
- [38] D. Papurello, A. Lanzini, S. Fiorilli, F. Smeacetto, R. Singh, and M. Santarelli, 'Sulfur poisoning in Ni-anode solid oxide fuel cells (SOFCs): Deactivation in single cells and a stack', *Chem. Eng. J.*, vol. 283, pp. 1224–1233, Jan. 2016, doi: 10.1016/j.cej.2015.08.091.
- [39] H. Madi, A. Lanzini, S. Diethelm, D. Papurello, J. Van herle, M. Lualdi, J. Gutzon Larsen and M. Santarelli, 'Solid oxide fuel cell anode degradation by the effect of siloxanes', *J. Power Sources*, vol. 279, pp. 460–471, Apr. 2015, doi: 10.1016/j.jpowsour.2015.01.053.
- [40] K. Chen and S. P. Jiang, 'Review—Materials Degradation of Solid Oxide Electrolysis Cells', *J. Electrochem. Soc.*, vol. 163, no. 11, pp. F3070–F3083, 2016, doi: 10.1149/2.0101611jes.
- [41] H. Yokokawa, H. Tu, B. Iwanschitz, and A. Mai, 'Fundamental mechanisms limiting solid oxide fuel cell durability', *J. Power Sources*, vol. 182, no. 2, pp. 400–412, Aug. 2008, doi: 10.1016/j.jpowsour.2008.02.016.
- [42] T. Shimonosono, H. Kishimoto, M. E. Brito, K. Yamaji, T. Horita, and H. Yokokawa, 'Phase transformation related electrical conductivity degradation of NiO doped YSZ', *Solid State Ion.*, vol. 225, pp. 69–72, Oct. 2012, doi: 10.1016/j.ssi.2012.05.023.
- [43] J. Laurencin, M. Hubert, D. F. Sanchez, S. Pylypko, M. Morales, A. Morata, B. Morel, D. Montinaro, F. Lefebvre-Joud and E. Siebert, 'Degradation mechanism of La<sub>0.6</sub>Sr<sub>0.4</sub>Co<sub>0.2</sub>Fe<sub>0.8</sub>O<sub>3-δ</sub>/Gd<sub>0.1</sub>Ce<sub>0.9</sub>O<sub>2-δ</sub> composite electrode operated under solid oxide electrolysis and fuel cell conditions', *Electrochimica Acta*, vol. 241, pp. 459–476, Jul. 2017, doi: 10.1016/j.electacta.2017.05.011.
- [44] D. The, S. Grieshammer, M. Schroeder, M. Martin, M. Al Daroukh, F. Tietz, J. Schefold and A. Brisse 'Microstructural comparison of solid oxide electrolyser cells operated for 6100 h and 9000 h', *J. Power Sources*, vol. 275, pp. 901–911, Feb. 2015, doi: 10.1016/j.jpowsour.2014.10.188.
- [45] T. Matsui, J.-Y. Kim, H. Muroyama, T. Abe, M. Miyao and K. Eguchi 'Anode microstructural change upon long-term operation for the cathode-supported tubular-type SOFC', *Solid State Ion.*, vol. 225, pp. 50–54, Oct. 2012, doi: 10.1016/j.ssi.2012.03.035.
- [46] A. V. Virkar, 'Mechanism of oxygen electrode delamination in solid oxide electrolyzer cells', *Int. J. Hydrog. Energy*, vol. 35, no. 18, pp. 9527–9543, Sep. 2010, doi: 10.1016/j.ijhydene.2010.06.058.
- [47] K. Chen and S. P. Jiang, 'Failure mechanism of (La,Sr)MnO<sub>3</sub> oxygen electrodes of solid oxide electrolysis cells', *Int. J. Hydrog. Energy*, vol. 36, no. 17, pp. 10541–10549, Aug. 2011, doi: 10.1016/j.ijhydene.2011.05.103.
- [48] D.-J. Liu, J. Almer, and T. Cruse, 'Characterization of Cr Poisoning in a Solid Oxide Fuel Cell Cathode Using a High Energy X-ray Microbeam', *J. Electrochem. Soc.*, vol. 157, no. 5, p. B744, 2010, doi: 10.1149/1.3358262.
- [49] Y. Tao, J. Shao, and S. Cheng, 'Electrochemically Scavenging the Silica Impurities at the Ni–YSZ Triple Phase Boundary of Solid Oxide Cells', *ACS Appl. Mater. Interfaces*, vol. 8, no. 27, pp. 17023–17027, Jul. 2016, doi: 10.1021/acsami.6b04723.
- [50] R. VAŠEN and D. Simwonis, 'Modelling of the agglomeration of Ni-particles in anodes of solid oxide fuel cells', p. 5.
- [51] M. Hubert, J. Laurencin, P. Cloetens, B. Morel, D. Montinaro, and F. Lefebvre-Joud, 'Impact of Nickel agglomeration on Solid Oxide Cell operated in fuel cell and electrolysis modes', *J. Power Sources*, vol. 397, pp. 240–251, Sep. 2018, doi: 10.1016/j.jpowsour.2018.06.097.

- [52] M. B. Mogensen *et al.*, 'Relation Between Ni Particle Shape Change and Ni Migration in Ni-YSZ Electrodes - a Hypothesis', *Fuel Cells*, vol. 17, no. 4, pp. 434–441, Aug. 2017, doi: 10.1002/face.201600222.
- [53] M. Trini, A. Hauch, S. De Angelis, X. Tong, P. V. Hendriksen, and M. Chen, 'Comparison of microstructural evolution of fuel electrodes in solid oxide fuel cells and electrolysis cells', *J. Power Sources*, vol. 450, p. 227599, Feb. 2020, doi: 10.1016/j.jpowsour.2019.227599.
- [54] F. Monaco, M. Hubert, J. Vulliet, J.P. Ouweltjes, D. Montinaro, P. Cloetens, P. Piccardo, F. Lefebvre-Joud and J. Laurencin, 'Degradation of Ni-YSZ Electrodes in Solid Oxide Cells: Impact of Polarization and Initial Microstructure on the Ni Evolution', *J. Electrochem. Soc.*, vol. 166, no. 15, pp. F1229–F1242, 2019, doi: 10.1149/2.1261915jes.
- [55] N. H. Menzler, D. Sebold, Y. J. Sohn, and S. Zischke, 'Post-test characterization of a solid oxide fuel cell after more than 10 years of stack testing', *J. Power Sources*, vol. 478, p. 228770, Dec. 2020, doi: 10.1016/j.jpowsour.2020.228770.
- [56] M. Chen, Y. Liu, J. J. Bentzen, W. Zhang, X. Sun, A. Hauch, Y. Tao, J. R. Bowen and P. V. Hendriksen, 'Microstructural Degradation of Ni/YSZ Electrodes in Solid Oxide Electrolysis Cells under High Current', *J. Electrochem. Soc.*, vol. 160, no. 8, pp. F883–F891, 2013, doi: 10.1149/2.098308jes.
- [57] A. Hauch, K. Brodersen, M. Chen, and M. B. Mogensen, 'Ni/YSZ electrodes structures optimized for increased electrolysis performance and durability', *Solid State Ion.*, vol. 293, pp. 27–36, Oct. 2016, doi: 10.1016/j.ssi.2016.06.003.
- [58] A. Sciazko, T. Shimura, Y. Komatsu, and N. Shikazono, 'Ni-GDC and Ni-YSZ electrodes operated in solid oxide electrolysis and fuel cell modes', *J. Therm. Sci. Technol.*, vol. 16, no. 1, pp. JTST0013–JTST0013, 2021, doi: 10.1299/jtst.2021jtst0013.
- [59] M. B. Mogensen, M. Chen, H. L. Frandsen, C. Graves, A. Hauch, P. V. Hendriksen, T. Jacobsen, S. H. Jensen, T. L. Skaftø and X. Sun, 'Ni migration in solid oxide cell electrodes: Review and revised hypothesis', *Fuel Cells*, p. face.202100072, Sep. 2021, doi: 10.1002/face.202100072.
- [60] M. B. Mogensen and G. Mogensen, 'On Degradation Mechanisms of Ni-YSZ Fuel Electrodes in Solid Oxide Cells', *ECS Trans.*, no. 112, p. 71, 2023.
- [61] Y. Lei, W. Epting, J. Masson, T. Cheng, H. Abernathy, G. Hackett and Y. Wen, 'Simulating Microstructure Evolution in Ni-YSZ Electrodes of Solid Oxide Cells Under Operating Conditions', in *TMS 2022 151st Annual Meeting & Exhibition Supplemental Proceedings*, The Minerals, Metals & Materials Society, Ed., in The Minerals, Metals & Materials Series. , Cham: Springer International Publishing, 2022, pp. 457–469. doi: 10.1007/978-3-030-92381-5\_42.
- [62] A. Nakajo, G. Rinaldi, P. Caliendo, G. Jeanmonod, L. Navratilova, M. Cantoni and J. Van herle, 'Evolution of the Morphology Near Triple-Phase Boundaries in Ni–Yttria Stabilized Zirconia Electrodes Upon Cathodic Polarization', *J. Electrochem. Energy Convers. Storage*, vol. 17, no. 4, p. 041004, Nov. 2020, doi: 10.1115/1.4046478.
- [63] D. C. Grahame, 'The Electrical Double Layer and the Theory of Electrocapillarity.', *Chem. Rev.*, vol. 41, no. 3, pp. 441–501, Dec. 1947, doi: 10.1021/cr60130a002.
- [64] T.-L. Cheng, Y. Lei, Y. Chen, Y. Fan, H. Abernathy, X. Song and Y.-H. Wen, 'Oxidation of nickel in solid oxide cells during electrochemical operation: Experimental evidence, theoretical analysis, and an alternative hypothesis on the nickel migration', *J. Power Sources*, vol. 569, p. 232991, Jun. 2023, doi: 10.1016/j.jpowsour.2023.232991.

## 2. Materials and methods

In this work, a coupled experimental and modeling approach including many tools has been used to study the cell degradations and especially the evolution of the cermet microstructure of the H<sub>2</sub> electrode upon operation. Indeed, as previously discussed in chapter 1, the degradation mechanism occurring in this electrode is still not understood. Nevertheless, this degradation phenomenon, which is responsible of a significant part of the cell performance losses, is liable to depend on many operating parameters such as the current density applied to the cell, the operating mode (electrolysis or fuel cell mode), and also the temperature. In order to investigate the effect of such parameters on the cell, a series of long-term tests has been performed in this work. The first part of this chapter aims to describe the test bench used for all the electrochemical experiments with the precise associated protocol. Then, in order to better understand the evolution of the microstructure and the corresponding degradation under operation, cell samples have been prepared for advanced post-test characterizations. Thus, the second part of this chapter is dedicated to the post-mortem techniques employed in this work. More specifically, the polished cross-sections are observed by Scanning Electron Microscopy (SEM) and the electrode microstructure reconstructed by Focused ion beam (FIB)-SEM tomography. In addition, a set of numerical tools already developed in the laboratory are used in this study to compute the microstructural properties from the 3D volumes of each sample. Finally, the data obtained from the long-term tests are introduced as input data in an electrochemical multi-scale model calibrated to reproduce the performance of the cells studied in this work. The last part is dedicated to the description of the model and its associated application.

### 2.1 Long-term tests

#### 2.1.1 Cell description

The studied CEA cell has a circular shape with an active area of 9.08 cm<sup>2</sup>. The cell is composed of a 280 μm-thick cermet substrate made of NiO and zirconia stabilized with 3 mol.% of yttria (NiO-3YSZ, reduced in Ni-3YSZ before operation). This substrate is manufactured by tape-casting and used as the cell mechanical support on which the following additional layers are screen-printed. Firstly, a 25 μm functional layer of NiO and zirconia stabilized with 8 mol.% yttria (NiO-8YSZ, reduced in Ni-8YSZ before operation) is deposited on top of the substrate. The Ni-to-YSZ weight ratios for the active layer and the support are respectively, 8YSZ/Ni/8YSZ = 54 wt% /46 wt% / and Ni/3YSZ = 44 wt%/56 wt%. Moreover, a very thin layer of Ni is deposited on the cermet surface in order to ensure the good electrical contact. The dense and 8 μm-thin electrolyte, which consists of 8YSZ, is co-sintered with both cermet layers. The oxygen

electrode deposited onto the electrolyte has a bilayer structure. The active part of the oxygen electrode is a 22  $\mu\text{m}$  thick porous layer constituted of a LSCF-CGO composite with  $\text{La}_{0.6}\text{Sr}_{0.4}\text{Co}_{0.2}\text{Fe}_{0.8}\text{O}_{3-\delta}$  (LSCF) perovskite and 20 mol.% Gadolinium Doped Ceria Oxide (GDC or CGO). The current collector is made of LSCF with a thickness of 20  $\mu\text{m}$ . A thin barrier diffusion layer of CGO (ca. 3  $\mu\text{m}$  thick) is also added between the electrolyte and the oxygen electrode to avoid the formation of secondary insulating phases.

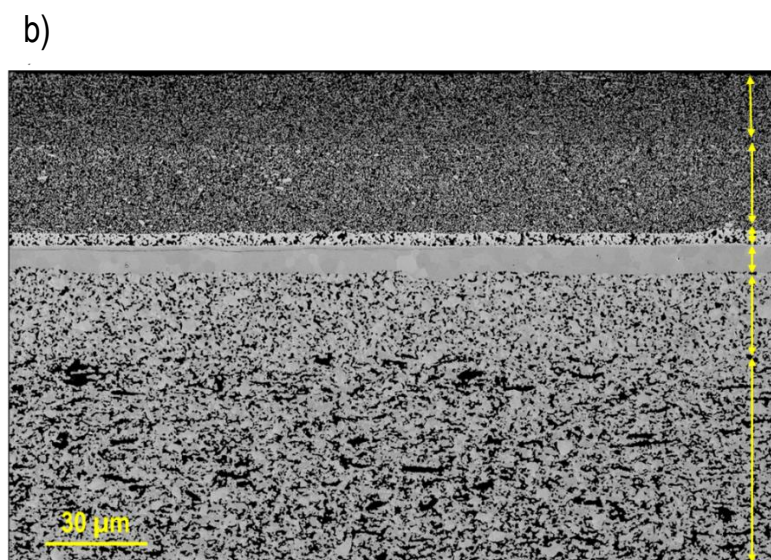
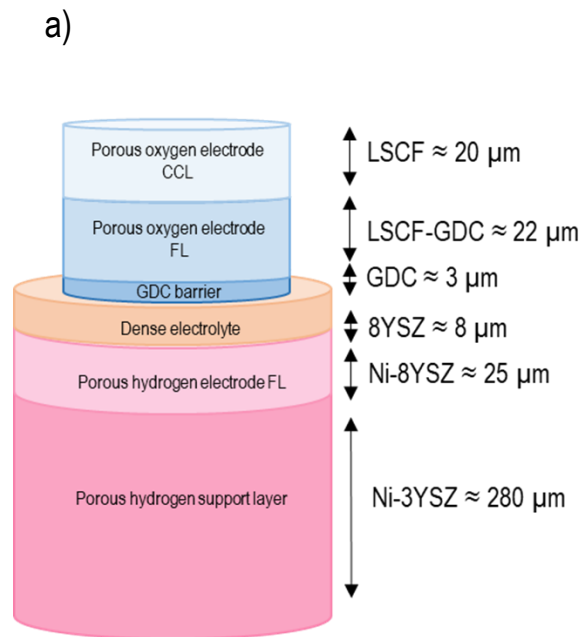


Figure 2-1: a) Schematic representation of the classical cell, b) SEM images in secondary electrons of the complete cell exhibiting all the layers.

### 2.1.2 Test bench

The durability tests carried out for the purpose of this thesis were conducted using the typical CEA cells described above. Those long-term experiments have been performed on a test bench developed for operation in fuel cell and electrolysis modes (Figure 2-2). The cell holder at the hydrogen side is made of Crofer 22 APU steel while an alumina gas diffuser is used at the oxygen side Figure 2-2. The cell temperature is measured with thermocouples located in the cell holder and in the gas outlet on H<sub>2</sub> side. For each electrode, the gases are introduced at the cell center for a radial co-flow configuration. Brooks SLA5850S mass flow controllers ensure the delivery of the gases (Air, N<sub>2</sub>, H<sub>2</sub> and steam produced from deionized water in a homemade evaporator kept at a temperature of 106-108°C and a pressure of around 200 mbar). Moreover, the precision of the steam mass flow meter after its calibration is +/- 0.09 NL/h (which is rather negligible compared to the inlet steam flow rate of 5.88 NL/h). Furthermore, in order to check the actual steam content sent to the cell, liquid water is weighed at the cell outlet after steam condensation. As a general matter, it can be noted that a reasonable agreement is obtained between the mass flow controller set point and the weight of water measured at the cell outlet (with an error of less than 10%). It is worth noting that to avoid any condensation in the gas lines of the test bench, all the pipes were kept at a temperature higher than 120°C. As depicted in Figure 2-2, a Schott G018-311 glass ceramic seal is deposited at the cell periphery to ensure the gas tightness of the hydrogen compartment. An H<sub>2</sub> mass-flow meter, located at the outlet, allows a continuous control of tightness and produced/consumed H<sub>2</sub> flow in SOEC/SOFC operation respectively. Nickel and gold grids are used for the current collection and gas distribution at the hydrogen and oxygen sides, respectively. A load of 600 g.cm<sup>-2</sup> is applied on the top of the set-up to minimize the contact resistances between the electrodes and the grids.

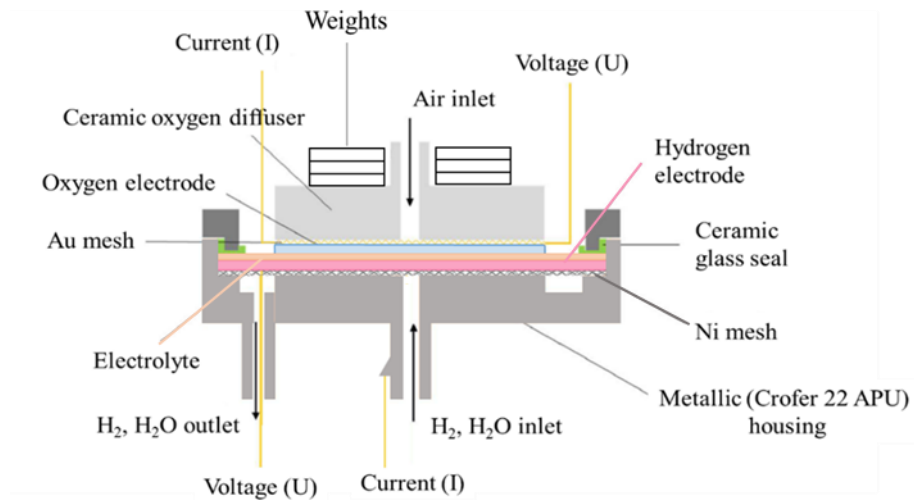


Figure 2-2: Schematic representation of the experimental set-up for the durability experiments.

### 2.1.3 Experimental setup, protocol for testing and data acquisition

All the durability tests performed in this work have been conducted following a precise protocol, which is described hereafter. Firstly, the cell was heated-up at  $1\text{ }^{\circ}\text{C}\cdot\text{min}^{-1}$  to avoid any thermo-mechanical damaging of the cell and sealing, and by feeding the oxygen and hydrogen compartments with air and nitrogen respectively. After a thermal treatment at a temperature higher than  $800^{\circ}\text{C}$  for the formation of the glass ceramic seal, the temperature was stabilized at  $800^{\circ}\text{C}$  for the cermet reduction of NiO into Ni carried out by introducing progressively hydrogen into nitrogen. After the complete cell reduction, the cells are let at OCV under dry  $\text{H}_2$  for 12h in order to check the tightness of the cells. After this, the temperature was lowered to a reference temperature of  $750^{\circ}\text{C}$ , which allows comparing the measured performances between them whatever the operating conditions of each long-term test. Initial electrochemical characterizations including polarization curves ( $i$ - $U$ ) and Electrochemical Impedance Spectroscopy (EIS) diagrams were recorded at the reference temperature and in the operating conditions of each experiment. All the electrochemical characterizations were conducted using a potentiostat/galvanostat (Autolab PGSTAT-302N) equipped with a Frequency Response Analyzer module (FRA) and a 20 A current booster. The  $i$ - $U$  curves have been measured in galvanostatic mode with a sweep rate of  $2.2\text{ mA}\cdot\text{s}^{-1}\cdot\text{cm}^{-2}$  (i.e.  $20\text{ mA}\cdot\text{s}^{-1}$ ) (which represents a good compromise between sufficiently low scanning rate (to fulfill the steady-state condition) and fast enough data acquisition) and a voltage limit equal to 0.7 V and 1.4 V in SOFC and SOEC modes, respectively. For the impedance measurements, the data were acquired in the frequency range of  $10^{-2}$  to  $10^4$  Hz by imposing a perturbation on the current with an amplitude of 100 mA. A typical impedance diagram recorded at OCV,  $750^{\circ}\text{C}$  and a fuel gas composition of 90 vol.%  $\text{H}_2\text{O}$  and 10 vol.%  $\text{H}_2$  is shown on Figure 2-3 a). The classical EIS presented here after is composed of three main contributions related to all the electrochemical reactions, chemical mechanisms, ionic transport and gas

diffusion and conversion in the cell. Equivalent Electric Circuit Model are usually used to fit the electrochemical impedance spectra using characteristic elements such as resistance and capacitance. However, it is worth noting that the contribution at high frequencies is distorted by an inductance related to the set-up wires. The classical Equivalent Electric Circuit Model (EECM) proposed in [1] [2], shown on Figure 2-3 and used in this work is composed of (i) an inductance (L) taking into account the contribution of the wires, (ii) a series resistance ( $R_s$ ) associated to the pure ohmic losses, (iii) three resistance-constant phase element groups (R-CPE) related to the high, medium and low frequencies arcs. In order to correct the artefact introduced by this inductive effect, the diagram has been fitted using this EEC model and the contribution associated to the inductance has been removed. Indeed, as depicted in Figure 2-3 a), the series resistance in the simulated spectrum is decreased compared to the initial diagram while the high frequency contribution is enlarged.

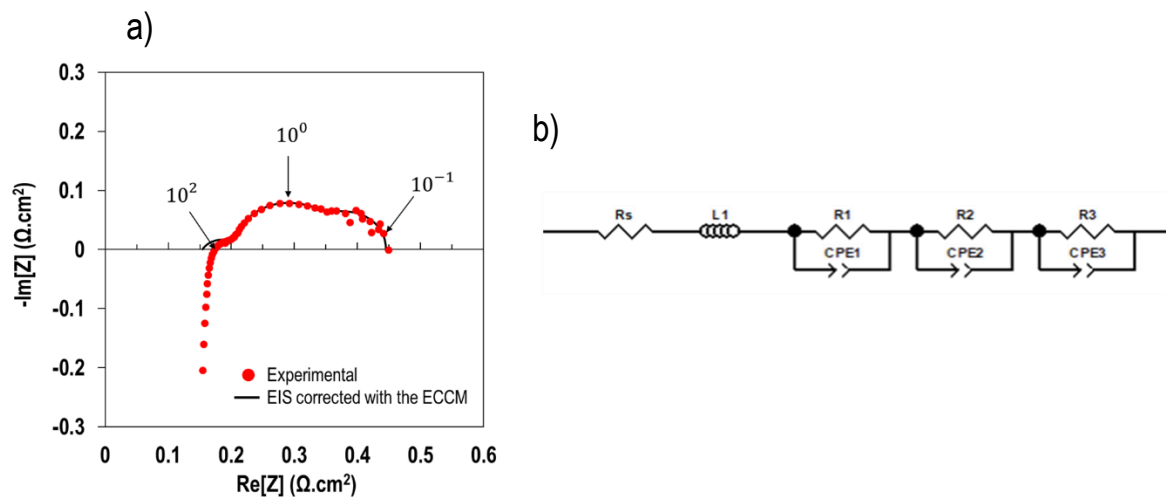


Figure 2-3: a) Experimental EIS and after its correction using the EECM (OCV at 750 °C,  $p_{H_2}/p_{H_2O} = 0.1/0.9$  and  $12 \text{ NmL.cm}^{-2}.\text{min}^{-1}$ ) and b) equivalent circuit model (EECM) used to analyze the EIS spectra.

In this thesis, a series of long-term tests was carried out to investigate the effect of different operating parameters on the cell performances and the consequent degradations. All the tests realized in this thesis are summarized in table 2-1.

**Table 2-1: Summary of the durability tests**

Parameters	Test 1	Test 2	Test 3	Test 4	Test 5	Test 6
Time (h)	2000	2000	1000	5000	2000	2000
Temperature (°C)	750	850	800	800	800	800
Mode	SOEC	SOEC	SOEC	SOEC	SOFC	SOEC
Current Density ( $A/cm^2$ )	-1	-1	-1	-1	+1	-1
$H_2+H_2O$ gas flow ( $NmL \text{ min}^{-1} \text{ cm}^{-2}$ )	12	12	12	12	12	12
Gas composition, $H_2/H_2O$ (vol.%)	10/90	10/90	10/90	10/90	90/10	10/90
Air gas flow ( $NmL \text{ min}^{-1} \text{ cm}^{-2}$ )	36	36	36	36	36	36

The effect of the temperature has been investigated with three tests (Tests 1,2 and 6) performed for 2000 h, in electrolysis mode at 750°C, 800°C and 850°C, in galvanostatic mode at -1 A.cm<sup>-2</sup> with a Steam Conversion of 64% and a gas composition of 90 vol.% H<sub>2</sub>O and 10 vol.% H<sub>2</sub>. It is worth noting that the steam conversion is calculated according to the following formula:  $100 \times \left( \frac{I \times 3600 \times V_m}{2 \times F \times flow} \right)$ . Where  $I$  is the current in A,  $V_m$  : 22.4 NI/mol,  $F$  is the faraday constant and the flow is equal to 90% of the total flow rate. Moreover, the effect of the ageing time has also been investigated with two other experiments in electrolysis mode (Tests 3 and 4) of 1000h and 5000h at 800°C in galvanostatic mode at -1 A.cm<sup>-2</sup> with a SC of 64% and a gas composition of 90 vol.% H<sub>2</sub>O and 10 vol.% H<sub>2</sub>. Furthermore, the difference between both fuel cell and electrolysis operating modes has been investigated with a supplementary long-term test (Test 5) conducted in fuel cell mode for 2000 h at 800°C and 1 A.cm<sup>-2</sup> with a fuel utilization of 64% and a gas composition of 10 vol.% H<sub>2</sub>O and 90 vol.% H<sub>2</sub>. The cell voltage was continuously monitored during the tests while intermediate EIS diagrams at Open Circuit Voltage (OCV) were acquired approximately each 500h. At the end, final characterizations have been measured at the reference condition (750°C) as well as in the conditions of each experiment. The cell was then cooled down at 1 °C.min<sup>-1</sup> to room temperature by sweeping the Ni-YSZ electrode with a sufficient quantity of hydrogen to maintain the Ni in its reduced state. Additionally, a cell was reduced in the same set-up and used as a reference for all the post-test characterizations.

## 2.2 Post-test characterization

### 2.2.1 SEM observations

After ageing, the cells are cut and embedded in an epoxy resin (Epofix®) under vacuum to fill the open porosity. Then, the cross-sections were polished step by step starting with a paper of 800 µm until a final stage performed with a silica spray of 0.03 µm. A thin carbon coating of around 2 nm was deposited on the polished cross-sections to avoid charging artefacts during the observations. Polished cross-sections of the reference and the aged cells were observed using a Field Emission Gun - Scanning Electron Microscope (FEG-SEM, ZEISS Merlin). The SEM images were obtained in Back-Scattered Electrons (BSE) mode to reveal a chemical contrast between the different phases present in the cell (associated to the atomic number of the atoms. Indeed, the heavier atoms implies a higher number of back-scattered electrons resulting in the observation of by a brighter region on the sample), with an acceleration voltage of 2 kV and a working distance of 5 mm. It is worth noting that the accelerating voltage used in this work allows to better distinguish YSZ from Ni as discussed in [3]. The SEM images were also obtained in

secondary electrons mode (associated to the rate of secondary electrons. This detector allows getting the topography of the sample) with a voltage of 10kV and a working distance of around 10 mm.

### 2.2.2 EDX analysis

The EDX (Energy-dispersive X-ray spectroscopy) technic has also been applied on the studied samples. Indeed, cartographies of principal elements composing the cermet have been acquired in order to get their distribution over the hydrogen electrode. EDX detection is based on photons emitted from the interaction between the atoms present in the sample and the incident electrons. Therefore, these photons are analysed with the EDX detector and are characteristic of the atoms they come from in order to give spectra of the different pics detected. Therefore, each element has a unique set of peaks on its electromagnetic spectrum.

### 2.2.3 FIB-SEM reconstructions

Representative volumes of the aged samples are obtained thanks to a destructive method for 3D imaging using a Focused Ion Beam coupled with a Scanning Electron Microscope (FIB-SEM, Zeiss CB550). In this method, the FIB is used to cut the material slice by slice, then SEM images are recorded for each slice allowing a good spatial resolution with an in-lens secondary electron detector [4]. The stack of images is then gathered onto a well representative volume of the cell. SEM images were acquired using Energy Selective Back-Scattered (ESB) and standard Secondary Electron (SE) detectors, with a voltage of 1.5 kV and a pixel size of 10 nm. FIB milling between two successive slices was also fixed at 10 nm in such a way that the voxel size in the reconstruction is  $10^3 \text{ nm}^3$ . In each direction, the acquired volumes are a few tenths of a micron. After acquisition and image processing to align and correct artifacts, the 3D image segmentation has to be carried out. The segmentation consists in labelling each voxel to a phase (pore, YSZ or Ni). This process requires identifying the thresholds in the grey level histogram of the image between the peaks related to each phase. For this purpose, an automatic code is used to find the best threshold value [5] to separate the 3 phases that composed the hydrogen electrode (the porosity, the Ni and the YSZ). The segmentation was done in this work by machine-learning using Ilastik software [6][7].

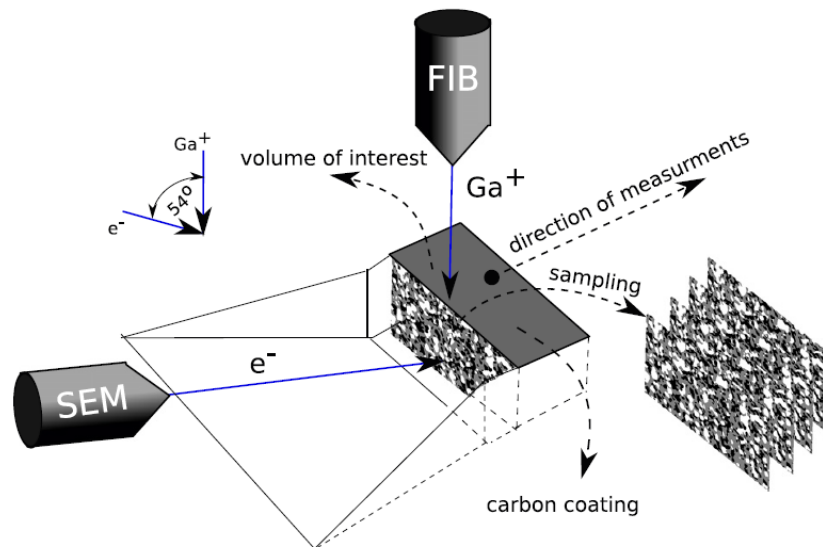


Figure 2-4: Schematic representation of the FIB-SEM technic [3].

#### 2.2.4 Codes for the microstructure

A Representative Volume Element (RVE) of the regions of interest containing the functional layer of the hydrogen electrode and a part of the dense electrolyte is selected in order to quantify accurately the microstructural properties. A set of numerical tools thoroughly detailed in [8] [9] is used to compute all the microstructural properties required for the simulations and allows studying the evolution of the microstructure under operation. For the hydrogen electrode, the main microstructural properties are the density of active TPBI ( $\xi_{\text{TPBIs}}$ ) in  $\mu\text{m}^{-2}$ , the volume fraction of each phase ( $\varepsilon$ ), the mean phase diameter in  $\mu\text{m}$ , the specific interfacial surface areas between two phases  $i$  and  $j$  ( $SP^{ij}$ ) in  $\mu\text{m}^{-1}$ , the 'apparent' tortuosity factors ( $\tau$ ) (which is related to the ratio of the effective length and the shortest length and the constrictivity parameter of the phase [10]).

### 2.3 Multi-scale electrochemical model

A dynamic physic-based model has been developed to unravel the relationships between the overall solid oxide cell response and the reaction mechanisms taking place in the electrodes. This tool combines modules at three different length-scales: electrode microstructures, two micro-scale electrochemical models for each electrodes and a macro-scale model at the complete cell/SRU level. More specifically, it links the microscale electrode models to the macroscopic description including the cell geometry as well as the properties of the microstructure for both electrodes and the radial co-flow configuration of the test bench (cf. Figure 2-2). On the one hand, at the micro-scale, two electrochemical models allow to describe the microscopic processes taking place in the active functional layer of both hydrogen and oxygen

electrodes. These models, which take into account the electrode microstructure via the properties extracted from the 3D reconstructions, give an understanding of the reaction mechanisms occurring in the electrodes. They are able to simulate the stationary electrode response (i-U curves) under both anodic and cathodic polarizations [11] and the dynamic electrode response (EIS diagrams and voltammograms) [12]. In this work, these micro-scale models implemented in COMSOL Multiphysics® are used to calculate the electrode polarization or activation overpotentials along the cell length thanks to an elementary description of the reaction pathways. The elementary model for the oxygen electrode active layer made of LSCF-CGO is extensively detailed in [13] and is validated in both SOEC and SOFC modes. The thorough description of the elementary kinetic model for the Ni-YSZ hydrogen electrode can be found in [14]. The model is based on a hydrogen spillover mechanism taking into account the gas interactions with both Ni and YSZ surfaces.

a)

CR1	Steam adsorption on the Ni surface	$H_2O(gas) + s_{Ni} \xrightleftharpoons[k_{H_2ONi}^{DES}]{k_{H_2ONi}^{ADS}} H_2ONi$
CR2	Steam adsorption on the YSZ surface	$H_2O(gas) + s_{YSZ} \xrightleftharpoons[k_{H_2OYSZ}^{DES}]{k_{H_2OYSZ}^{ADS}} H_2O_{YSZ}$
CR3	H <sub>2</sub> O dissociation on YSZ surface	$H_2O_{YSZ} + O_{YSZ}^{2-} \xrightleftharpoons[k_{H_2OYSZ}^{DISS-}]{k_{H_2OYSZ}^{DISS+}} 2OH_{YSZ}^-$
CR4	Hydrogen desorption from the Ni surface	$2H_{Ni} \xrightleftharpoons[k_{H_2Ni}^{ADS}]{k_{H_2Ni}^{DES}} H_2(gas) + 2s_{Ni}$
ER1	First charge transfer reaction	$H_2ONi + s_{YSZ} + 1e_{Ni}^- \xrightleftharpoons[k_1^{ox}]{k_1^{red}} OH_{YSZ}^- + H_{Ni}$
ER2	Second charge transfer reaction	$OH_{YSZ}^- + s_{Ni} + 1e_{Ni}^- \xrightleftharpoons[k_2^{ox}]{k_2^{red}} O_{YSZ}^{2-} + H_{Ni}$
CR5	Oxygen incorporation in the YSZ lattice	$O_{YSZ}^{2-} + V_O^{**}(YSZ) \xrightleftharpoons[k_{O_{YSZ}}^{EXC}]{k_{O_{YSZ}}^{INC}} O_O^{\bullet}(YSZ) + s_{YSZ}$

b)

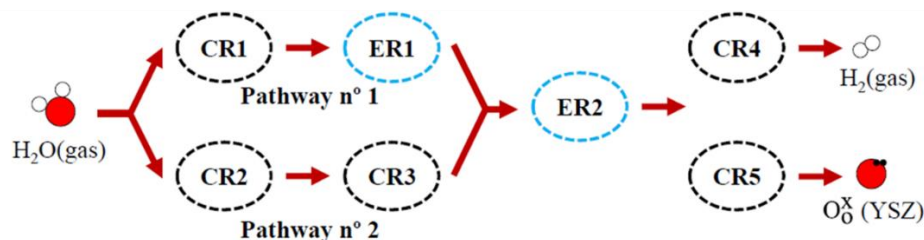


Figure 2-5: a) Reactions for the hydrogen electrode (expressed in electrolysis mode with the abbreviation CR and ER referring to the chemical and electrochemical reactions, respectively)  
 b) Schematic representation of the two parallel pathways for the electrode reaction (given in electrolysis mode) [14].

Indeed, assuming an electrolysis operation for instance, the first proposed pathway (Figure 2-5) consists in the steam adsorption on the Ni surface where water molecules are electrochemically reduced at the TPBI, forming  $H_{Ni}$  and  $OH_{YSZ}^-$  on the Ni and YSZ surface respectively. The  $OH_{YSZ}^-$  are then reduced at TPBIs, leading to the production of a second hydrogen ad-atom on Ni ( $H_{Ni}$ ) and an oxygen ion  $O_{YSZ}^{2-}$  on the YSZ surface. Finally, the  $H_{Ni}$  species are associated into a  $H_2$  molecule before being desorbed in the gas phase while the oxygen ions  $O_{YSZ}^{2-}$  are incorporated into the YSZ lattice [14] [15]. For the second path (Figure 2-5),  $H_2O$  can be adsorbed on the YSZ surface and reacts with the oxygen ions available at the YSZ surface where it is dissociated into hydroxyl ions. Then the hydroxyl ions are also reduced at TPBIs as described for the first path on Ni. It has been shown that the first pathway (steam adsorption on Ni surface) is preferentially activated under electrolysis mode while the water desorption from YSZ (second pathway) is predominant in fuel cell mode [14]. Moreover, it is worth noting that this model is able to predict accurately the dissymmetry of the  $H_2$  electrode polarization in SOFC and SOEC modes. On the other hand, the macro-scale model aims to reproduce the global response of a complete SRU considering a two-dimensional approach [16] [17] [18]. The model couples local fluidic and electrochemical steps, which allow computing the distribution of molar fractions along the gas channel and within the porous electrodes as well as the electrode overpotentials, the ohmic losses together with the local current density in the cell [18]. At the complete cell level (model implemented in MATLAB® or COMSOL Multiphysics®), the active layers are restricted to the electrode/electrolyte interface and the partial pressures calculated at the macro-scale are used as boundary conditions at the top of the active layer for the electrode models. To make the connection between both micro-scale and macro-scale models, the partial pressure exponents (m,n,p) and the activation energy ( $E_{act}$ ) defining the exchange current densities as described in equations 2-1 and 2-2, and determined with the micro-scale models are used in the complete cell/SRU model to calculate the “apparent” exchange current density for each electrode,  $i_0^{H_2}$  and  $i_0^{O_2}$ .

$$i_0^{H_2} = A \times (p_{H_2})^m \times (p_{H_2O})^n \times e^{\left(\frac{E_a^{H_2 electrode}}{RT}\right)} \quad 2-1$$

$$i_0^{O_2} = B \times (p_{O_2})^p \times e^{\left(\frac{E_a^{O_2 electrode}}{RT}\right)} \quad 2-2$$

Then, the activation overpotentials in the complete cell/SRU model are expressed using the phenomenological Butler-Volmer expression as follows [16]:

$$|\eta_{act}^{O_2 electrode}| + |\eta_{act}^{H_2 electrode}| = \frac{RT}{F} \sinh^{-1} \left\{ \frac{|i|}{2i_0^{O_2}} \right\} + \frac{RT}{F} \sinh^{-1} \left\{ \frac{|i|}{2i_0^{H_2}} \right\} \quad 2-3$$

In this approach, the local activation overpotentials at the cell/SRU level are equal to the electrode overpotentials calculated in the active layer with the micro-scale models. The link between the micro-scale and macro-scale model described above is well illustrated by the flowchart reported in Figure 2-6.

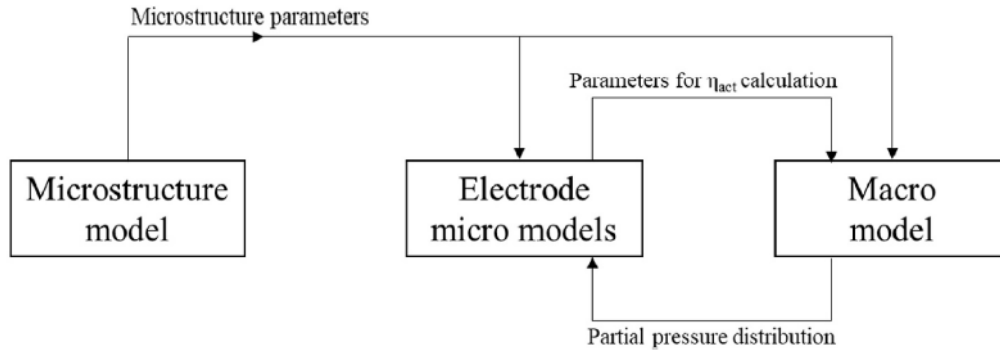


Figure 2-6: General flowchart of the multi-scale model as reported in [10].

The model has been calibrated and validated to reproduce the performances of the classical cells used in this work. For this purpose, the validation of the micro-scale electrode models has been done using polarization curves and electrochemical impedance spectra measured on a symmetrical cell in a specific three-electrode set-up [11] [13] [14]. It is worth noting that the calibration and the validation have been done in collaboration with Eduardo Da Rosa Silva [18] [11] and Giuseppe Sassone [12] for the cells tested in this work. For the stationary part, the model has been validated on various global and local *i*-*U* curves [11]. Figure 2-7 presents the results of the calibration of the *i*-*U* curves in a) SOEC and b) SOFC for different temperatures (700°C, 800°C and 850°C) and a flux of 12 NmL.min<sup>-1</sup>.cm<sup>-2</sup>. Moreover, the polarization curves of the complete cell have been measured in SOEC (p<sub>H<sub>2</sub></sub>/p<sub>H<sub>2</sub>O</sub> = 10/90) and SOFC (p<sub>H<sub>2</sub></sub>/p<sub>H<sub>2</sub>O</sub> = 100/0).

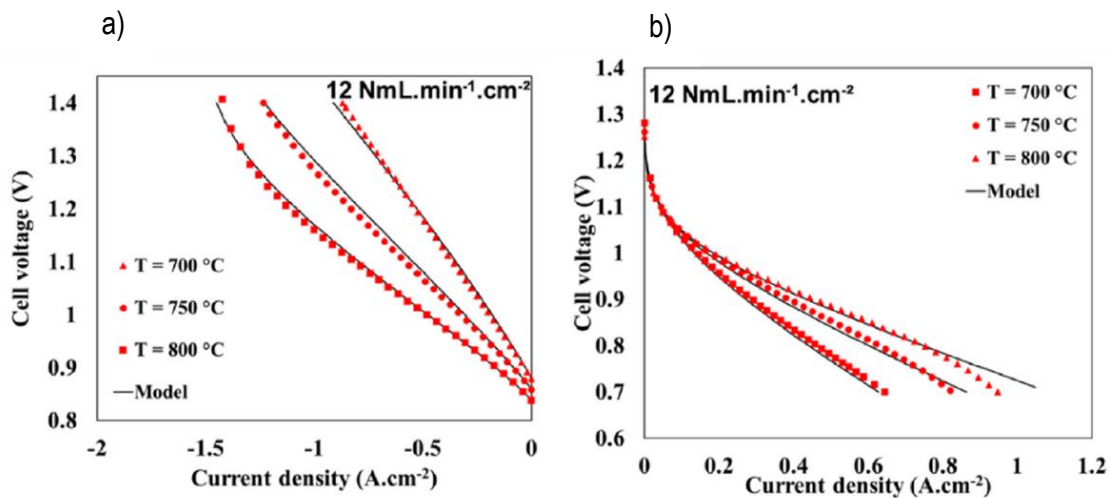


Figure 2-7: Polarization curves in a) SOEC p<sub>H<sub>2</sub></sub>/p<sub>H<sub>2</sub>O</sub> = 10/90 and b) SOFC p<sub>H<sub>2</sub></sub>/p<sub>H<sub>2</sub>O</sub> = 100/0 modes for a flux of 12 NmL.min<sup>-1</sup>.cm<sup>-2</sup> at 750°C [11]. Comparison between simulation and experimental data.

For the dynamic part, the model was validated by comparing the simulated impedance spectra and the experimental ones recorded for different gas composition at OCV [12] after correction by the EECM. The Figure 2-8 presents the results of the comparison of the EIS spectra in the Nyquist and Bode plots in SOEC mode  $p_{H_2}/p_{H_2O} = 10/90$  at OCV,  $750^\circ\text{C}$ , and a total inlet flow rate of  $12 \text{ NmL}\cdot\text{min}^{-1}\cdot\text{cm}^{-2}$  for validation of the electrochemical model. As explained in [12], a good agreement is found between the experimental and simulated spectra in the Nyquist plot in Figure 2-8 a) whereas the intensity in the imaginary part of the intermediate frequency arc of Bode plot b) is higher than the experimental one. It can be noted that the mismatch at intermediate frequencies (from  $10^{-1} \text{ Hz}$  to  $10^3 \text{ Hz}$ ) between the experimental and the simulated curves should come from the uncertainties on the microstructural properties for the Ni-YSZ support and especially the pore radius as discussed in [12] and shown in Figure 2-8 c) and d). Indeed, by changing this parameter it is possible to see an improvement of the mid-frequency contribution.

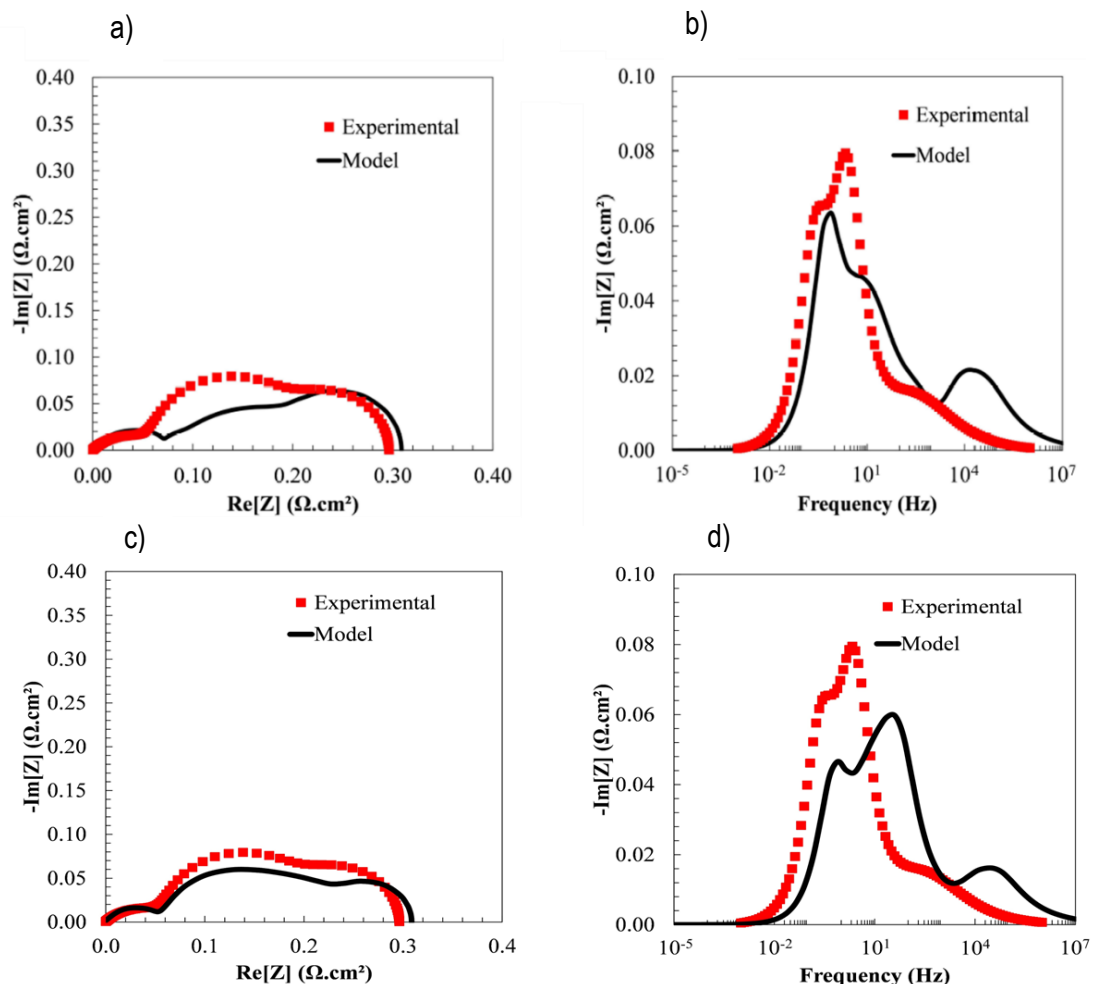


Figure 2-8: a) Nyquist plot and b) Bode plot of the EIS at OCV ( $750^\circ\text{C}$ ,  $p_{H_2}/p_{H_2O} = 10/90$ , total inlet flow rate= $12 \text{ NmL}\cdot\text{min}^{-1}\cdot\text{cm}^{-2}$ ). The ohmic losses have been removed from the impedance diagrams [12]. Comparison of the simulated and experimental EIS spectra after correction with the EECM, at OCV,  $750^\circ\text{C}$ ,  $p_{H_2}/p_{H_2O} = 0.1/0.9$  and  $12 \text{ NmL}\cdot\text{cm}^{-2}\cdot\text{min}^{-1}$  c) in Nyquist plot, d) in Bode plot and after modification of the microstructural properties (pore radius)

Thanks to the simulations and the multi-scale model, the three contributions in the impedance spectra can be identified unambiguously [12]. It has been found that the low frequency arc is mainly related to the gas conversion and diffusion in the cermet support. The contribution at medium frequencies is associated to the electrochemical and transport processes in the active layer of the oxygen electrode. The contribution at high frequencies is mainly related to the processes in the hydrogen electrode [12].

## 2.4 Conclusion

The coupled experimental and modeling approach is a powerful tool to understand the complex reactions and degradations mechanisms that occur in SOCs. In order to study the cell degradations and especially the cermet microstructural evolution in operation, a series of durability tests has been performed in this work on a test bench designed to operate in both electrolysis and fuel cell modes. The post-test characterizations including SEM imaging and FIB-SEM 3D reconstructions allow getting the microstructural properties and their evolution in order to understand the effect of the ageing in different operating conditions and its impact on the cell performances. The electrochemical data together with the post-test characterizations are then supplied to the developed multi-scale model calibrated and validated for the specific cells used in this work. Indeed, this multi-scale model is composed of a combination of three length-scales including (i) the electrode microstructure, (ii) an elementary kinetic model for the description of the electrodes functional layer, which are linked to (iii) a complete cell model for the SRU description. The electrochemical model has been used to assess the local electrode overpotentials from the H<sub>2</sub> electrode/electrolyte interface through the H<sub>2</sub> electrode thickness and the associated gradient of the Ni/YSZ contact angle in the conditions of the dedicated experiments (750°C, +/- 1A.cm<sup>-2</sup>, 90/10 vol.% H<sub>2</sub>O and 10/90 vol.% H<sub>2</sub> in SOEC and SOFC modes respectively). This last quantity is considered as the driving force for the Ni migration in the mechanism studied in this work.

## Bibliography of chapter 2

- [1] B. Liu, H. Muroyama, T. Matsui, K. Tomida, T. Kabata, and K. Eguchi, 'Analysis of Impedance Spectra for Segmented-in-Series Tubular Solid Oxide Fuel Cells', *J. Electrochem. Soc.*, vol. 157, no. 12, p. B1858, 2010, doi: 10.1149/1.3494214.
- [2] A. Nechache, A. Mansuy, M. Petitjean, J. Mougín, F. Mauvy, B. A. Boukamp, M. Cassir and A. Ringuedé, 'Diagnosis of a cathode-supported solid oxide electrolysis cell by electrochemical impedance spectroscopy', *Electrochimica Acta*, vol. 210, pp. 596–605, Aug. 2016, doi: 10.1016/j.electacta.2016.05.014.
- [3] K. Thydén, Y. L. Liu, and J. B. Bilde-Sørensen, 'Microstructural characterization of SOFC Ni-YSZ anode composites by low-voltage scanning electron microscopy', *Solid State Ion.*, vol. 178, no. 2008, pp. 1984–1989, 2007.
- [4] G. Brus, K. Miyawaki, H. Iwai, M. Saito, and H. Yoshida, 'Tortuosity of an SOFC anode estimated from saturation currents and a mass transport model in comparison with a real micro-structure', *Solid State Ion.*, vol. 265, pp. 13–21, 2014.
- [5] N. Otsu, 'A Threshold Selection Method from Gray-Level Histograms', vol. IEEE transaction system, pp. 62–66, 1979.
- [6] S. Berg, D. Kutra, T. Kroeger, C. N. Straehle; B. X. Kausler, C. Haubold, M. Schiegg, J. Ales, T. Beier, M. Rudy, K. Eren, J. Cervantes. B. Xu, F. Beuttenmueller, A. Wolny, C. Zhang, U. Koethe, F. A. Hamprecht and A. Kreshuk, 'ilastik: interactive machine learning for (bio)image analysis', *Nat. Methods*, vol. 16, no. 12, pp. 1226–1232, Dec. 2019, doi: 10.1038/s41592-019-0582-9.
- [7] C. Sommer, C. Straehle, U. Köthe, and F. A. Hamprecht, 'ilastik: Interactive learning and segmentation toolkit', in *2011 IEEE International Symposium on Biomedical Imaging: From Nano to Macro*, Mar. 2011, pp. 230–233. doi: 10.1109/ISBI.2011.5872394.
- [8] H. Moussaoui *et al.*, 'Stochastic geometrical modeling of solid oxide cells electrodes validated on 3D reconstructions', *Comput. Mater. Sci.*, vol. 143, pp. 262–276, Feb. 2018, doi: 10.1016/j.commatsci.2017.11.015.
- [9] F. Usseglio-Viretta, J. Laurencin, G. Delette, J. Villanova, P. Cloetens, and D. Leguillon, 'Quantitative microstructure characterization of a Ni-YSZ bi-layer coupled with simulated electrode polarisation', *J. Power Sources*, vol. 256, pp. 394–403, Jun. 2014, doi: 10.1016/j.jpowsour.2014.01.094.
- [10] A. Godula-Jopek, *Hydrogen Production: by Electrolysis*. John Wiley & Sons, 2015.
- [11] E. Da Rosa Silva, G. Sassone, M. Prioux, M. Hubert, B. Morel, and J. Laurencin, 'A multiscale model validated on local current measurements for understanding the solid oxide cells performances', *J. Power Sources*, vol. 556, p. 232499, Feb. 2023, doi: 10.1016/j.jpowsour.2022.232499.
- [12] G. Sassone *et al.*, 'Multiscale Modelling of Solid Oxide Cells Validated on Electrochemical Impedance Spectra and Polarization Curves', *ECS Trans.*, vol. 111, no. 6, pp. 649–661, May 2023, doi: 10.1149/11106.0649ecst.
- [13] E. Effori *et al.*, 'An Elementary Kinetic Model for the LSCF and LSCF-CGO Electrodes of Solid Oxide Cells: Impact of Operating Conditions and Degradation on the Electrode Response', *J. Electrochem. Soc.*, vol. 168, no. 4, p. 044520, Apr. 2021, doi: 10.1149/1945-7111/abf40a.
- [14] F. Monaco *et al.*, 'Electrode kinetics of porous Ni-3YSZ cermet operated in fuel cell and electrolysis modes for solid oxide cell application', *Electrochimica Acta*, vol. 389, p. 138765, Sep. 2021, doi: 10.1016/j.electacta.2021.138765.
- [15] D. G. Goodwin, H. Zhu, A. M. Colclasure, and R. J. Kee, 'Modeling Electrochemical Oxidation of Hydrogen on Ni-YSZ Pattern Anodes', *J. Electrochem. Soc.*, vol. 156, no. 9, p. B1004, 2009, doi: 10.1149/1.3148331.
- [16] J. Laurencin, 'Modelling of solid oxide steam electrolyser: Impact of the operating conditions on hydrogen production', *J. Power Sources*, p. 14, 2011.

- [17] L. Bernadet, J. Laurencin, G. Roux, D. Montinaro, F. Mauvy, and M. Reytier, 'Effects of Pressure on High Temperature Steam and Carbon Dioxide Co-electrolysis', *Electrochimica Acta*, vol. 253, pp. 114–127, Nov. 2017, doi: 10.1016/j.electacta.2017.09.037.
- [18] E. Da Rosa Silva, M. Hubert, B. Morel, H. Moussaoui, J. Debayle, and J. Laurencin, 'A Dynamic Multi-Scale Model for Solid Oxide Cells Validated on Local Current Measurements: Impact of Global Cell Operation on the Electrodes Reaction Mechanisms', *ECS Trans.*, vol. 103, no. 1, pp. 893–907, Jul. 2021, doi: 10.1149/10301.0893ecst.

### 3. Experimental evaluation of degradation tests

This third chapter is dedicated to the durability experiments and the post-test microstructural characterization carried out in this work. As presented in chapter one, SOCs are submitted under operation to many degradation phenomena arising in the electrodes and in the electrolyte, which are dependent on the operating conditions (the operating temperature, the ageing time, the functioning mode, etc.). In order to investigate the real impact of these parameters on the degradation, a series of long-term tests has been conducted in collaboration with G. Sassone, a PhD student in the laboratory. From these tests performed in galvanostatic mode, the durability curves  $U(t)$  as well as the initial, intermediate and final electrochemical characterizations (EIS diagrams and  $i$ - $U$  curves) have been obtained. Moreover, to better understand the phenomena underlying the degradation, post-test characterizations have been performed on all the tested cells in order to study the Ni evolution under operation. The post-mortem analysis includes 2D characterization with SEM images as well as EDX analysis and 3D FIB-SEM reconstructions. More specifically, representative volumes, which have been reconstructed from a reference and the aged cells, have been used to compute the microstructural properties of the electrode. Therefore, the first part of this chapter is dedicated to the results of the electrochemical characterizations acquired for each tested cell. The first section presents the initial performances whereas the second one details the durability curves as well as the initial and final EIS diagrams recorded as a function of the temperature, the ageing time and the operating mode. The second part presents the post-mortem results obtained on each sample and compared to a reference cell. The first section of this part shows the SEM and EDX analysis whereas the FIB-SEM 3D reconstructions are gathered in the second section with the associated microstructural properties.

#### 3.1 Initial cell performances

The initial performances of all the tested cells have been checked in the same SOEC conditions (750°C, 90 vol.% H<sub>2</sub>O and 10 vol.% H<sub>2</sub> i.e.  $p_{H_2}/p_{H_2O}=10/90$ , total flow of 12 Nml.min<sup>-1</sup>.cm<sup>-2</sup>) to ensure a similar starting point between all the durability experiments. In this frame, the initial  $i$ - $U$  curves have been plotted in Figure 3-1 and exhibit a similar behavior. They exhibit good performances at the thermoneutral voltage (TNV=1285 mV at 750°C) with a current density reaching values around -1 A.cm<sup>-2</sup> and a steam conversion of about 64%. The tightness of each cell has been checked by the value of the OCV under dry H<sub>2</sub>. For the bench used in this work, it is generally admitted that the standard OCV values that indicate a good tightness of the test is around 1200 mV at 800°C, higher than 1170 mV in average. The OCV values

obtained in these conditions are reported in table 3-1. They show that  $U \geq 1170$  mV (except for cell 5, aged in SOFC, however the study of the i-U curve has revealed a rather similar initial behavior) with a standard deviation of  $\pm 49$  mV. Therefore, it can be concluded that the gas tightness for the experiments is rather good and repeatable. The current density values at TNV have also been listed in table 3-1. They present a rather good dispersion of  $\pm 0.05$  A.cm<sup>-2</sup>, considering the standard scattering related to cell manufacturing. Indeed, the manufacturer has reported a standard deviation of  $\pm 0.054$  A.cm<sup>-2</sup>, for 12 cells tested in the same conditions.

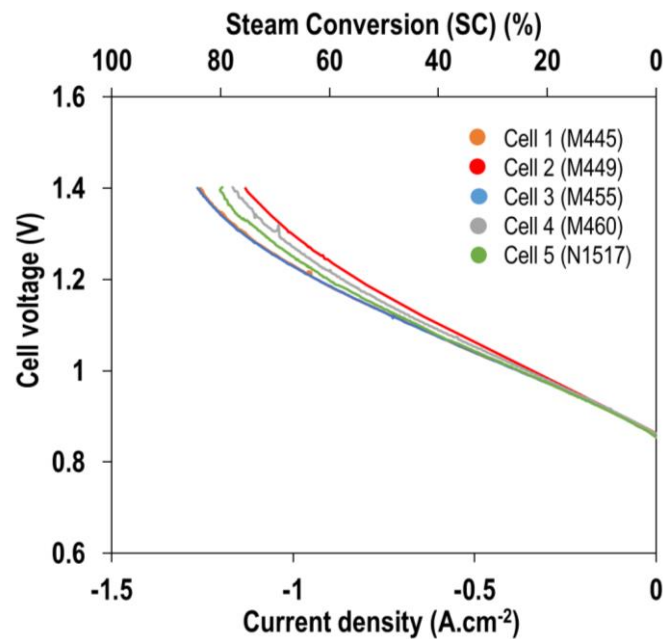


Figure 3-1: Initial i-U curves of the tested cells at the reference SOEC conditions (750°C,  $p_{H_2}/p_{H_2O}=10/90$  and 12 Nml.cm<sup>-2</sup>.min<sup>-1</sup>). The i-U curve of cell 6 is missing because of an experimental issue.

**Table 3-1 : Values of OCV under dry H<sub>2</sub> at 800°C and current density at TNV for the tested cells**

	OCV (mV)	i (A.cm <sup>-2</sup> ) at TNV
Cell1	1264	-1.06
Cell2	1236	-0.93
Cell3	1241	-1.06
Cell4	1271	-0.98
Cell5	1135	-1.01
Cell6	1245	-

In addition, the initial EIS spectra recorded in the same reference conditions at OCV have been plotted on Figure 3-2. The diagrams have been corrected from the inductance with the equivalent electric circuit model (EECM) already presented in the chapter 2 and show some scattering of the series resistance  $R_s$  and polarization resistance  $R_p$ , whose the average values are given in table 3-2.

These dispersions have been analyzed by calculating the standard deviation of the  $R_s$  and  $R_p$  values, which are respectively  $0.013 \Omega \cdot \text{cm}^2$  and  $0.02 \Omega \cdot \text{cm}^2$ , indicating a satisfying homogeneity in accordance with the cell manufacturing. Then, it can be pointed out that the cells present very similar performances at the beginning of the durability experiments. This good reproducibility between cells suggests that the initial electrode microstructures of the tested cells are well comparable.

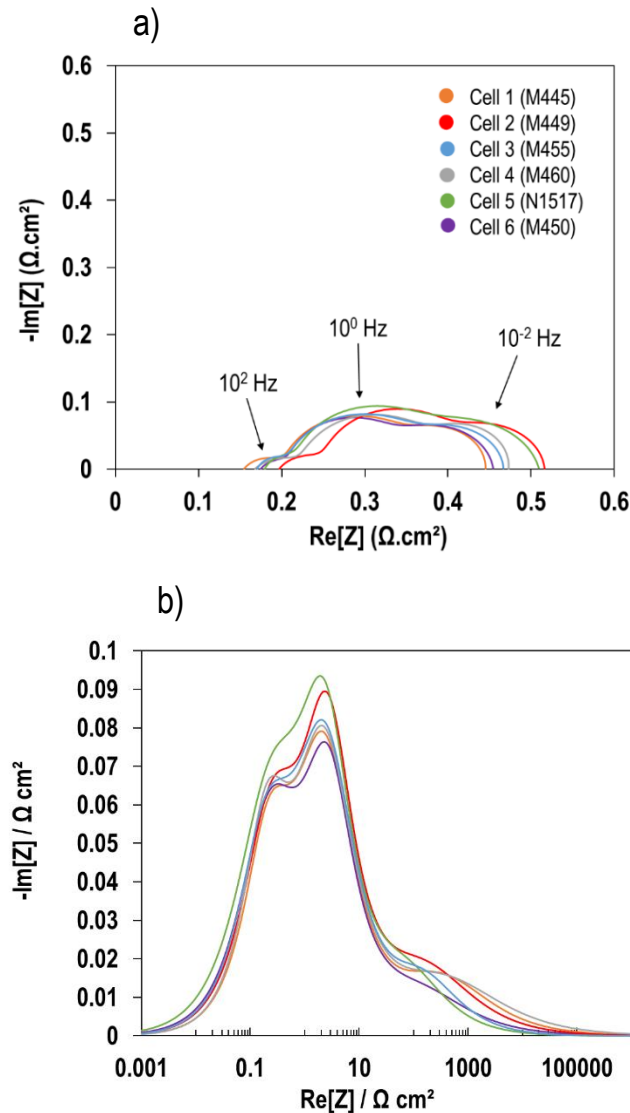


Figure 3-2: Initial EIS diagrams at OCV, in a) the Nyquist plot and b) the Bode plot for all the tested cells at  $750^\circ\text{C}$ ,  $\text{pH}_2/\text{pH}_2\text{O}=10/90$  and  $12 \text{ Nml} \cdot \text{cm}^{-2} \cdot \text{min}^{-1}$ .

**Table 3-2 : Standard deviation and average values of the series and polarization resistances ( $R_s$  and  $R_p$ )**

	Standard deviation	Average
$R_s$ ( $\Omega \cdot \text{cm}^2$ )	+/-0.01	0.18
$R_p$ ( $\Omega \cdot \text{cm}^2$ )	+/-0.02	0.31

## 3.2 Study of the degradations under different operating conditions

### 3.2.1 Effect of the operating temperature

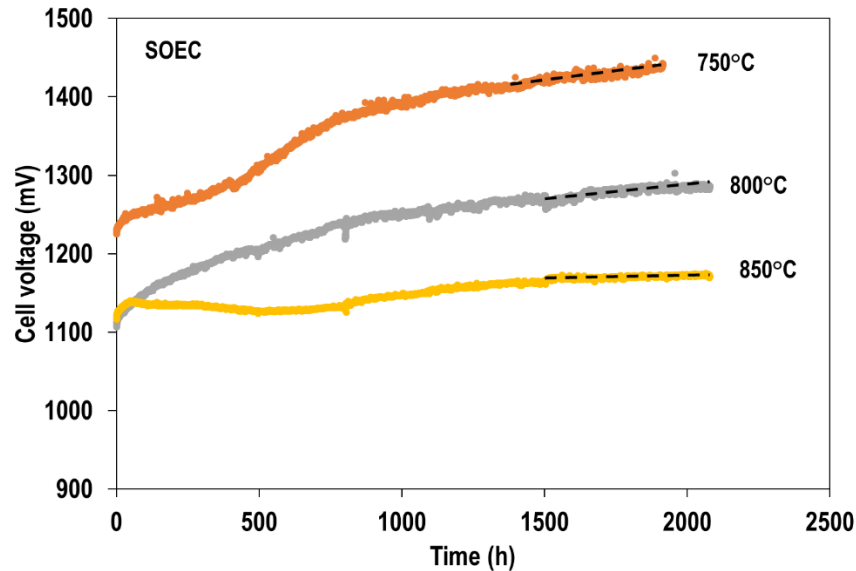


Figure 3-3: Durability curves showing the cell voltage increase for the cells aged at 750°C, 800°C and 850°C for 2000h in SOEC mode at  $-1 \text{ A}\cdot\text{cm}^{-2}$ , 64% SC,  $\text{pH}_2/\text{pH}_2\text{O}=10/90$  and  $12 \text{ Nml}\cdot\text{cm}^{-2}\cdot\text{min}^{-1}$ .

The effect of the temperature on the cell degradation has been investigated with three long-term tests of 2000h at 750°C, 800°C and 850°C in SOEC mode at  $-1 \text{ A}\cdot\text{cm}^{-2}$  with a steam conversion (SC) of 64% and  $\text{pH}_2/\text{pH}_2\text{O}=10/90$  and  $12 \text{ Nml}\cdot\text{cm}^{-2}\cdot\text{min}^{-1}$ . The Figure 3-3 shows the cell voltage degradation over the test

duration (2000h). The degradation rates are computed according to:  $100 \times \frac{(U_2 - U_1)}{U_1} \frac{1}{t_2 - t_1}$ . From the visual

inspection of the curves, an initial period exhibiting a fast and variable degradation rate is observed in the first 800h. After this transient period, the slope becomes less steep and tends to a rather constant rate value. From this second period, the voltage degradation rates have been calculated on the last 500h in the linear part of the durability curves for 750°C, 800°C and 850°C and achieve respectively: 2.8%/kh, 2%/kh and 0.8%/kh. Those values correspond to the following ones in mV/kh respectively: 39 mV/kh, 25 mV/kh and 9 mV/kh. These values lie in the range of the usual degradation rates reported in the literature for comparable cells [1] [2] [3] [4]. It is noteworthy that the durability curves  $U(t)$  lead to the 'apparent' degradation, which decreases with increasing the temperature [5]. Indeed, the impact of the electrodes degradation on the durability curve becomes less pronounced at higher temperatures because of the lower contribution of the electrodes activation overpotential to the total cell voltage. For this reason, it is worth to compare the performance degradation in the same reference conditions before and after the durability to evaluate the 'intrinsic' degradation in all the cases (as already explained in chapter 2). In

order to assess this degradation rates, the initial (0h) and final (2000h) electrochemical impedance spectra recorded in the reference conditions (at OCV and 750°C) have been plotted in the Nyquist and Bode plots for the three different operating temperatures in Figure 3-4 and are further analyzed.

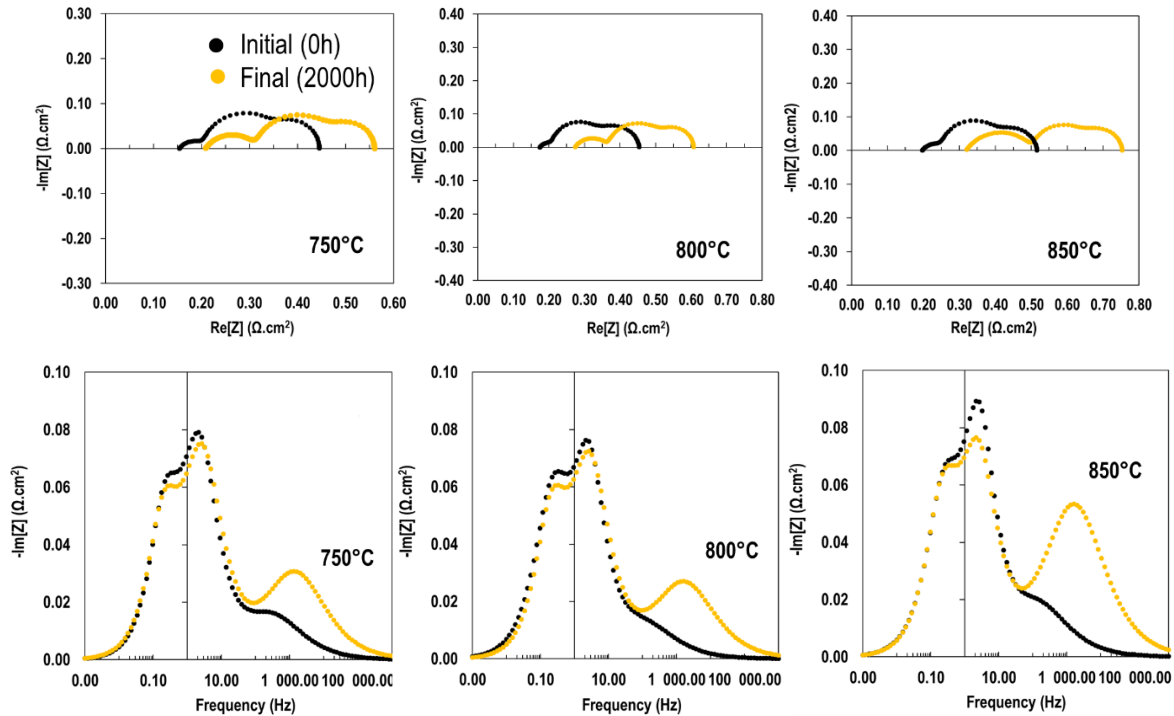


Figure 3-4: EIS diagrams in the Nyquist and Bode plots, measured at OCV,  $\text{pH}_2/\text{pH}_2\text{O}=10/90$ , 64% SC and 12  $\text{Nml} \cdot \text{cm}^{-2} \cdot \text{min}^{-1}$  for initial and final plot of the cells aged at 750°C, 800°C and 850°C for 2000h. The diagrams have been corrected of the wires inductance using EEC showed in Figure 3-3 of chapter 2.

**Table 3-3: Values and evolution of the series, polarization and high frequency resistances with temperature**

Samples (aged for 2000h)	750°C		800°C		850°C	
Time (h)	0h	2000h	0h	2000h	0h	2000h
$R_s$ ( $\Omega \cdot \text{cm}^2$ )	0.155	0.209	0.175	0.274	0.197	0.321
$R_p$ ( $\Omega \cdot \text{cm}^2$ )	0.291	0.352	0.279	0.333	0.319	0.433
$R_p$ HF ( $\Omega \cdot \text{cm}^2$ )	0.053	0.107	0.040	0.094	0.062	0.188

Their analysis as a function of time in the Nyquist plot reveals a significant global increase of both series and polarization resistances with a strong contribution of the high frequency arc whereas the low and medium frequency contributions remain almost unchanged (see table 3-3). The degradation rates of the ohmic and polarization resistances achieve 28, 48 and 59  $\text{m}\Omega \cdot \text{cm}^2/\text{kh}$  (i.e. 18, 27, 30 %/kh) for  $R_s$  and 32, 26 and 55  $\text{m}\Omega \cdot \text{cm}^2/\text{kh}$  (i.e. 11, 9, 17 %/kh) for  $R_p$  at 750°C, 800°C and 850°C respectively. In addition, the high frequency arc expressed as  $R_p$  HF in table 3-3 and related to the hydrogen electrode has also

increased. Its degradation rate is worth 28, 26 and 61  $\text{m}\Omega\cdot\text{cm}^2/\text{kh}$  (i.e. 53, 65, 97 %/kh) at 750°C, 800°C and 850°C respectively. It is worth noting that this evolution of the high frequency contribution becomes more pronounced as the ageing temperature increases. Moreover, the Bode plots in Figure 3-4 d)-f) emphasize the distinct separation of the three arcs which are associated [6]:

- 1) to the hydrogen electrode and LSCF/GDC ionic transfer at high frequencies,
- 2) the oxygen electrode and the gas diffusion in the support at medium frequencies,
- 3) the gas conversion at low frequencies (see chapter 2, section 1.3).

Thus, the evolution in both ohmic and high frequency resistances can be ascribed to the Ni migration away from the electrode/electrolyte interface towards the bulk of the hydrogen electrode, and the Ni coarsening. More specifically, the increase in the  $R_s$  is mostly attributed to the rate of Ni migration. Therefore, in this study, the main cell degradation is likely related to the hydrogen electrode since a degradation dependence on the temperature is found in the tested temperature range. Simultaneously, the degradation of the oxygen electrode seems to remain limited.

### 3.2.2 Effect of the ageing time

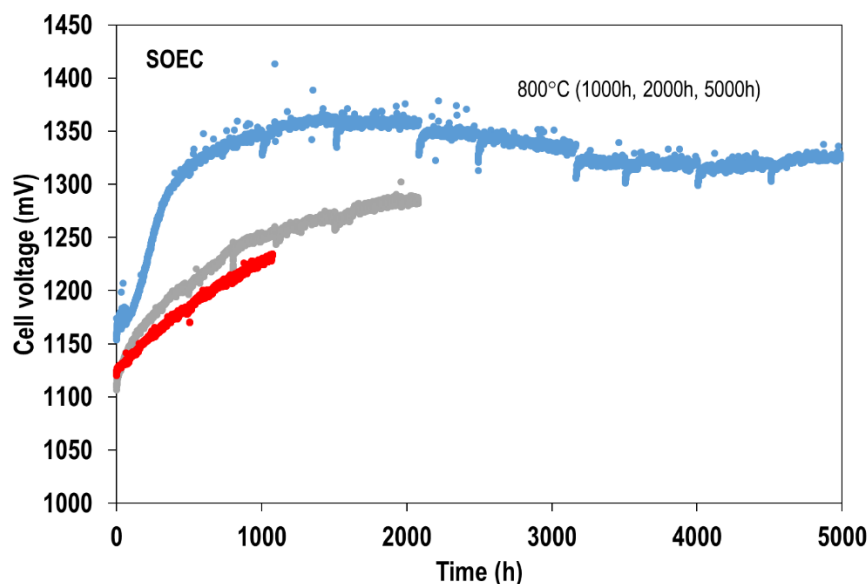


Figure 3-5: Durability curves showing the cell voltage increase for the cells aged at 800°C for 1000h, 2000h and 5000h in SOEC mode at  $-1 \text{ A}\cdot\text{cm}^{-2}$ , 64% SC,  $\text{pH}_2/\text{pH}_2\text{O}=10/90$  and  $12 \text{ NmL}\cdot\text{cm}^{-2}\cdot\text{min}^{-1}$ .

The durability curves of the cells tested at 800°C for 1000h, 2000h and 5000h in SOEC mode at  $-1 \text{ A}\cdot\text{cm}^{-2}$ , 64% SC,  $\text{pH}_2/\text{pH}_2\text{O}=10/90$  and  $12 \text{ NmL}\cdot\text{cm}^{-2}\cdot\text{min}^{-1}$  have been plotted in Figure 3-6. It is worth noting that, while 1000h and 2000h curves show an identical shape, the curve of the cell aged 5000h exhibits a

different behavior in the same conditions. Indeed, a strong degradation is observed in the first 500h even though the three cells presented similar initial performances (see cells 3, 4 and 6 in Figure 3-1). It could be due to a higher steam conversion (72% max. instead of targeted 64%) associated to a lower flow rate of steam at the inlet (constant but lower steam supply than expected, suggested by outlet water weighing all along the test). However, the apparent degradations tend to slow down after 2000h of ageing, with a voltage degradation rate lower than 2%/kh (20 mV/kh) for the last 1800h.

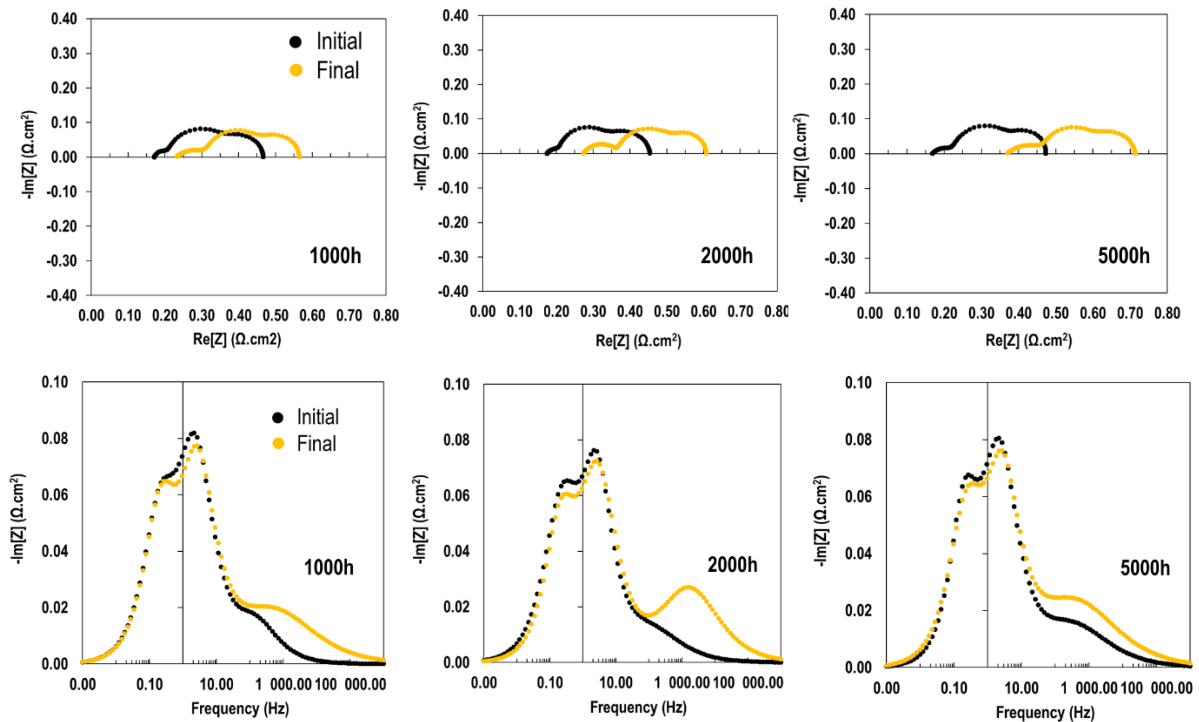


Figure 3-6: EIS diagrams in the Nyquist and Bode plots, measured at OCV, 750°C,  $p_{H_2}/p_{H_2O}=10/90$ , 64% SC and 12  $NmL.cm^{-2}.min^{-1}$  for initial and final plot of the cells aged 1000h, 2000h and 5000h at 800°C. The diagrams have been corrected of the wires inductance using EEC showed in Figure 3-3 of chapter 2.

**Table 3-4: Values and evolution of the series, polarization and high frequency resistances with ageing time**

Samples (aged at 800°C)	1000h		2000h		5000h	
Time (h)	0h	1000h	0h	2000h	0h	5000h
$R_s$ ( $\Omega.cm^2$ )	0.171	0.232	0.175	0.274	0.168	0.371
$R_p$ ( $\Omega.cm^2$ )	0.296	0.333	0.279	0.333	0.305	0.343
$R_p$ HF( $\Omega.cm^2$ )	0.039	0.092	0.040	0.094	0.063	0.113

The EIS spectra in the Nyquist and Bode plots have been plotted in Figure 3-6 for the three cells aged for 1000h, 2000h and 5000h. As already observed with 2000h results in the previous section, they also show an increase of the intrinsic  $R_s$ , the  $R_p$  and the high frequency contribution in operation (cf. table 3-4). The  $R_s$  and  $R_p$  degradation rates achieve respectively 57 and 34  $m\Omega.cm^2/kh$  (i.e. 33 and 11 %/kh) for the

1000h ageing, 48 and 26 m $\Omega$ .cm<sup>2</sup>/kh (i.e. 27 and 9 %/kh) for the 2000h ageing compared to 41 and 8 m $\Omega$ .cm<sup>2</sup>/kh (i.e. 24 and 3 %/kh) for the 5000h ageing. Moreover, the high frequency arc, which is associated to the hydrogen electrode, presents an evolution of 49, 26 and 10 m $\Omega$ .cm<sup>2</sup>/kh (i.e. 126, 65 and 15 %/kh) after 1000, 2000 and 5000h respectively. Therefore, it appears that the  $R_s$ ,  $R_p$  and  $R_p$  HF degradation rates have decreased by increasing the ageing time indicating a slowdown of the degradation over time.

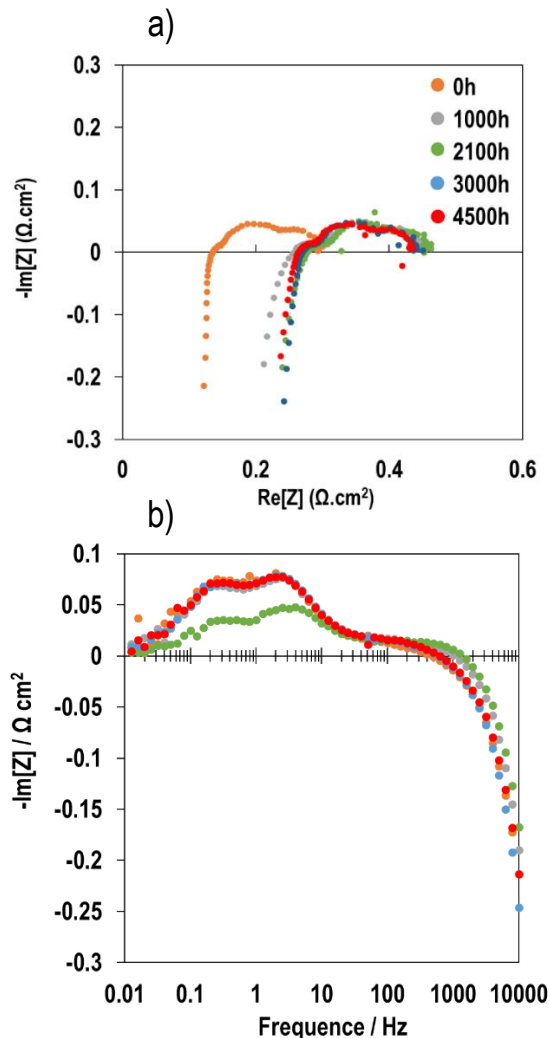


Figure 3-7: Evolution as a function of the time of the EIS diagrams in the a) Nyquist plot and b) Bode plot of the cell aged for 5000h in SOEC at 800°C.

It is consistent with the plot of the evolution as a function of the time of the EIS spectra (cf. Figure 3-7) that shows the  $R_s$ ,  $R_p$  and  $R_p$  HF almost superimposed after 1000h of ageing. This tendency suggests that the degradation and especially the degradations associated to the evolution of the Ni microstructure would slow down with time. Indeed, it is well known that the phenomenon of Ni agglomeration takes place during the first period of the test (i.e. <1000h) [5]. According to these observations, it seems that the Ni migration could also slow down over time with a possible stabilization after 1000h of ageing (in relation to the stabilising behaviour of the  $R_s$  over time).

### 3.2.3 Effect of the operating mode

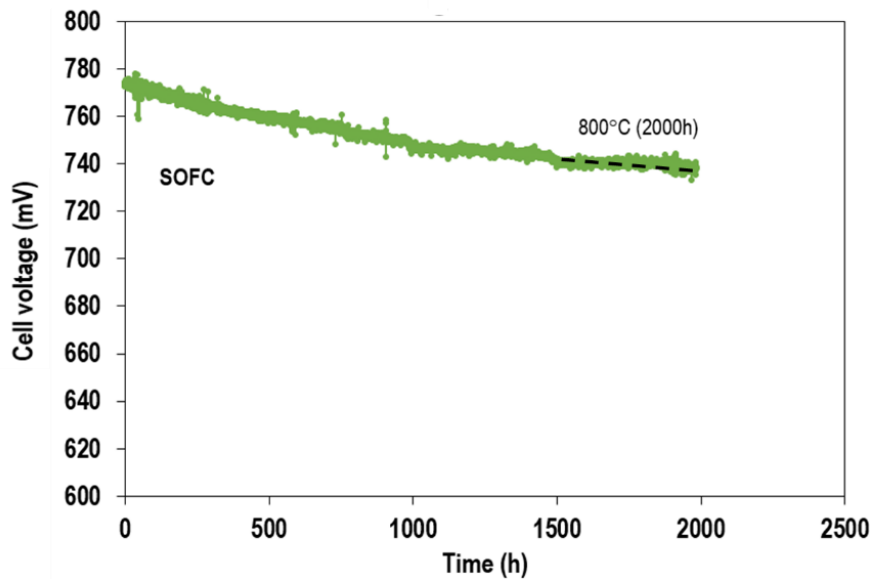
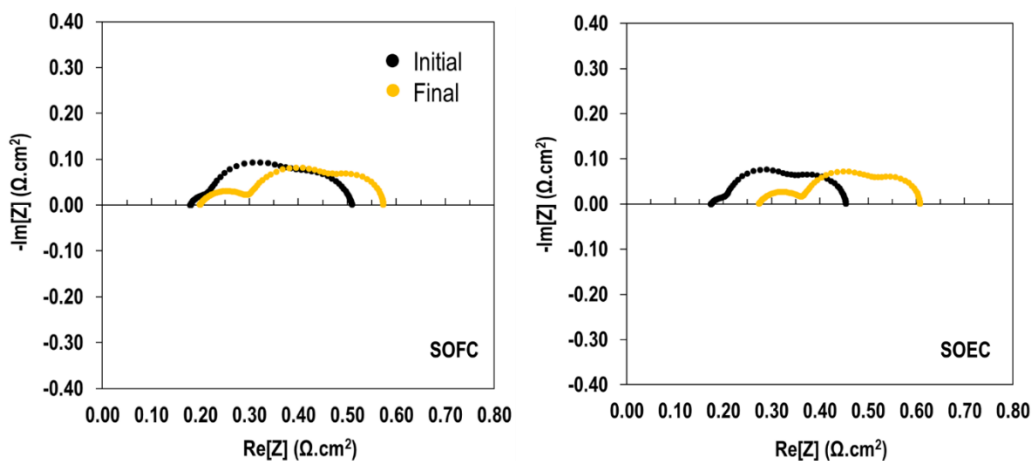


Figure 3-8: Durability curve showing the cell voltage evolution for the cell aged at 800°C for 2000h in SOFC mode at 1 A·cm<sup>-2</sup>, 64% of fuel utilization, p<sub>H<sub>2</sub></sub>/p<sub>H<sub>2</sub>O</sub>=90/10 and 12 Nml·cm<sup>-2</sup>·min<sup>-1</sup>.

The durability curve of the cell aged at 800°C for 2000h in SOFC mode at 1 A·cm<sup>-2</sup>, 64% of fuel utilization, 10 vol.% H<sub>2</sub>O and 90 vol.% H<sub>2</sub> and 12 Nml·cm<sup>-2</sup>·min<sup>-1</sup> is presented in Figure 3-8. As very often described in literature and mentioned in chapter 1, it shows a lower voltage evolution and a less pronounced transient period than in SOEC mode, for a voltage degradation rate of 0.76%/kh on the last 500h of the linear part and (i.e. 5.7 mV/kh).



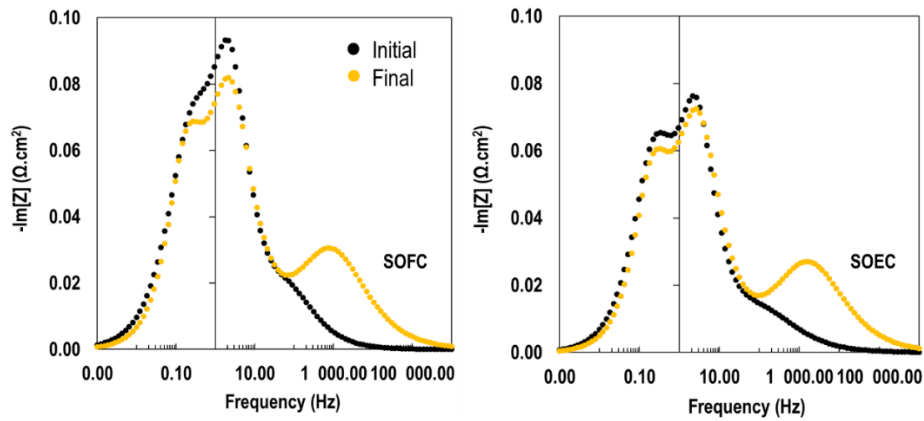


Figure 3-9: EIS diagrams measured at OCV, 750°C, 90 vol.% H<sub>2</sub>O and 10 vol.% H<sub>2</sub> and 12 Nm<sup>3</sup>.cm<sup>-2</sup>.min<sup>-1</sup> for the initial and final plot of the cells aged for 2000h at 800°C in SOFC and SOEC mode. The diagrams have been corrected of the wires inductance using EEC showed in Figure 3-3 of chapter 2.

According to Figure 3-9 and table 3-5, the thorough analysis of the EIS spectra reveals a different behavior compared to durability in SOEC mode. Only a slight increase of the  $R_s$  and  $R_p$  values is observed.  $R_s$  and  $R_p$  degradation rates of 10 and 23 mΩ.cm<sup>2</sup>/kh (5 and 7 %/kh) are calculated respectively (compared to 48 and 26 mΩ.cm<sup>2</sup>/kh (27 and 9 %/kh) after 2000h at 800°C in SOEC mode). Nevertheless a substantial increase of the high frequency arc is still observed with a degradation rate of 32 mΩ.cm<sup>2</sup>/kh (77 %/kh) (while 26 mΩ.cm<sup>2</sup>/kh (65 %/kh) after 2000h at 800°C in SOEC mode). As expected, the Ni agglomeration must be responsible of the increase of the high frequency arc while the origin of the very small  $R_s$  increase remains unclear.

**Table 3-5: Values and evolution of the series, polarization and high frequency resistances in SOFC and SOEC operation**

Samples (aged at 800°C for 2000h)	SOFC		SOEC	
	0h	2000h	0h	2000h
$R_s$ (Ω.cm <sup>2</sup> )	0.180	0.199	0.175	0.274
$R_p$ (Ω.cm <sup>2</sup> )	0.330	0.374	0.279	0.333
$R_p$ HF(Ω.cm <sup>2</sup> )	0.042	0.106	0.040	0.094

### 3.3 Post-test characterization

In addition to the electrochemical analyses, post-mortem characterizations have been performed in order to study the evolution of the cermet microstructure. The post-test characterizations include SEM images as well as EDX analyses for 2D observations and FIB-SEM reconstructions for 3D analysis. Moreover, the evolution of the microstructural properties extracted from the 3D volumes has also been studied. The impact of the operating conditions on the microstructural parameters has been analyzed in the different parts below, including the effect of the temperature, the operating time and the mode of functioning.

#### 3.3.1 SEM-EDX analysis

##### 3.3.1.1 Effect of the operating temperature

SEM images of the Ni-8YSZ functional layer have been acquired on the samples tested at different temperatures for 2000h in SOEC mode as well as EDX analyses in order to evaluate the evolution of the hydrogen electrode microstructure. Figure 3-11 presents images for the three different temperatures (750°C, 800°C and 850°C), taken at the gas inlet, which corresponds to the center of the cell, and compared to the reference cell. Figure 3-10 exhibits the SEM images taken at the gas inlet and at the gas outlet (cell periphery) of the cell aged at 800°C. First, it can be mentioned that the pristine cermet presents a homogeneous and rather fine microstructure as presented in Figure 3-10 a). From the observations of the aged cermet, the agglomeration of the Ni particles is detected in some places (Figure 3-10 b), c) and d)). Besides, a strong Ni depletion at the electrolyte interface is observed after operation, suggesting a strong Ni migration from the electrolyte interface to the electrode bulk. In addition, a detachment of the remaining Ni particles all along the electrolyte interface has been also seen as shown in Figure 3-11. It is worth noting that the higher is the temperature, the higher is the depleted thickness at the electrolyte interface. Indeed, the sample aged at 850°C exhibits the thickest Ni depleted layer at the interface with the electrolyte. It can also be noticed that the Ni depletion is more pronounced at the cell inlet than at the cell outlet as shown on Figure 3-10 as the current density is higher at the cell inlet due to a higher steam content. Therefore, the study of the SEM images as a function of the temperature confirms that a substantial Ni migration arises in electrolysis mode and is increased when increasing the operating temperature.

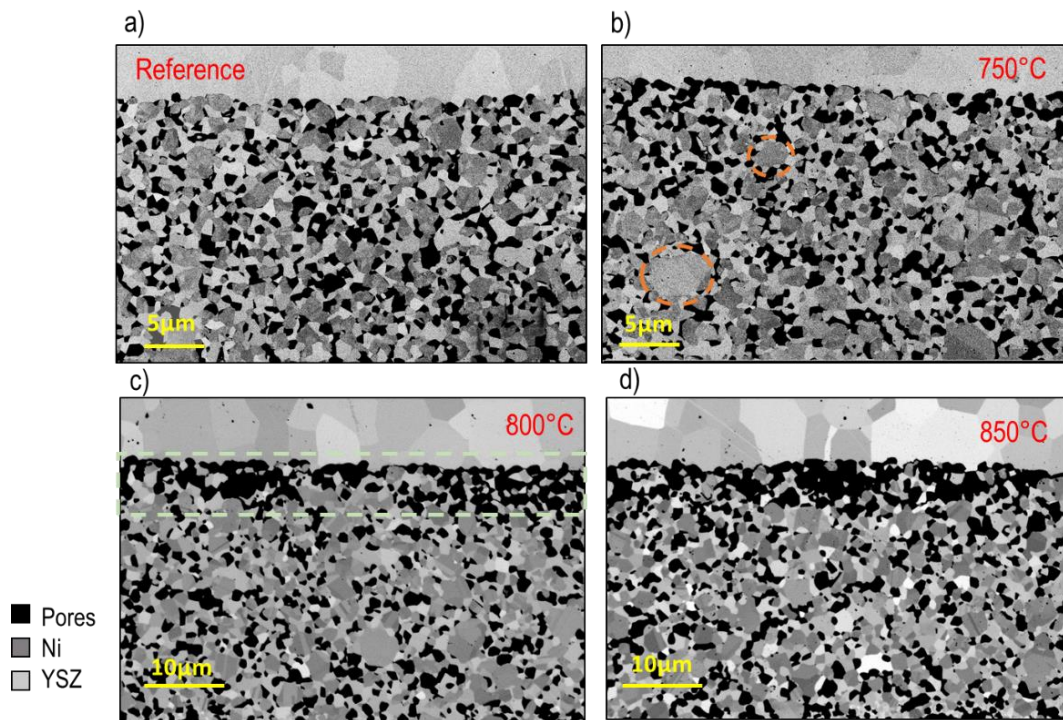


Figure 3-10: SEM images in back-scattering electrons of the Ni-YSZ/YSZ interface performed on a) the reference cell, and the cells aged b) at 750°C, c) at 800°C and d) at 850°C. The images are taken at the gas inlet (center of the cell). Ni coarsening is indicated by the orange dashed circles and Ni depletion by the green dashed lines.

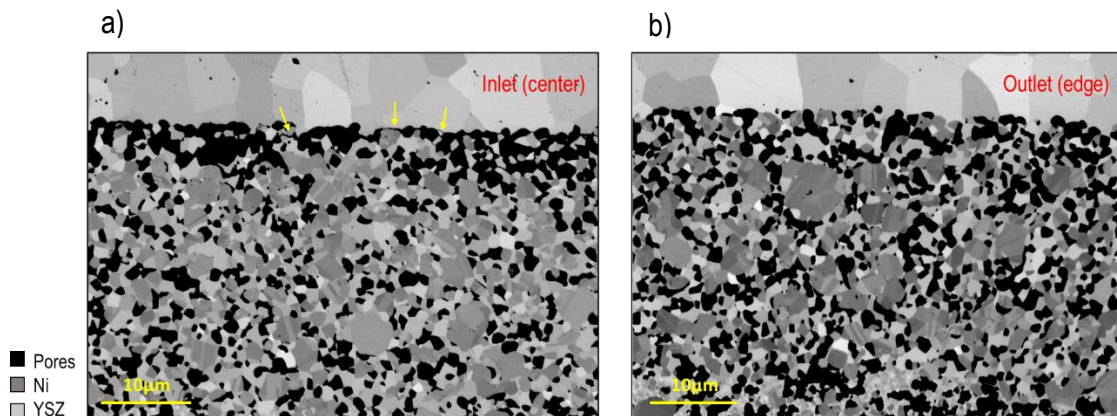


Figure 3-11: SEM images in back-scattering electrons of the Ni-YSZ/YSZ interface for the cell aged 2000h at 800°C: a) at the gas inlet (center of the cell), b) at the gas outlet (cell periphery). The yellow arrows show the detachment of the remaining Ni particles in the depletion zone.

In complementary to the SEM observations, EDX analyses have been used to highlight the Ni microstructural evolution under operation. It is worth noting that the profile of the Ni has been estimated (or quantified) by plotted the evolution of the grey levels in the Ni phase EDX cartographies (Annexe B). Therefore, the values obtained on each position on the profile are related to the Ni phase evolution. A large scale-view of 312 µm has been chosen to carry out the EDX analyses to ensure an accurate estimation of the profile. First, the evolution of the Ni volume fraction as a function of the electrode

thickness (Figure 3-12 a)) reveals after 2000h of ageing a substantial depleted layer of around 2, 3 and 5  $\mu\text{m}$  from the electrolyte interface for all the aged cells at 750°C, 800°C and 850°C respectively. More specifically, the Ni volume fraction decreases strongly in the depleted layer with increasing the temperature. Furthermore, in order to highlight the effect of the current density on the Ni migration all along the cell radius, Figure 3-12 b) shows the profile of the Ni volume fraction for the gas inlet and outlet position of the sample aged at 800°C. The plot at the outlet is almost superimposed with the reference one. The small difference is probably mostly associated to the agglomeration of the Ni particles. On the other hand, as already mentioned, a strong depletion is found at the cell inlet.

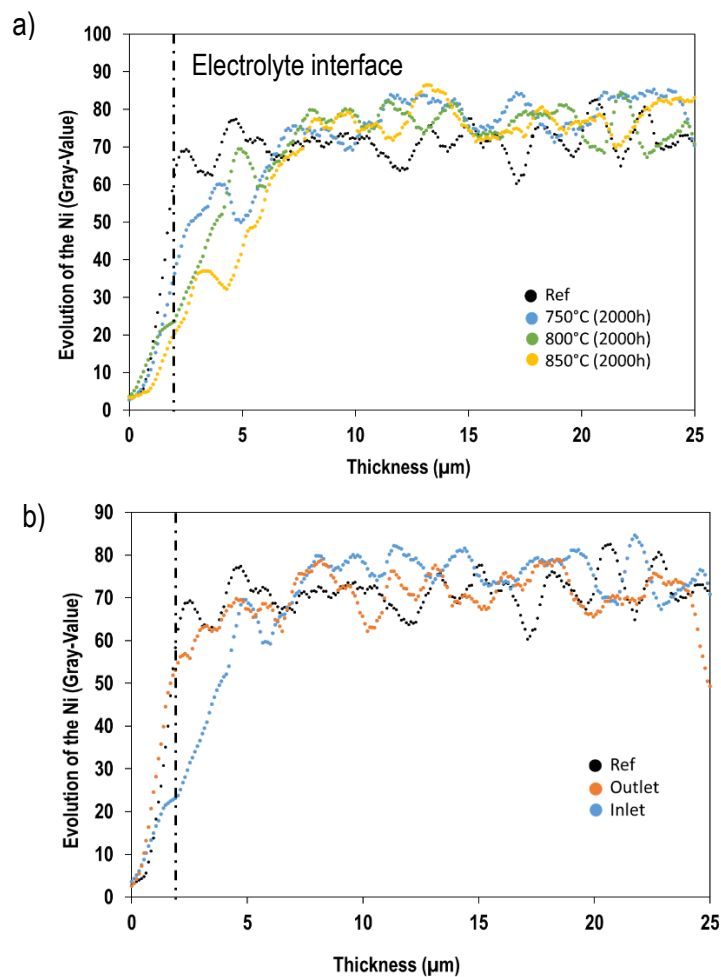


Figure 3-12: EDX analysis taken at the inlet of the Ni volume fraction for a) the samples aged at 750°C, 800°C and 850°C for 2000h in SOEC mode and b) for the samples aged at 800°C taken at the gas inlet and outlet in SOEC mode as a function of the electrode thickness (Cf. Appendix B for the EDX cartography of the Ni phase).

### 3.3.1.2 Effect of the ageing time

The SEM images taken at the cell inlet of the Ni-8YSZ functional layer are shown in Figure 3-13 for the cells aged for 2000h and 5000h at 800°C in SOEC mode. The two aged samples present a strong Ni agglomeration as well as Ni migration from the interface with the electrolyte. In addition, the zoom at the

interface on the cell aged for 5000h confirms a clear detachment of the remaining Ni particles all along the electrolyte interface.

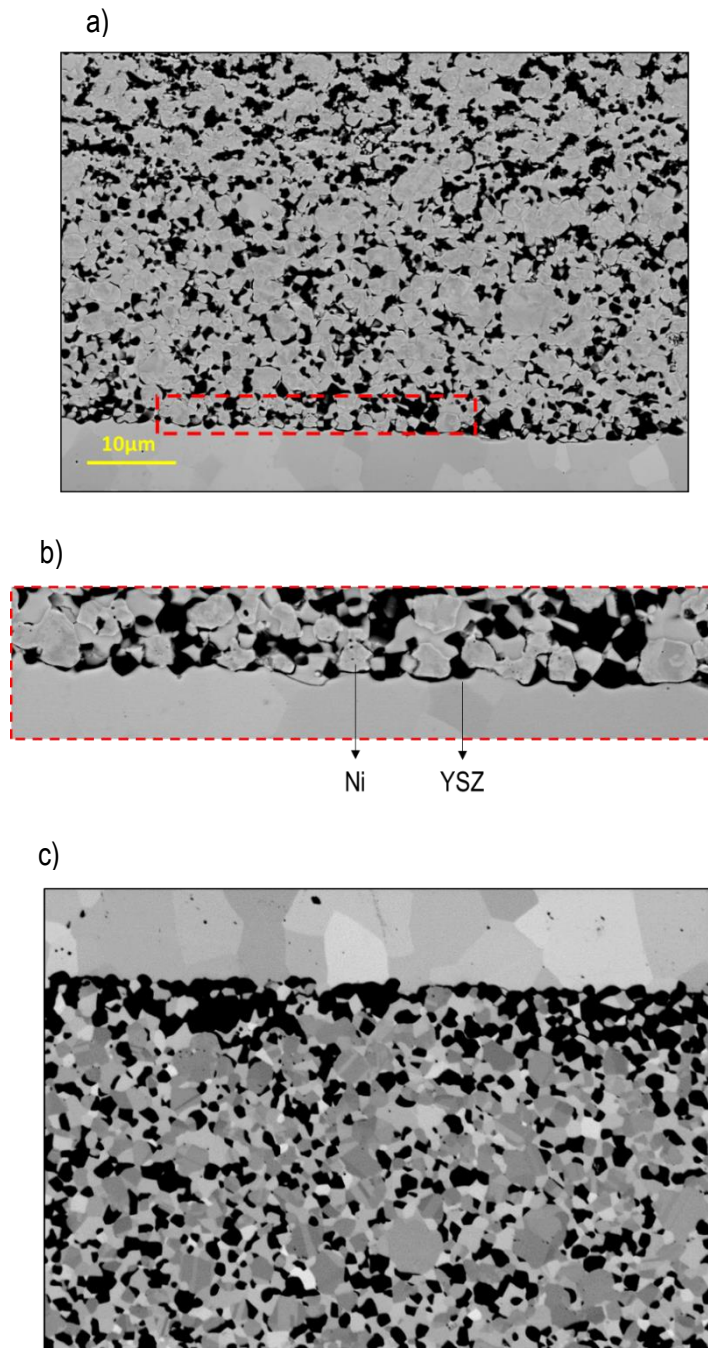


Figure 3-13: SEM images in secondary electrons of the Ni-YSZ/YSZ interface for a) the cell aged for 5000h at 800°C in SOEC mode, b) the zoomed interface and c) 2000h at 800°C in SOEC mode, taken all at the cell inlet. Pores in black.

As the size of the Ni depletion layer cannot be easily measured on the SEM image, EDX cartographies for Ni have been acquired on a large view of 312 µm. They allow estimating the evolution of the Ni volume

fraction as a function of the electrode thickness for the different ageing durations. The evolution of the reference cell and the ones aged at 800°C for 2000h and 5000h is plotted in Figure 3-14.

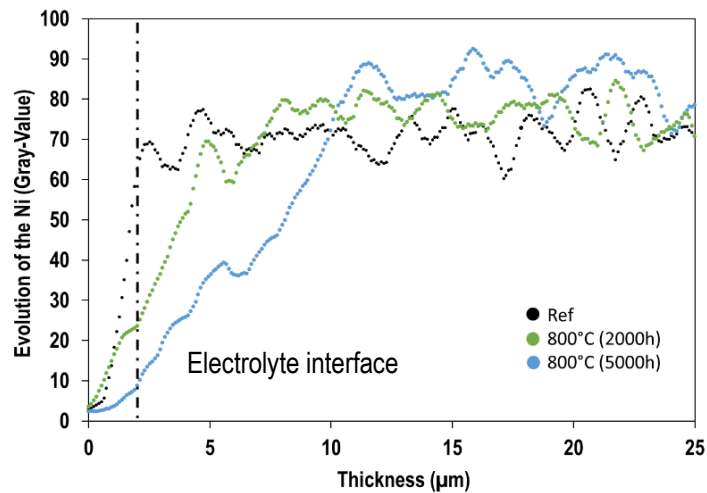


Figure 3-14: EDX analysis of the Ni volume fraction for the samples aged for 2000h and 5000h in SOEC mode at 800°C as a function of the electrode thickness (Cf. Appendix B for the EDX cartography of the Ni phase).

The evolution of the Ni volume fraction as a function of the electrode thickness exhibits an increasing thickness of the depleted layer as the ageing time increases between 2000 and 5000h. Therefore, even if the migration could slow down according to the electrochemical characterizations (in relation to the analysis of the evolution of the EIS and especially the decrease of the  $R_s$  and  $R_p$  HF degradation rate with time), the present microstructural observations would indicate that the Ni migration continue to occur after a long operating time.

### 3.3.1.3 Effect of the operating mode

The SEM images of the Ni-8YSZ functional layer are shown in Figure 3-15 for the cell aged for 2000h in SOFC mode. A strong agglomeration of Ni is visible after operation whereas no Ni migration is observed as expected [7]. Moreover, Ni particles present a good adhesion on YSZ at the electrode/electrolyte interface.

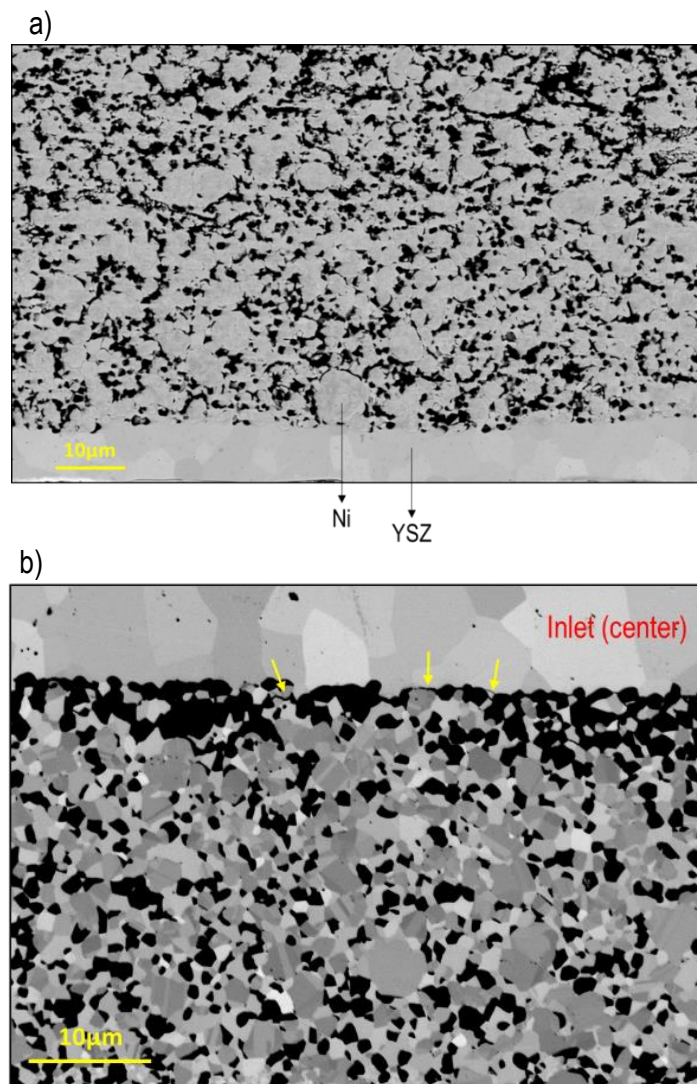


Figure 3-15: SEM image in secondary electrons of the Ni-YSZ/YSZ interface for the cells aged for 2000h at 800°C in (a) SOFC and (b) SOEC mode. Pores in black.

In addition, EDX analyses have also been performed on the sample at the interface with the electrolyte. Figure 3-16 compares the profiles of the Ni volume fraction for the cells aged for 2000h at 800°C in SOEC and SOFC modes. The curve of the cell aged in SOFC is almost superimposed to the reference one, the small difference is probably due to the Ni agglomeration.

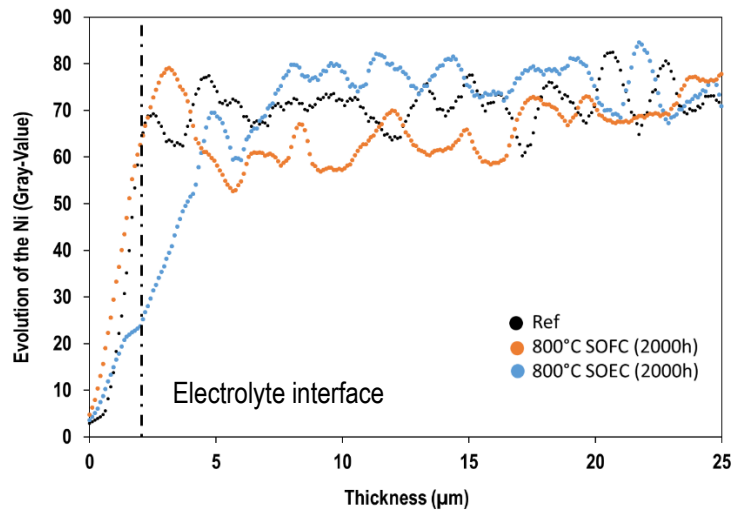


Figure 3-16: EDX analysis of the Ni volume fraction for the samples aged at 800°C for 2000h in SOFC and SOEC mode as a function of the electrode thickness (Cf. Appendix B for the EDX cartography of the Ni phase).

### 3.3.2 FIB-SEM reconstruction

FIB-SEM reconstructions have been done on the reference cell as well as on the samples aged at the three different operating temperatures. Since the rate of Ni migration depends on the cell position, the 3D reconstructions have been performed on samples extracted approximatively at the same distance from the cell inlet (at around 0.7 cm from the inlet of the cell). To quantify the microstructural evolution of the hydrogen electrode, the microstructural properties have been computed on the whole reconstructions.

#### 3.3.2.1 Effect of the operating temperature

Figure 3-17 represents the 3D reconstructed volumes of the reference cell and the ones aged at the different operating temperatures. Sub-volumes of  $18 \times 19 \times 22.4 = 7660.8 \mu\text{m}^3$  for the reference cell and  $24 \times 7.8 \times 22.4 = 4193.28 \mu\text{m}^3$ ,  $20 \times 20 \times 26 = 10400 \mu\text{m}^3$ ,  $20 \times 15 \times 22.16 = 6648 \mu\text{m}^3$  for the aged ones at 750°C, 800°C and 850°C respectively have been extracted from the whole reconstructions to calculate the microstructural properties of the percolated phases. First, from the visual inspection of the volumes, the Ni coarsening and migration after SOEC operation is confirmed as already seen on the SEM images and EDX profiles: compared to the pristine cermet, larger Ni particles are observed after ageing while the porosity is increased at the electrolyte interface. The computation of the microstructural properties on the whole reconstruction has revealed that the overall volume fractions of pore, Ni and YSZ for the pristine cell (respectively 0.247, 0.378 and 0.368) are very similar to the ones obtained after ageing at 750°C (respectively 0.235, 0.384 and 0.364), at 800°C (respectively 0.228, 0.382 and 0.376) and 850°C (respectively 0.215, 0.393 and 0.377). Nevertheless, the active TPB length density and the mean diameter of Ni particles reported for each cell in table 3-6 show expected evolutions related to Ni coarsening.

Indeed, the active TPB length density has decreased from  $2.39 \mu\text{m}^{-2}$  to  $2.36 \mu\text{m}^{-2}$ ,  $1.81 \mu\text{m}^{-2}$  and  $1.51 \mu\text{m}^{-2}$  for  $750^\circ\text{C}$ ,  $800^\circ\text{C}$  and  $850^\circ\text{C}$  respectively. In addition, the mean diameter of the Ni particles has increased from  $0.62 \mu\text{m}$  to  $0.67 \mu\text{m}$ ,  $0.77 \mu\text{m}$  and  $0.8 \mu\text{m}$  at  $750^\circ\text{C}$ ,  $800^\circ\text{C}$  and  $850^\circ\text{C}$  respectively.

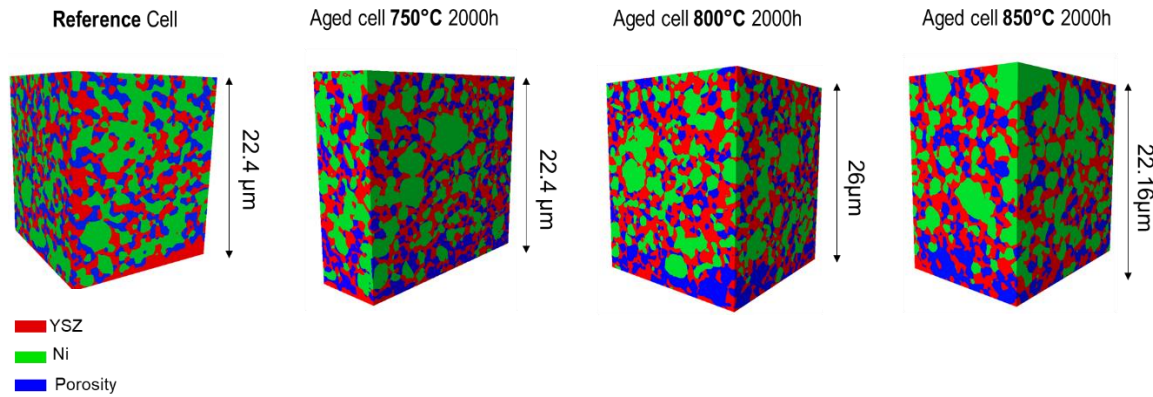


Figure 3-17: 3D FIB-SEM reconstructions of the hydrogen electrode performed on the reference, and the cells aged for 2000h at  $750^\circ\text{C}$ ,  $800^\circ\text{C}$  and  $850^\circ\text{C}$ . The reconstructions have been taken at around 0.7 cm from the cell center (gas inlet) and the electrolyte is located at the bottom of the volumes.

**Table 3-6: Values of the active TPB density and the Ni mean diameter as a function of the ageing temperature and compared to a reference cell.**

Samples (aged for 2000h, Ref excepted)	Ref	$750^\circ\text{C}$	$800^\circ\text{C}$	$850^\circ\text{C}$
Active TPB density ( $\mu\text{m}^{-2}$ )	2.3911	2.3637	1.8075	1.5087
Ni mean diameter ( $\mu\text{m}$ )	0.616	0.672	0.768	0.8

The positions of the mass center for the pore and Ni phases in the electrode have been also calculated on the reconstructions (Figure 3-18). It can be seen that during SOEC operation, the Ni phase moved away from the electrolyte interface whereas the center of mass for the pores is shifted toward the electrolyte interface. Moreover, the values of the mass center position for the Ni phase increase with increasing the temperature suggesting a stronger Ni depletion at the electrolyte interface at higher temperature. To highlight the Ni migration, the evolution of the phase volume fractions and active TPB density has been calculated as a function of the position in the electrode thickness according to the method reported in [8]. Their evolutions are plotted in Figure 3-19. Firstly, Figure 3-19 c) shows the evolution of YSZ volume fraction as a function of the electrode thickness for the reference cell and the three ageing temperatures. As expected, it is found that the YSZ phase is not changed after operation [9]. Secondly, the loss of Ni from the electrolyte interface (Figure 3-19 a)) takes place over a distance of around  $2.5 \mu\text{m}$  for the cell aged at  $750^\circ\text{C}$ ,  $4.5 \mu\text{m}$  for the cell aged at  $800^\circ\text{C}$  and to  $6.5 \mu\text{m}$  for the one aged at  $850^\circ\text{C}$ . Therefore, the Ni volume fraction decreases at the electrolyte interface as the ageing temperature increases (lower at  $850^\circ\text{C}$  compared to  $750^\circ\text{C}$  under the conditions of this study) (Figure 3-19 a)). This evolution is associated to a significant decrease in the density of active TPB that must

explain the cell degradation in performances (Figure 3-19 b)). Indeed, the decrease of the TPB density with the ageing temperature is stronger at the electrolyte interface and is greater as the temperature increases for a same location.

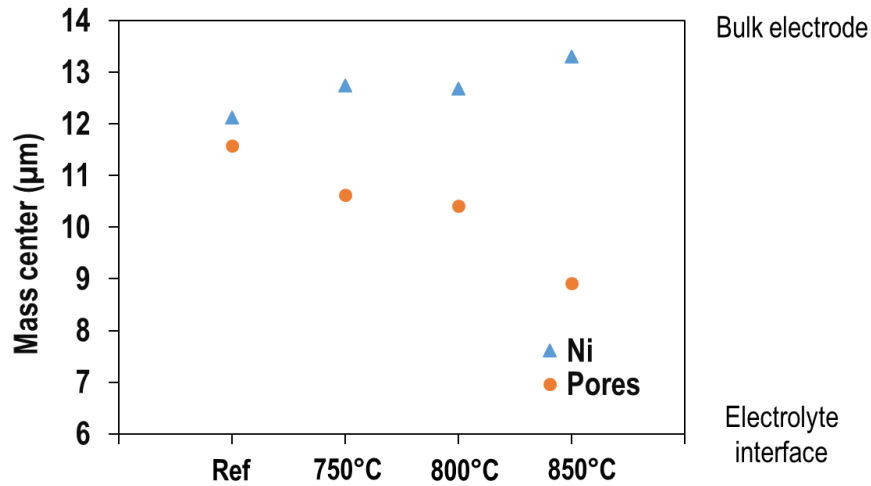


Figure 3-18: Mass center evolution of the cells aged for 2000h in SOEC mode as a function of the operating temperature.

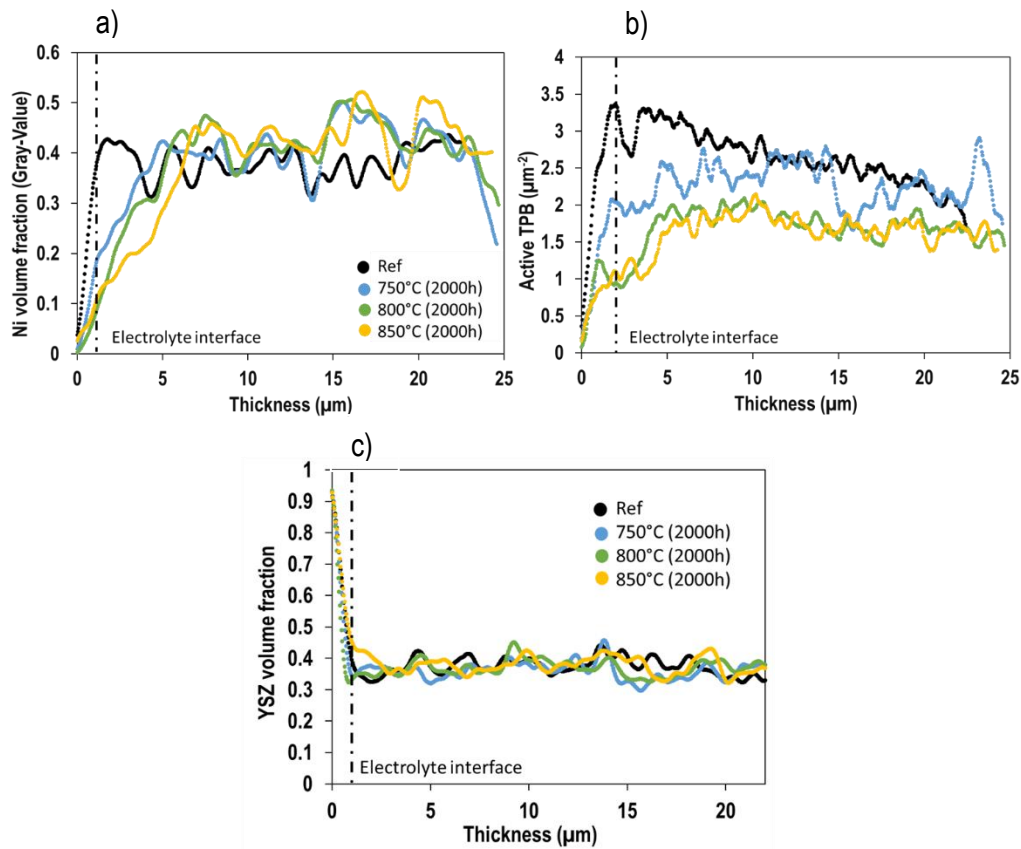


Figure 3-19: Evolution of the a) Ni and c) YSZ volume fraction and b) the active TPB density as a function of the electrode thickness after 2000h in SOEC mode at 750°C, 800°C and 850°C.

Therefore, 3D reconstructions confirmed the effect of the temperature on Ni migration already observed by SEM, by revealing a thicker depleted layer when increasing the temperature (higher thickness at 850 °C compared to 750 °C in the conditions of this study). This growth of the Ni depleted zone with ageing temperature could mostly explained the increase in the ohmic resistance measured by EIS previously.

### 3.3.2.2 Effect of the ageing time

Figure 3-20 represents the 3D reconstructed volumes of the cells aged for 2000h and 5000h at 800°C. The sub-volumes of the cells aged for 2000h and 5000h are respectively equal to  $18 \times 19 \times 21.5 = 7353 \mu\text{m}^3$ ,  $20 \times 20 \times 26 = 10400 \mu\text{m}^3$  and  $20 \times 11 \times 23.44 = 5156.8 \mu\text{m}^3$  and have been extracted from the whole reconstructions to calculate the microstructural properties of the percolated phases. First, from the visual inspection of the volumes, it is possible to see that the three volumes present Ni migration at the electrolyte interface.

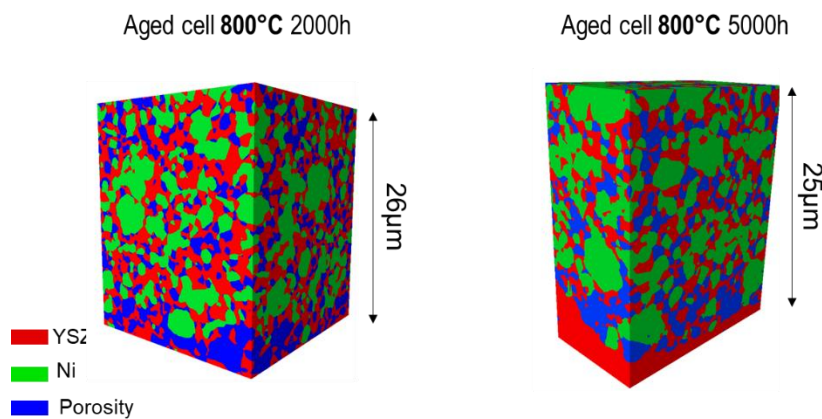


Figure 3-20: 3D FIB-SEM reconstructions of the hydrogen electrode performed on the cells aged for 2000h and 5000h at 800°C. The reconstructions have been taken at around 0.7 cm from the cell center (gas inlet).

The microstructural properties of the percolated phases have been computed. The most relevant properties for this study have been listed in table 3-7 and the profiles of the Ni volume fraction as well as the active TPB density have been plotted on Figure 3-22 as a function of the electrode thickness. The mean value of the active TPB density shows a decrease from  $2.39 \mu\text{m}^{-2}$  to  $1.81 \mu\text{m}^{-2}$  and  $1.59 \mu\text{m}^{-2}$  after ageing for 2000h and 5000 h respectively. Moreover, this global decrease of performance with time is accompanied by an increase of the Ni mean diameter from  $0.616 \mu\text{m}$  to  $0.768 \mu\text{m}$  and  $0.808 \mu\text{m}$  respectively. This increase of diameter reduces over time, which reveals the Ni agglomeration, slowing down with increasing time.

**Table 3-7: Values of the active TPB density and the Ni mean diameter as a function of the operating duration and compared to a reference cell.**

Samples (aged at 800°C, Ref excepted)	Ref	2000h	5000h
Active TPB density ( $\mu\text{m}^{-2}$ )	2.3911	1.8075	1.5897
Ni mean diameter ( $\mu\text{m}$ )	0.616	0.768	0.808

As a function of the ageing time, the positions of the mass center for the pore and Ni phases calculated on the all reconstructions suggest that the Ni phase moved away from the electrolyte interface whereas the pore phase moved in the opposite direction (Figure 3-21).

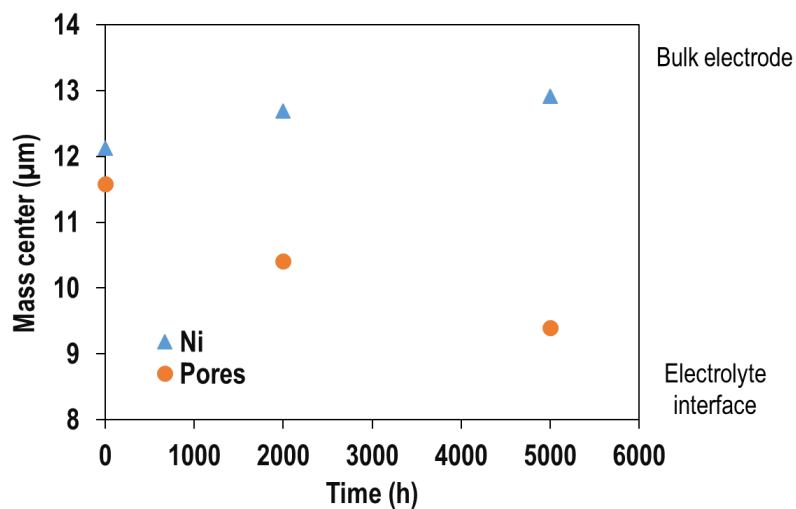


Figure 3-21: Mass center evolution of the cells aged at 800°C in SOEC mode as a function of the ageing time.

The profile of the Ni volume fraction has been plotted on Figure 3-22 a) and the one of the active TPB length density on Figure 3-22 b). It is possible to see a depleted layer of around 4  $\mu\text{m}$  for the samples aged for and 5  $\mu\text{m}$  for the one aged for 5000h. These observations are in good agreement with the previous MEB and EDX images. Moreover, the TPB length density has significantly decreased close to the electrode/electrolyte interface.

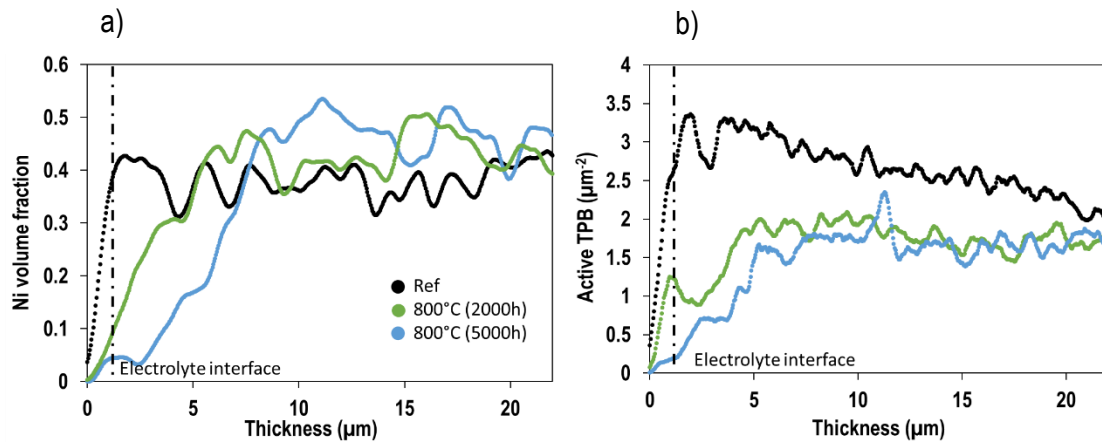


Figure 3-22: Evolution of a) the Ni volume fraction and b) the active TPB density as a function of the electrode thickness in SOEC mode after 2000h and 5000h at 800°C.

As already mentioned above in the discussion, despite the uncertainties related to the experimental conditions (composition of the steam inlet or procedure for the post-test characterization), these evolutions are consistent with a possible slowdown of the Ni migration. Nevertheless, another series of tests should be necessary to strengthen this observed tendency.

### 3.3.2.3 Effect of the operating mode

The 3D reconstruction of the cell aged in SOFC has been shown in Figure 3-23 and has a size of  $20 \times 18 \times 23.52 = 8467.2 \mu\text{m}^3$ . The volume presents a strong Ni agglomeration whereas no Ni migration neither from the electrolyte interface nor toward this interface is detected.

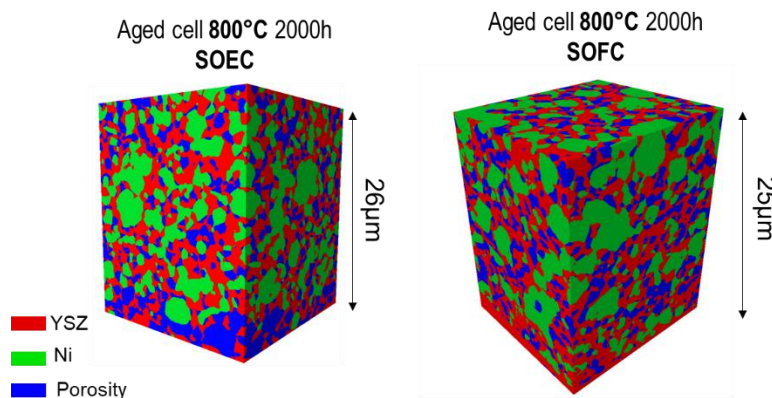


Figure 3-23 : 3D FIB-SEM reconstruction of the hydrogen electrode performed on the cell aged for 2000h at 800°C in SOFC mode. The reconstruction has been taken at around 0.7 cm from the cell center (gas inlet).

Again, the microstructural properties of this sample have been computed on the percolated phases and the most relevant ones for this study are reported in table 3-8. In accordance with the visual observation of the reconstructed volume, the Ni mean diameter has strongly increased from  $0.616 \mu\text{m}$  to  $0.912 \mu\text{m}$  and the active TPB density has decreased from  $2.39 \mu\text{m}^{-2}$  to  $1.47 \mu\text{m}^{-2}$ . Those evolutions are obviously

due to the Ni agglomeration. As a matter of fact, it is worth noting that these evolutions are dependent on the reference as well as the initial microstructure of each sample.

**Table 3-8: Values of the active TPB density and the Ni mean diameter as a function of the functioning mode and compared to a reference cell.**

Samples (2000h-800°C, Ref excepted)	Ref	SOFC	SOEC
Active TPB length density ( $\mu\text{m}^{-2}$ )	2.3911	1.4701	1.8075
Ni mean diameter ( $\mu\text{m}$ )	0.616	0.912	0.768

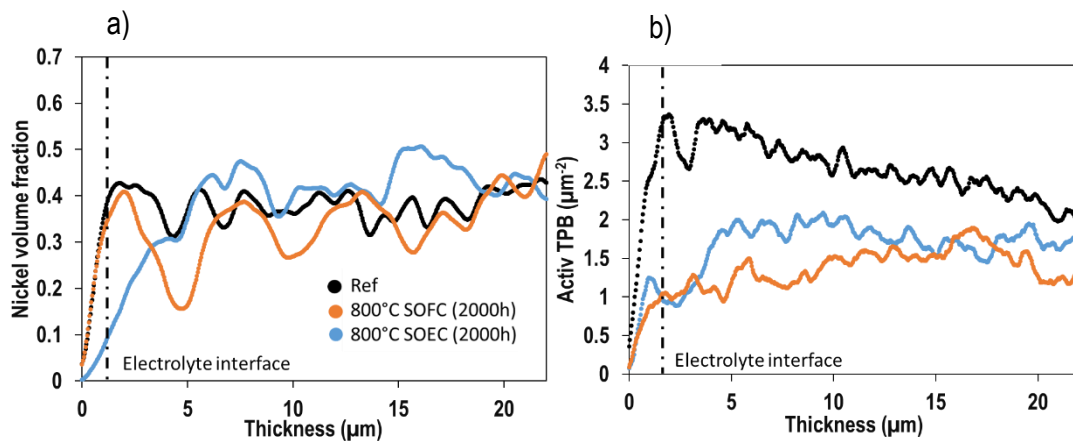


Figure 3-24: Evolution of a) the Ni volume fraction and b) the active TPB density as a function of the electrode thickness in SOEC and SOFC modes after 2000h at 800°C.

The profiles of the Ni volume fraction as well as the active TPB density are plotted in Figure 3-24 a) and b) respectively. The evolution of the Ni volume fraction in SOFC mode after 2000h of ageing is in the same range of the reference one with no sign of Ni migration close to the electrolyte interface. The profile with larger “waves” also highlights the Ni agglomeration in the microstructure, which is in accordance with the  $R_p$  HF increase already observed. However, the profile of the active TPB density shows a strong decrease after ageing which is in the same trend as the one after SOEC ageing.

### 3.4 Conclusion

This chapter was dedicated to the experimental results obtained from the various tests conducted in this work. First, it has been seen that the initial performances of the different tested cells are similar, which ensures a similar starting point for all of them. The electrochemical characterizations including durability curves,  $i$ - $U$  curves and EIS spectra in the Nyquist and Bode plots have been presented and thoroughly analyzed. From this study, it has been established that the apparent voltage degradation from the durability curves decreases when the operating temperature increases. It has been also shown that the degradation rates tend to slow down after  $\approx 1000$ h, achieving a steady-state value in the studied range of time (up to 5000h). In order to assess the intrinsic degradation, the initial and final EIS diagrams recorded in a reference condition have been analyzed. An increase in the series resistance, the polarization one and the high frequency arc associated to the hydrogen electrode has been detected in SOEC mode. This increase is stronger at higher operating temperatures but appears to slow down all along operation (for an increasing ageing time at a fixed temperature). On the contrary, the test in SOFC mode has only revealed a slight increase of  $R_s$  and  $R_p$  values while a strong increase in the HF frequency arc. In the second part, the microstructural post-test characterization has allowed highlighting the associated degradation phenomena of the hydrogen electrode. It has been shown that the increase in the ohmic losses is mostly attributed to the Ni depletion while the increase of the high frequency arc is related to both the Ni agglomeration and migration. Indeed, a strong Ni depletion as well as Ni agglomeration at the electrolyte interface has been observed after ageing in electrolysis mode while in SOFC mode, only significant Ni agglomeration is observed. Additionally, the rate of the Ni depletion at the electrolyte interface in SOEC mode increases with the operating temperature from 750 °C to 850 °C. As confirmed by the evolution of the EIS with the time for the cells aged 1000h, 2000h and 5000h, as well as the study of the ones acquired all along the 5000h ageing; the evolution of the  $R_s$  seems to stabilize after 1000h of ageing. Consequently, it can be supposed that the rate of Ni depletion, mostly associated to the  $R_s$  tends to slow down. Therefore, further experiments are mandatory in order to well understand the effect of the operating parameters on the Ni migration, in particular to clarify the evolution of the Ni migration over time.

## Bibliography of chapter 3

- [1] X. Sun, P. V. Hendriksen, M. B. Mogensen, and M. Chen, 'Degradation in Solid Oxide Electrolysis Cells During Long Term Testing', *Fuel Cells*, vol. 19, no. 6, pp. 740–747, 2019, doi: 10.1002/face.201900081.
- [2] J. Schefold, A. Brisse, M. Zahid, J. P. Ouweltjes, and J. U. Nielsen, 'Long Term Testing of Short Stacks with Solid Oxide Cells for Water Electrolysis', *ECS Trans.*, vol. 35, no. 1, pp. 2915–2927, Apr. 2011, doi: 10.1149/1.3570291.
- [3] A. Hauch, S. D. Ebbesen, S. H. Jensen, and M. Mogensen, 'Solid Oxide Electrolysis Cells: Microstructure and Degradation of the Ni/Yttria-Stabilized Zirconia Electrode', *J. Electrochem. Soc.*, vol. 155, no. 11, p. B1184, 2008, doi: 10.1149/1.2967331.
- [4] G. Schiller, A. Ansar, M. Lang, and O. Patz, 'High temperature water electrolysis using metal supported solid oxide electrolyser cells (SOEC)', *J. Appl. Electrochem.*, vol. 39, pp. 293–301, 2009, doi: 10.1007/s10800-008-9672-6.
- [5] M. Hubert, J. Laurencin, P. Cloetens, B. Morel, D. Montinaro, and F. Lefebvre-Joud, 'Impact of Nickel agglomeration on Solid Oxide Cell operated in fuel cell and electrolysis modes', *J. Power Sources*, vol. 397, pp. 240–251, Sep. 2018, doi: 10.1016/j.jpowsour.2018.06.097.
- [6] G. Sassone, E. Da Rosa Silva, M. Prioux, M. Hubert, B. Morel, A. Léon and J. Laurencin, 'Multiscale Modelling of Solid Oxide Cells Validated on Electrochemical Impedance Spectra and Polarization Curves', *ECS Trans.*, vol. 111, no. 6, pp. 649–661, May 2023, doi: 10.1149/111106.0649ecst.
- [7] M. Trini, A. Hauch, S. De Angelis, X. Tong, P. V. Hendriksen, and M. Chen, 'Comparison of microstructural evolution of fuel electrodes in solid oxide fuel cells and electrolysis cells', *J. Power Sources*, vol. 450, p. 227599, Feb. 2020, doi: 10.1016/j.jpowsour.2019.227599.
- [8] F. Monaco, M. Hubert, J. Vulliet, J.P. Ouweltjes, D. Montinaro, P. Cloetens, P. Piccardo, F. Lefebvre-Joud and J. Laurencin, 'Degradation of Ni-YSZ Electrodes in Solid Oxide Cells: Impact of Polarization and Initial Microstructure on the Ni Evolution', *J. Electrochem. Soc.*, vol. 166, no. 15, pp. F1229–F1242, 2019, doi: 10.1149/2.1261915jes.
- [9] M. Trini, P. S. Jørgensen, A. Hauch, M. Chen, and P. V. Hendriksen, 'Microstructural Characterization of Ni/YSZ Electrodes in a Solid Oxide Electrolysis Stack Tested for 9000 Hours', *ECS Trans.*, vol. 78, no. 1, pp. 3049–3064, May 2017, doi: 10.1149/07801.3049ecst.

## 4. Modeling the Ni migration

This thesis is devoted to a better understanding of the Ni migration based on an original and new mechanism to account for the microstructural change observed in the hydrogen electrode. This chapter is thus dedicated to the modeling and the simulation of the Ni microstructural evolution in the cermet. The approach adopted in this work was based on the coupling of electrochemical and phase field modelling.

Firstly, the multi-scale electrochemical model has been calibrated based on the validation presented in chapter 2 for the cells used in this work. The results of this calibration are presented in the first part of this chapter. The second part of this chapter is dedicated to the mechanism to account for the Ni migration based on the evolution of the Ni/YSZ interface (and so the Ni/YSZ contact angle) depending on the electrode overpotential. A coupling between the multi-scale electrochemical model and the developed phase-field model was necessary. Indeed, the electrochemical model has been used to assess the gradient in Ni/YSZ contact angle in both SOEC and SOFC modes and then applied them as boundary conditions for the simulation of the Ni migration by the phase-field model. In this context, the following section details the procedure and the equations used for the computation of the gradient in Ni/YSZ contact angle. The third part is dedicated to the developed phase-field model, which includes the theory of the method applied to reproduce the Ni migration as well as the validation of the numerical implementation. It is worth noting that an Appendix 1 has been added at the end of the thesis document in order to well explain the phase-field theory. Finally, the last part presents, in a first section, the results obtained from the multi-scale electrochemical model and, more specifically the computed gradients in Ni/YSZ contact angle in both SOEC and SOFC modes. The second section is dedicated to the results of the phase-field simulations in SOEC and SOFC modes after an operation of 2000h in the conditions of the experiments in order to prove the relevance of the mechanism. Furthermore, a discussion about the results in regard to the bibliography is included at the end of this chapter.

### 4.1 Electrochemical validation

In this work, the multi-scale electrochemical model presented in the chapter 2 has been coupled to a phase-field model to simulate the Ni migration. Indeed, the electrochemical multi-scale model has been used to assess the gradients in Ni/YSZ contact angle, which are considered as the driving force for the Ni migration. As already presented in chapter 2, the adaptations of the multi-scale model to the studied cells have been performed in collaboration with the post-doc of Eduardo Da Rosa Silva and the PhD

thesis of Giuseppe Sassone [1] [2]. In this frame, the model has been calibrated to reproduce the performance of the cells used for this thesis. On the one hand, the Figure 4-1 displays the result of the calibration with the simulated polarization curve in SOEC mode compared to the experimental one. It is worth noting that a general good agreement is found between the experimental curve and the simulated one. More specifically, the model is able to capture correctly the limiting current density at high steam conversion in SOEC mode [1]. On the other hand, the electrochemical spectra in the Nyquist and Bode plots for the SOEC mode are reported in Figure 4-2 a) and b) respectively and have been corrected using the EECM depicted in the second chapter. A good match is also found between the simulated and the experimental impedance spectra as shown in Figure 4-2 for both plots, especially after correction of the microstructural properties (see Figure 2-8 in chapter 2).

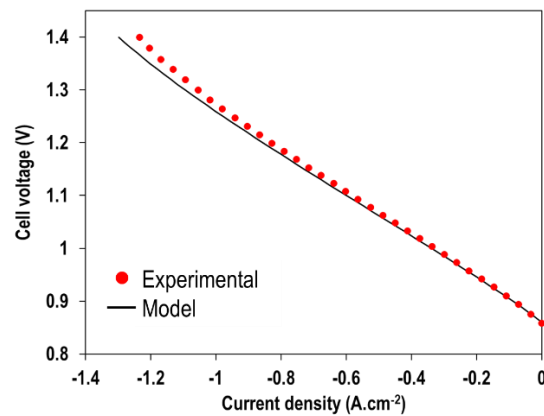


Figure 4-1: Simulated and experimental i-U curves at 750°C in SOEC mode for  $p_{H_2}/p_{H_2O} = 0.1/0.9$  and 12  $Nml.cm^{-2}.min^{-1}$ .

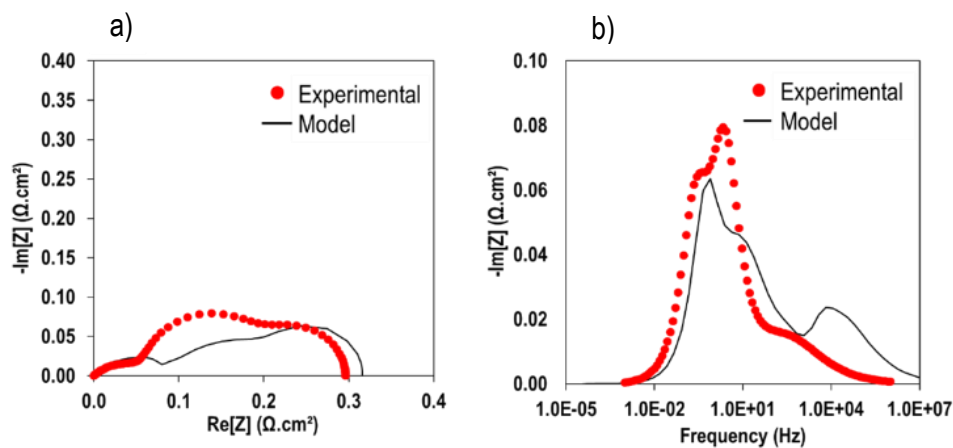


Figure 4-2: Simulated and experimental EIS spectra after correction with the EECM, at OCV, 750°C,  $p_{H_2}/p_{H_2O} = 0.1/0.9$  and 12  $Nml.cm^{-2}.min^{-1}$ , a) in Nyquist plot, b) in Bode plot.

## 4.2 Mechanism for the Ni migration in both SOEC and SOFC modes

### 4.2.1 Description of the proposed mechanism

As discussed in the chapter dedicated to the bibliography, some mechanisms have been already proposed in the literature to account for the Ni migration in both SOEC and SOFC modes. It is worth noting that whatever the mechanisms, they all agree that the electrode overpotential should be the driving force for the Ni migration. More specifically, in this thesis the proposed mechanism is based on a change of the Ni/YSZ interfacial energy under polarization. Indeed, the oxygen vacancies concentration in the electrochemical double layer (act as a capacitor) can be significantly affected by the local electrode overpotential if considering a blocking electrode (i.e. an ideally polarizable electrode). It is worth noting that this case must be well representative of the bulk of the Ni/YSZ interface away from the TPBs lines (where there is no electrochemical reaction). In this condition, the concentration of vacancies in the vicinity of the Ni/YSZ interface can be estimated as a function of the position in the electrode (*radius r, thickness z*) through the local overpotential  $\eta(r, z)$  and is plotted in Figure 4-3 [3]:

$$C_{V\ddot{o}}^{int}(r, z) = \frac{C_{V\ddot{o}}^{max} C_{V\ddot{o}}^{bulk} \exp\left(-\frac{2F}{RT} \eta(r, z)\right)}{C_{V\ddot{o}}^{max} + C_{V\ddot{o}}^{bulk} \left(\exp\left(-\frac{2F}{RT} \eta(r, z)\right) - 1\right)} \quad 4-1$$

where  $C_{V\ddot{o}}^{int}$ ,  $C_{V\ddot{o}}^{max}$  and  $C_{V\ddot{o}}^{bulk}$  denote respectively the oxygen vacancy concentration at the Ni/YSZ interface, the maximum and the bulk concentrations in YSZ. The term  $C_{V\ddot{o}}^{bulk}$  is expressed as a function of the molar percentage of Ytria in 8YSZ, i.e.  $\%Y_2O_3 = 0.08$ , the volume of the unit cell  $V_{uc}$  for cubic zirconia and the Avogadro's number  $Na$ :

$$C_{V\ddot{o}}^{bulk} = 4 \cdot \frac{\%Y_2O_3}{V_{uc} \cdot Na} \quad 4-2$$

In the model, it is assumed that the maximum concentration  $C_{V\ddot{o}}^{max}$  of vacancies in the double layer is reached when all the oxygen atoms have been removed from YSZ surface:

$$C_{V\ddot{o}}^{max} = \frac{8}{V_{uc} \cdot Na} \quad 4-3$$

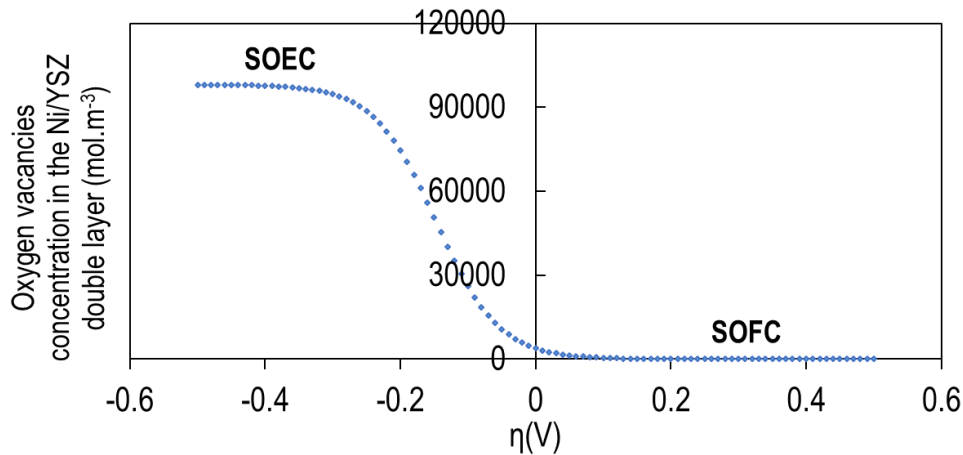


Figure 4-3: Evolution of the oxygen vacancies concentration in the Ni/YSZ double layer as a function of the electrode overpotential.

For a radial position  $r$  along the cell radius (cf. Figure 4-4), the local overpotentials present a steep gradient in the depth of the electrode  $z$  with higher absolute value at the electrolyte interface ( $z = 0$ ) than at the top of the active layer ( $z = \ell$ ):  $|\eta_{act}(r, z = 0)| > |\eta_{act}(r, z = \ell)|$  (Figure 4-10) (cf. system of coordinates in Figure 4-4). It can be noted that, for a given current density, a higher gradient in local electrode overpotentials is expected in SOEC mode with respect to the SOFC one (because of the dissymmetry of the electrode polarization curve [4]). According to equation 4-1, these gradients will induce a variation in oxygen vacancies concentration in the double layer as a function of the electrode thickness. As depicted in Figure 4-4, a strong accumulation of oxygen vacancies in the double layer should appear at the electrolyte interface ( $z = 0$ ) in SOEC mode while a moderate oxygen vacancies is expected in SOFC mode. The oxygen vacancies in the double layer are liable to significantly affect the adhesion between both materials and hence the wettability of Ni onto YSZ (which is the ability of the Ni to maintain contact with the YSZ surface). Indeed, the Ni/YSZ adhesion is mainly ensured by the Ni-O bonds at the interface between the metal and the ceramic [5]. Therefore, the modification of the oxygen vacancies concentration in the double layer under polarization will change the number of bonds at the interface. Under cathodic polarization, the interface must be weakened since the oxygen atoms participating to the adhesion are replaced by the oxygen vacancies accumulated in the double layer. Because of the gradient in overpotentials (and hence in oxygen vacancies), the Ni adhesion onto YSZ must be preferentially lowered at the electrolyte interface ( $z = 0$ ). As a consequence, a gradient in Ni/YSZ contact angle related to the Ni wettability onto YSZ should arise in the electrode thickness with higher values at the electrolyte interface than in the bulk as illustrated in Figure 4-4. This gradient could constitute the driving force for the Ni migration away from the electrolyte interface in SOEC mode. Conversely, the Ni/YSZ interface must be strengthened under anodic polarization by the depletion of vacancies in the double layer. In other words, the adhesion should be enhanced especially at the electrolyte interface. Accordingly, a wettability gradient

should appear in the electrode thickness with a lower Ni/YSZ contact angle at the electrolyte interface (Figure 4-4). These gradients could thus explain the Ni enrichment at the electrolyte interface observed after SOFC operation in literature [6]. It is worth noting that the strong accumulation of vacancies and the steep gradients under cathodic polarization would trigger a rapid Ni depletion as experimentally observed while the lower gradients in SOFC mode should be consistent with the slow Ni enrichment at the electrolyte interface, not observed experimentally even after 2000h in this work.

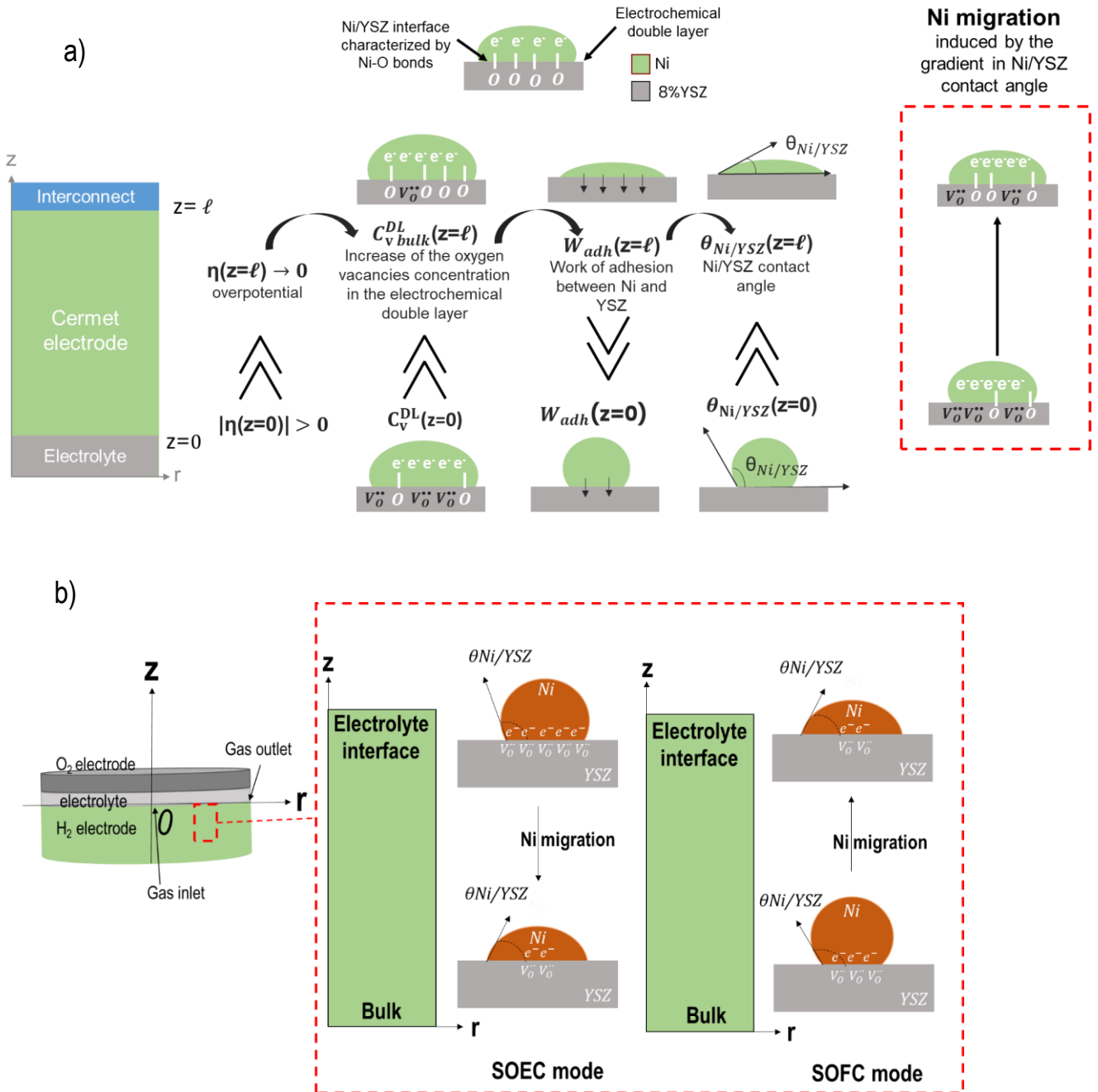


Figure 4-4: a) Schematic explanation of the Ni migration mechanism from the overpotential gradient to the contact angle one and b) Schematic representations of the Ni migration mechanism in both SOEC and SOFC modes with the system of coordinates.

#### 4.2.2 Equation for the computation of the gradients in Ni/YSZ contact angle

In this section, the method to calculate the gradients in Ni/YSZ contact angle is presented. They have been calculated in the operating conditions of the long-term testing at 750°C, 12 Nml.cm<sup>-2</sup>.min<sup>-1</sup>, a current density of +/- 1 A.cm<sup>-2</sup> in SOFC and SOEC modes for a gas composition of p<sub>H<sub>2</sub></sub>/p<sub>H<sub>2</sub>O</sub> = 0.9/0.1 and p<sub>H<sub>2</sub></sub>/p<sub>H<sub>2</sub>O</sub> = 0.1/0.9, respectively. For this purpose, the concentrations of oxygen vacancies in the double layer at the Ni/YSZ interface have been calculated with equation 4-1 using the local overpotentials calculated as a function of the electrode thickness thanks to the electrochemical model. To relate the impact of these evolutions to the Ni wettability onto YSZ, it has been assumed that the Ni is detached from YSZ when the concentration of vacancies in the double layer reaches  $C_{V\ddot{O}}^{max}$ . This condition,  $C_{V\ddot{O}}^{int} = C_{V\ddot{O}}^{max}$ , means that all the oxygen atoms have been removed from the electrolyte interface, and hence, the contact angle  $\theta_{Ni/YSZ}$  is equal to  $\theta_{Ni/YSZ}^{max} = 180^\circ$ . At equilibrium when the concentration of vacancies is equal to  $C_{V\ddot{O}}^{int} = C_{V\ddot{O}}^{bulk}$ , the contact angle  $\theta_{Ni/YSZ}^{eq}$  can be expressed as a function of the local oxygen partial pressure as follows [7]:

$$\theta_{Ni/YSZ}^{eq} = \cos^{-1} \left( \frac{W_{adh}}{\gamma^p - \Gamma_O RT \ln \left( 1 + K_a \left( 2.38 \times 10^{-4} \left( \frac{p_{O_2}^{eq}}{p} \right)^{0.5} \exp \left( \frac{1.82 \times 10^5}{RT} \right) \right) \right)} - 1 \right) \quad 4-4$$

Where  $W_{adh}$  is the work of adhesion at the Ni/YSZ interface,  $\gamma^p$  the surface tension of pure Ni without oxygen adsorption,  $\Gamma_O$  is the saturation coverage of oxygen adsorption on Ni surface and  $K_a$  is the oxygen adsorption coefficient. The terms  $R$  and  $p$  denote the ideal gas constant and the atmospheric pressure. The oxygen partial pressure at equilibrium  $p_{O_2}^{eq}$  has been taken at the top of the active layer ( $z = \ell$ ) where the overpotentials tend to zero. It has been calculated with the hydrogen and steam partial pressures assuming that the hydrogen combustion reaction at 750°C (i.e.  $1/2O_2 + H_2 \leftrightarrow H_2O$ ) is at the thermodynamic equilibrium [8]:

$$p_{O_2}^{eq} = \left( \frac{p_{H_2O}^{eq}}{p_{H_2}^{eq} \exp \left( \frac{-\Delta G}{RT} \right)} \right)^2 \quad 4-5$$

Where the variation in Gibbs energy is given by [9] :

$$\Delta G = -248300 + 55.7 \times T \text{ [J/mol]} \quad 4-6$$

The contact angles at equilibrium can thus be calculated combining equations 4-7, 4-8 and 4-9 and using the input data listed in table 4-1. Finally, a semi-empirical approach has been adopted to express the contact angle. Indeed, it is worth noting that the contact angles under polarization have been computed as a function of the oxygen vacancies assuming a linear dependence between the two bounds  $\theta_{Ni/YSZ}^{eq} = f(C_{V\ddot{o}}^{bulk})$  and  $\theta_{Ni/YSZ}^{max} = f(C_{V\ddot{o}}^{max})$ .

**Table 4-1: Data used to calculate the Ni/YSZ contact angle at equilibrium.**

Parameters	Values
$W_{adh}$	1.4 [J.m <sup>-2</sup> ] [7]
R	8.314 [J.K <sup>-1</sup> .mol <sup>-1</sup> ]
T	1023 [K]
$\Gamma_o$	0.41 [N.m <sup>-1</sup> ] [7]
$K_a$	1200 [7]
$\gamma^p$	$1829 - 0.4014(T - 1728)$ [10 <sup>-3</sup> N.m <sup>-1</sup> ] [8]

### 4.3 Phase-field modeling

Modeling can be an efficient tool to unravel the complex and entangled phenomena involved in the Ni microstructural evolutions in the cermet. Many models have been already proposed to simulate accurately the morphological evolution of the Ni. First, the simulation of the Ni agglomeration, which is a well-known mechanism, has been modeling using semi-phenomenological approaches such as power-law models. They have been applied to calculate the growth of the mean Ni particle diameter upon operation [10]. Moreover, more sophisticated models have been also developed thanks to a detailed mechanistic description of the Ni coarsening phenomenon [11]. In this frame, the phase-field method has been successfully applied to reproduce accurately the Ni agglomeration in the electrode 3D microstructure [12] [13] [14]. The phase-field method is a computational method to describe the microstructure evolution of a material with space and time. In this approach, each phase is represented by a field variable, which has a constant value inside a phase while it varies smoothly at the interface defined by a finite thickness. The field variable includes the boundary information avoiding tracing the interface during the calculation. A detailed description of the governing equations for the phase-field theory is reported in appendix A. From the work of Cahn-Hilliard [15], the expression of the free energy functional as a function of the field variable and its spatial derivatives has been proposed. In the case of the Ni migration, only few models were

dedicated to the simulation of the Ni migration using the phase-field approach [16] [17]. In the work of [16], the model was based on the mechanism proposed by Trini et al. [18] while the electrode overpotentials were estimated using a Butler-Volmer expression for the electrochemical reaction at TPB. However, using this mechanism (cf. chapter 1 page 16), the wettability gradients are not sufficient to induce a significant migration even in SOEC mode. Moreover, Cheng et al. have proposed a mechanism based on the Ni reoxidation into NiO to explain the Ni redistribution [19]. A phase-field model has been developed in order to take into account the effect of the oxygen partial pressure variation on the microstructure evolution. It has been proposed that, close to the electrolyte interface in the YSZ phase, the oxygen partial pressure could be significant to trigger Ni oxidation and lead to Ni depletion. However, according to the author, further investigations are needed to confirm the hypothesis and the results. In this work, the phase field method was also applied to simulate the Ni redistribution due to a change of the Ni/YSZ interfacial energy according to the mechanism previously presented. For application to the Ni migration, the phase-field model has been implemented in a finite element code using the mathematic toolbox of COMSOL® [20]. To simulate the Ni evolution in the electrode 3D microstructure, the YSZ backbone is assumed to remain stable upon operation which implies a rather negligible mobility [18]. Therefore, the evolution of the YSZ is no longer taken into account in the model. The assumption made on the YSZ allows simulating the evolution of three-phase system with only one phase-field variable. Indeed, the phase-field variable is equal to the constant value of 0 in the bulk of the porosity and 1 in the bulk of the Ni phase while it varies smoothly with values between ]0,1[ at the interface which is defined by a finite thickness. The gradient in Ni/YSZ contact angle is imposed as boundary conditions in the three-phase system. Indeed, the contact angle between Ni and YSZ contains information about the surface energies of the three phases and is the driving force of the dynamic evolution of Ni. In this work, the implementation of the gradient in contact angle boundary conditions is carried out assuming that the phases of the system (Ni, YSZ, and pores) satisfy to the well-known Young's equation. The system describes the evolution of the Ni/gas interface where the phase field variable  $\phi$  corresponds to the Ni concentration. The free energy function describing the total energy of the system is then introduced (cf. appendix for the phase field fundamentals):

$$F[\phi]=\int_v[wg(\phi) + \frac{\epsilon^2}{2}|\nabla\phi|^2] dv \quad 4-10$$

Where the integral term  $wg(\phi)$  represents the free energy of the system. The term  $w$  is the height of the energy barrier for the transition from one phase to another (transition from 0 to 1) while  $g(\phi)$  is a

double-well function of the following form  $g(\phi) = \phi^2(1 - \phi)^2$ . The second term  $\frac{\varepsilon^2}{2} |\nabla\phi|^2$  depends on the gradient coefficient  $\varepsilon$  and is used to describe the interface continuously by taking values between  $]0,1[$ .

The stationary profile of the phase field is obtained by minimizing the free energy to reach equilibrium. It is expressed as follows (Figure 4-5):

$$\phi(x) = \frac{1}{2} + \frac{1}{2} \tanh\left(\frac{2x}{\delta}\right) \quad 4-11$$

By solving the stationary profile, the half-thickness expression of the phase field interface is introduced:

$$\delta = \frac{4\varepsilon}{\sqrt{2w}} \quad 4-12$$

In the finite element mesh, it is worth noting that the half thickness of the phase field,  $\delta$ , needs to contain a sufficient number of elements in order to correctly describe the smooth interface. For this study, this value is taken equal to 3 times the size of a mesh element in order to well describe the interface. A final characteristic parameter of the system is the interface energy between Ni and porosity and is expressed as a function of  $w$  and  $\varepsilon$ :

$$\sigma = \frac{\varepsilon\sqrt{2w}}{6} \quad 4-13$$

In this work, the interface energy between the Ni and the pores,  $\sigma$ , is a physical value taken equal to 1.92 J/m<sup>2</sup> [21]. The governing equation involves the parameters  $w$  and  $\varepsilon$ , which are numerical and difficult to identify in the literature. In this work, the half thickness of the phase field interface was fixed to 0.3  $\mu\text{m}$ . The values for  $w$  and  $\varepsilon$  are then deduced from equations 4-9 and 4-10.

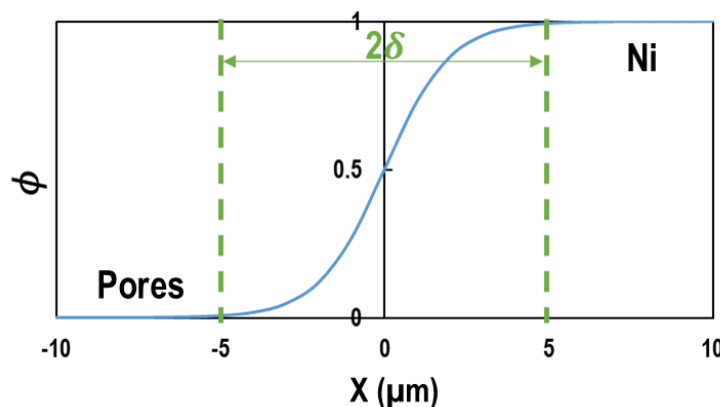


Figure 4-5: Stationary profile of the phase field variable at the Ni/pore interface as a function of the distance  $x$  in  $\mu\text{m}$  for example.

The redistribution of the Ni phase in the electrode microstructure implies that the quantity of Ni in the volume remains constant. It is worth noting that the chemical potential is defined as follows:

$$\mu = \frac{\delta F[\phi]}{\delta \phi} \quad 4-14$$

According to Fick's law:

$$\vec{j} = -M\nabla\mu \quad 4-15$$

$M$  (en  $\text{m}^5\cdot\text{J}^{-1}\cdot\text{s}^{-1}$ ) represents the mobility and is expressed physically as:

$$M = \frac{D Vm}{R T} \quad 4-16$$

With  $D$  the diffusion coefficient of Ni ( $\text{m}^2\cdot\text{s}^{-1}$ ),  $Vm$  the molar volume of Ni ( $6.59 \times 10^{-6} \text{ m}^3\cdot\text{mol}^{-1}$ ),  $R$  the constant of the ideal gases ( $8.314 \text{ J}\cdot\text{mol}^{-1}\cdot\text{K}^{-1}$ ) and  $T$  (K) the temperature. In the phase-field approach, the mobility is a key parameter that has an impact on the speed of Ni diffusion. In this work, the mobility is expressed as a function of  $\phi$ , defined as follows Figure 4-6:

$$M(\phi) = A \phi^2(1 - \phi)^2 \quad 4-17$$

With  $A = \frac{M1}{0.5^2(1-0.5)^2}$  and  $M1 = \frac{D Vm}{R T}$ . With this definition, the mobility is maximal at the Ni/gas interface (i.e  $\phi = 0.5$ ) and equal to 0 in the bulk phases Figure 4-6. For the simulation, it can be noted the Ni can diffuse on the surface or in the bulk of the Ni particles, then the diffusion coefficient,  $D$ , for the Ni was taken equal to  $10^{-14} \text{ m}^2/\text{s}$ , which is an average value between the surface diffusion ( $D=10^{-12} \text{ m}^2\cdot\text{s}^{-1}$ ) and volume diffusion ( $D =10^{-16} \text{ m}^2\cdot\text{s}^{-1}$ ) coefficients [22] [23].

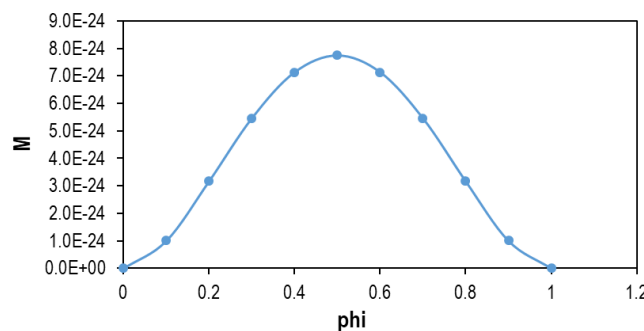


Figure 4-6: Evolution of the mobility  $M(\phi)$  as a function of the phase-field variable  $\phi$ .

The mass conservation implies:

$$\frac{d\phi}{dt} = -\nabla \vec{J} \quad 4-18$$

Therefore, the spatial and temporal evolution of Ni through the phase field variable  $\phi$  is controlled by the so-called Cahn-Hilliard equation which is used as the governing equation (cf. *Appendix 1*):

$$\frac{d\phi}{dt} = \nabla \cdot \left( M \nabla \frac{\delta F[\phi]}{\delta \phi} \right) = \nabla \cdot (M \nabla (2w\phi(1-\phi)(1-2\phi) - \varepsilon^2 |\nabla^2 \phi|)) \quad 4-19$$

### 4.3.1 Validation of the numerical implementation

The validation of the phase field numerical implementation is the first step to be sure about the reliability of the model to predict the evolution of the complex 3D microstructure. First, this validation has been done on a simplified case, which consists of a cubic particle of Ni deposited on a YSZ substrate (Figure 4-7). This cubic particle is expected to evolve towards a spherical droplet by minimizing its surface energy. It must also move under the application of a gradient of contact angle. The geometry chosen was a cube of  $0.5 \times 0.5 \times 0.5 \mu\text{m}^3$  put down on a planar surface with a mesh composed of tetrahedral elements with a constant edge length of  $0.045 \mu\text{m}$ .

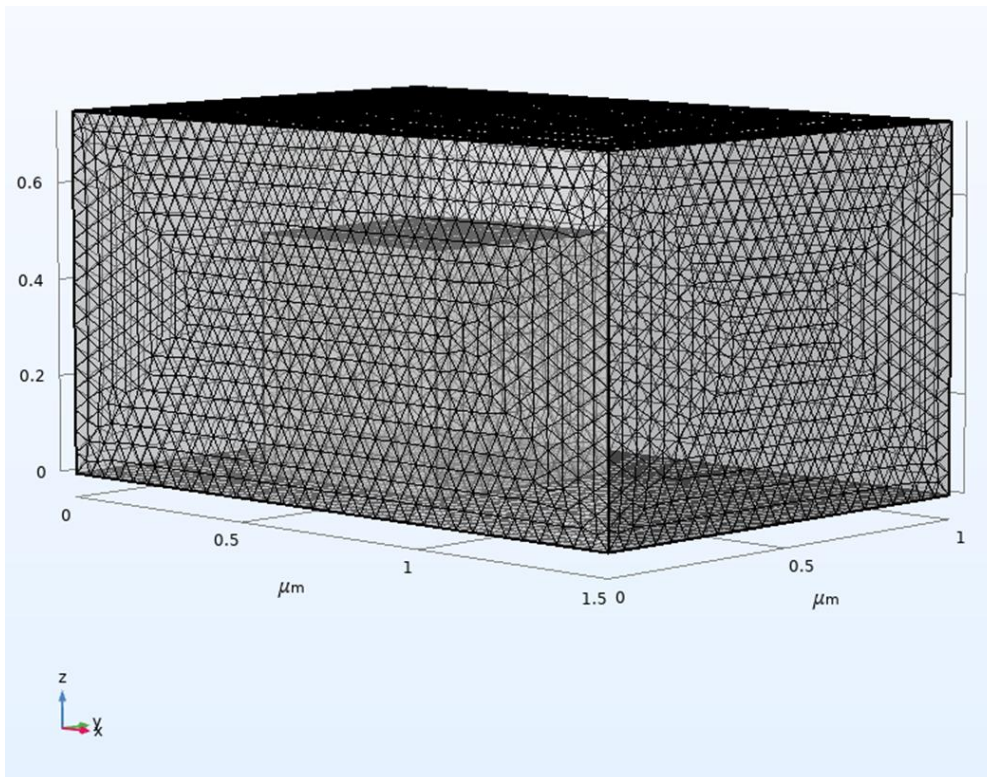


Figure 4-7: Mesh of the 3D geometry used for the validation of the phase-field model (*the small cube inside parallelepiped is the initial Ni particle enclosed in the gas phase (i.e. air for the parallelepiped)*).

It is worth noting that the validation has been done using a constant factor of mobility  $M$  in order to simplify the governing equation that has to be solved and consequently decrease the computation time. In order to check the validity of the model, the value of the contact angle of the particle with the planar surface has been taken down as a function of the position according to the values of the imposed gradient of contact angle. The Figure 4-8 presents the results of the simulation after 10000s under the application of a gradient in contact angle for a window of 1.5  $\mu\text{m}$ . First, it can be seen that the particle evolves towards a spherical shape in order to minimize its energy. Moreover, the angle formed between the Ni particle and the YSZ substrate corresponds to the imposed value in the simulation. After the minimization, the particle moves in the direction of the lower value of contact angle (toward the position of 1.5  $\mu\text{m}$ ). Based on these results, the numerical implementation was considered validated.

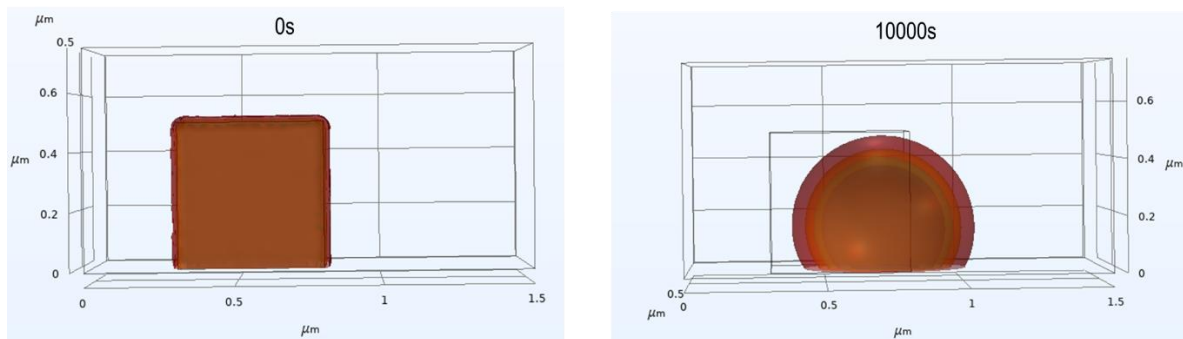


Figure 4-8: Evolution from an initial to a final state (after 10000s) of a particle under the application of a gradient in contact angle between the particle and the substrate for a window of 1.5  $\mu\text{m}$ .

## 4.4 Elements of validation for the mechanism

### 4.4.1 Gradients of Ni/YSZ contact angle

The determination of the Ni/YSZ contact angles was performed with the method detailed in 4.2.2 using the multi-scale electrochemical model. First, the complete cell model has been used to plot the local current densities along the cell radius in the conditions of the experimental durability tests (at 750°C, 12 Nml.cm<sup>-2</sup>.min<sup>-1</sup>, a total current density of +/- 1 A.cm<sup>-2</sup> in SOFC and SOEC modes for a gas composition of p<sub>H<sub>2</sub></sub>/p<sub>H<sub>2</sub>O</sub> = 0.9/0.1 and p<sub>H<sub>2</sub></sub>/p<sub>H<sub>2</sub>O</sub> = 0.1/0.9 respectively) (cf. section 3.1). Due to the steam consumption and the hydrogen production, the local current density decreases continuously from the gas inlet to the outlet [1]. It is worth noting that the cermet reconstructions after the tests have been done at a radial position of 0.7 cm from the cell center (i.e. gas inlet). According to Figure 4-9, this position corresponds to a local current density equal to 1.08 A.cm<sup>-2</sup> in SOFC mode whereas it is equal to -1.23 A.cm<sup>-2</sup> in SOEC mode. Moreover, the gas composition taken at the interface between the active layer and

the cermet support is given equal to  $p_{H_2}/p_{H_2O}=0.28/0.72$  in SOEC mode and  $p_{H_2}/p_{H_2O}=0.73/0.27$  in SOFC mode by the model.

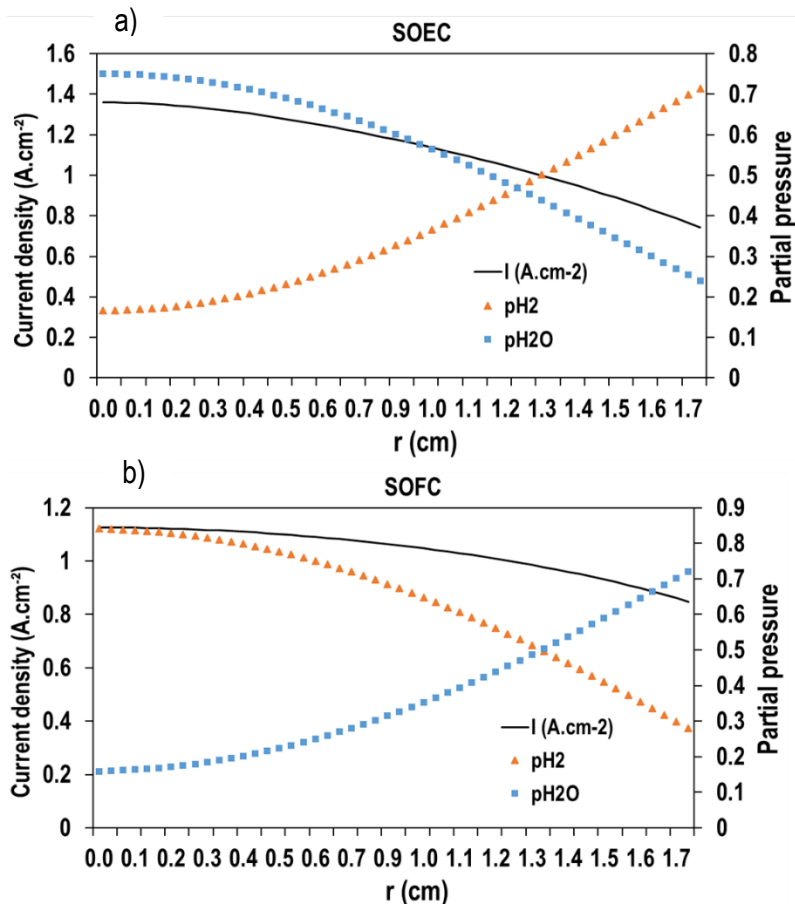


Figure 4-9: Distribution of the current density and the p<sub>H<sub>2</sub></sub> and p<sub>H<sub>2</sub>O</sub> along the cell radius r at 750°C, 12 Nml.cm<sup>-2</sup>.min<sup>-1</sup>, +/- 1 A.cm<sup>-2</sup> for a gas composition of p<sub>H<sub>2</sub></sub>/p<sub>H<sub>2</sub>O</sub> = 0.9/0.1 and p<sub>H<sub>2</sub></sub>/p<sub>H<sub>2</sub>O</sub> = 0.1/0.9 respectively (b) in SOFC and (a) SOEC modes.

The local conditions of partial pressures and current density along the cell radius are the boundary conditions that need to be applied in the hydrogen electrode model. Using these boundary conditions, the electrode model allows to determine the distribution of the overpotential as a function of the electrode thickness in the two operating modes Figure 4-10.

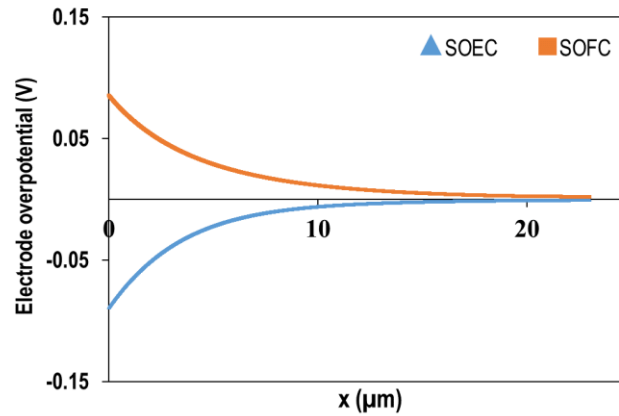


Figure 4-10: Evolution of the electrode overpotential in SOEC and SOFC modes as a function of the electrode thickness for the local conditions corresponding to a radial position of 0.7 cm from the cell center (750°C, 12 Nml.cm<sup>-2</sup>.min<sup>-1</sup>, p<sub>H<sub>2</sub></sub>/p<sub>H<sub>2</sub>O</sub>=0.28/0.72 in SOEC mode and p<sub>H<sub>2</sub></sub>/p<sub>H<sub>2</sub>O</sub>=0.73/0.27 in SOFC mode).

Once the local overpotentials are known, the distribution of the concentration of oxygen vacancies in the double layer between the Ni and the YSZ can be estimated according to equation 1.1 as a function of the electrode thickness. This evolution is plotted in Figure 4-11 a) A strong difference in concentration can be observed between both modes. In SOEC mode, at the interface with the electrolyte (corresponding to  $x = 0 \mu\text{m}$ ), the concentration in oxygen vacancies is high and decreases steeply down to the equilibrium value towards the interface between the functional layer and the support. On the contrary, the SOFC mode presents a low gradient as the oxygen vacancies concentration increases slightly from the electrolyte interface in the thickness of the functional layer. As explained in section 1.2.2, it is supposed that there is a linear evolution between the contact angle and the oxygen vacancies concentration.

From the linear dependence of Ni/YSZ contact angle with the concentration of oxygen vacancies between  $\theta_{Ni/YSZ}^{eq} = f(C_{V_o}^{bulk})$  and  $\theta_{Ni/YSZ}^{max} = f(C_{V_o}^{max})$ , the contact angle evolution with the electrode thickness is shown in Figure 4-11 b) for both SOEC and SOFC operating conditions (i.e. the two different conditions of oxygen partial pressure at equilibrium). A steep decrease of the Ni/YSZ contact angle from the electrolyte interface is found in SOEC mode leading to a high gradient in wettability ( $\approx 16^\circ$  for the first 23  $\mu\text{m}$  below the electrolyte interface). This gradient should thus trigger a substantial Ni migration away from the electrolyte interface. On the contrary, only a slight increase in the contact angle is calculated from the electrolyte interface in SOFC mode. It is associated to a low gradient in wettability ( $\approx -3^\circ$  for the first 23  $\mu\text{m}$  below the electrolyte interface) that should drive a slow Ni migration towards the electrolyte interface.

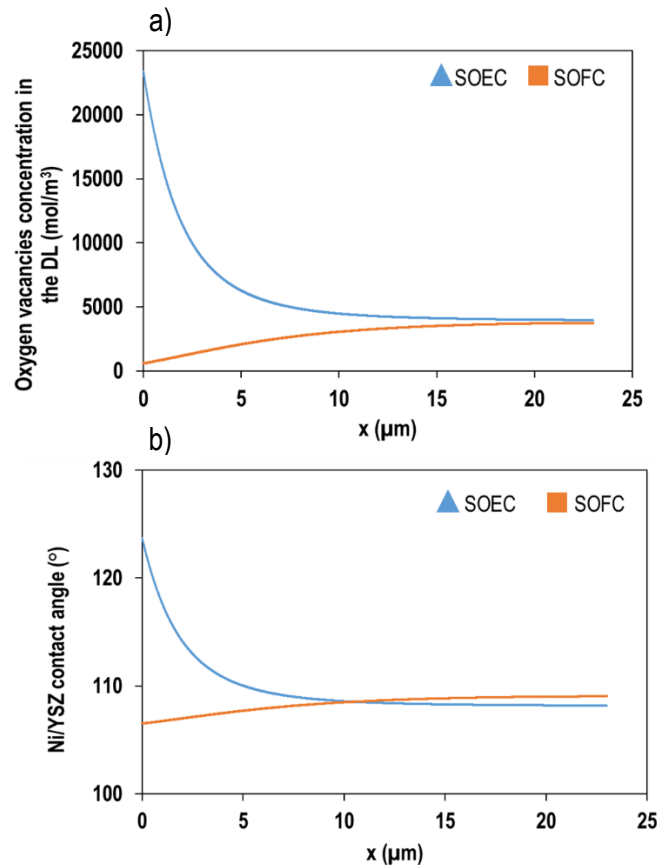


Figure 4-11: a) Evolution of the concentration of the oxygen vacancies in the double layer and b) evolution of the contact angle between the Ni and YSZ as a function of the electrode thickness at  $750^\circ\text{C}$ ,  $12 \text{ Nml}\cdot\text{cm}^{-2}\cdot\text{min}^{-1}$ ,  $\pm 1 \text{ A}\cdot\text{cm}^{-2}$  for a gas composition of  $\text{pH}_2/\text{pH}_2\text{O} = 0.9/0.1$  and  $\text{pH}_2/\text{pH}_2\text{O} = 0.1/0.9$  in SOFC and SOEC modes respectively. DL = double layer.

#### 4.4.2 Properties

The phase-field simulations were carried out separately for operations of 2000h in SOEC and SOFC modes at  $i = \pm 1 \text{ A}\cdot\text{cm}^{-2}$ ,  $\text{pH}_2/\text{pH}_2\text{O} = 0.1/0.9$  and  $\text{pH}_2/\text{pH}_2\text{O} = 0.9/0.1$  respectively,  $12 \text{ Nml}\cdot\text{cm}^{-2}\cdot\text{min}^{-1}$  and  $750^\circ\text{C}$ . For a relevant comparison, it should be noted that simulations were performed under the same conditions as experiments. The phase-field computations in SOEC and SOFC modes were performed with the Ni/YSZ contact angle gradients reported in Figure 4-11 b). A volume of the electrode microstructure, including a part of the electrolyte, was taken as initial state to well describe the local heterogeneities especially in the electrode thickness. Indeed, the phase field model presented above has been applied to a real 3D microstructure obtained from FIB-SEM reconstruction of the reference cell. The Figure 4-12 presents the mesh realized with the Avizo software used for the simulation. A volume with a size of  $4 \times 4 \times 6 \mu\text{m}^3$  was considered for a mesh size of 100 nm. For the 3D meshed microstructure, it was important to find a good compromise between a fine mesh to increase the accuracy of the results

and a coarser mesh to reduce the cost of the calculation and thus carry out the simulations in a reasonable time.

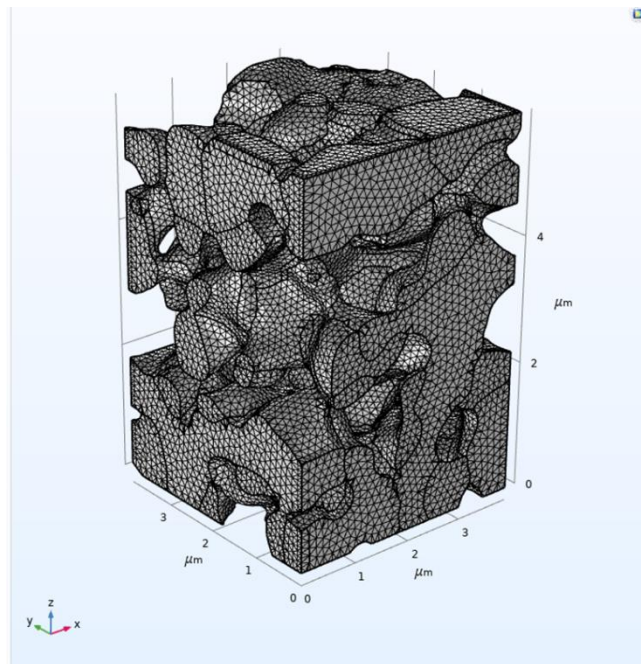


Figure 4-12: Mesh of the  $4 \times 4 \times 6 \mu\text{m}$  volume with a typical mesh size of 100 nm.

The 3D microstructure of the Ni-YSZ electrode is shown in Figure 4-13 a) for the initial state whereas the ones simulated by the phase-field model are displayed in Figure 4-13 b) and c) for the ageing in electrolysis mode and Figure 4-13 d) and e) for the ageing in fuel cell mode at respectively 1000h and 2000h. Moreover, for the sake of clarity, the Figure 4-14 presents the 3D rendering volumes with only the Ni phase for 1000h and 2000h in both operating modes. From the visual inspection of the Ni skeleton after operation, it is clear that, in both cases, the Ni has become strongly agglomerated. The table 4-2 presents the evolution of the active TPB length density and mean diameter ( $d_{\text{meanNi}}$ ) of the Ni in SOEC and SOFC after 1000h and 2000h of ageing. Indeed, the Ni agglomeration is confirmed by the increase of the  $d_{\text{meanNi}}$  from  $0.648 \mu\text{m}$  to  $0.728 \mu\text{m}$  and  $0.744 \mu\text{m}$  respectively in SOEC and SOFC modes. Moreover, it is also confirmed by the decrease of the active TPB length density from  $1.9446 \mu\text{m}^{-2}$  to  $0.868 \mu\text{m}^{-2}$  in electrolysis mode and  $0.9189 \mu\text{m}^{-2}$  in fuel cell mode. As expected, the decrease is higher in SOEC mode and it could be associated to the Ni redistribution in the electrode thickness. Indeed, for the volume aged in SOEC mode, it is possible to observe the Ni migration away from the electrolyte interface in Figure 4-13 b) c) compared to the reference one. The Ni, which was present at the interface, has moved away whereas it is still present in the microstructure aged in SOFC mode in Figure 4-13 d) e).

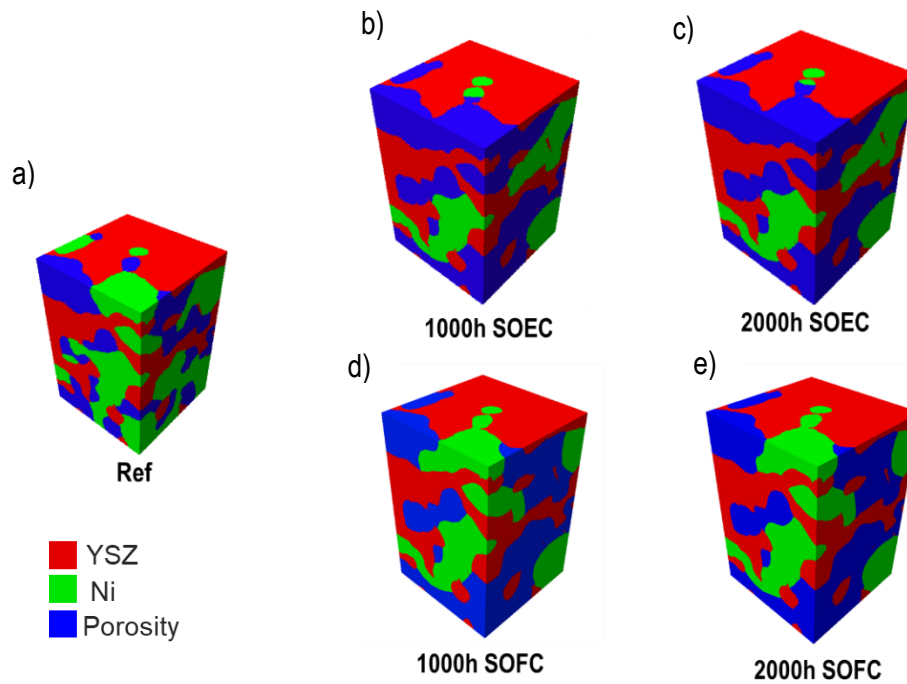


Figure 4-13: Evolution of the volumes in b),c) SOEC ( $-1 \text{ A.cm}^{-2}$ ,  $\text{pH}_2/\text{pH}_2\text{O} = 0.1/0.9$ ,  $12 \text{ Nml.cm}^{-2}.\text{min}^{-1}$  and  $750^\circ\text{C}$  and d),e) SOFC ( $1 \text{ A.cm}^{-2}$ ,  $\text{pH}_2/\text{pH}_2\text{O} = 0.9/0.1$ ,  $12 \text{ Nml.cm}^{-2}.\text{min}^{-1}$  and  $750^\circ\text{C}$ ) after respectively 1000h (b) and d)) and 2000h (c) and e)) of simulation with the Ni/YSZ contact angle gradients calculated in Figure 4-11 b) and compared to a) the reference. The electrolyte is located at the top.

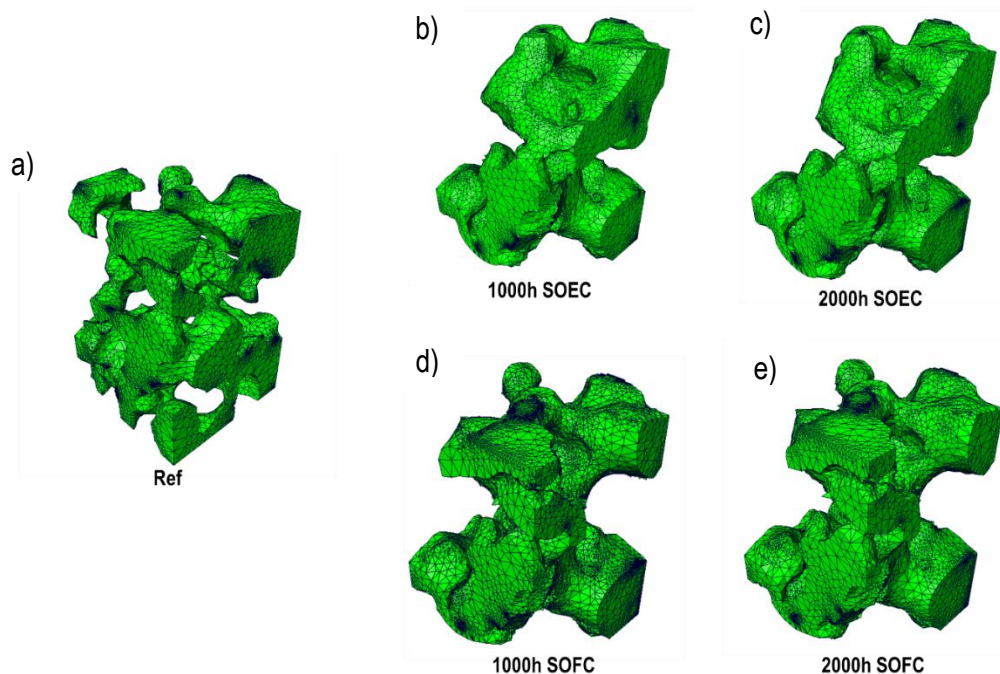


Figure 4-14: 3D microstructures of the Ni phase only for a) the reference, b),c) SOEC ( $-1 \text{ A.cm}^{-2}$ ,  $\text{pH}_2/\text{pH}_2\text{O} = 0.1/0.9$ ,  $12 \text{ Nml.cm}^{-2}.\text{min}^{-1}$  and  $750^\circ\text{C}$ ) and c), d) SOFC ( $1 \text{ A.cm}^{-2}$ ,  $\text{pH}_2/\text{pH}_2\text{O} = 0.9/0.1$ ,  $12 \text{ Nml.cm}^{-2}.\text{min}^{-1}$  and  $750^\circ\text{C}$ ), with the Ni/YSZ contact angle gradients calculated in Figure 4-11 b) after respectively 1000h (b) and d)) and 2000h (c) and e)) of simulation. The electrolyte is located at the top.

**Table 4-2: Values of the active TPB density and Ni mean diameter in SOEC and SOFC compared to the reference ones.**

	Time	Active TPB density ( $\mu\text{m}^{-2}$ )	Ni mean diameter ( $\mu\text{m}$ )
Ref	0h	1.94	0.65
SOEC	1000h	0.87	0.73
	2000h	0.87	0.738
SOFC	1000h	0.91	0.74
	2000h	0.92	0.75

The time evolution of the mass center position for Ni obtained during operation in SOEC and SOFC mode are plotted in Figure 4-15. First, it can be noticed that the Ni agglomeration induce a rapid evolution over the first 700h in both modes. For ageing in SOEC mode, it is found that the Ni moves towards the top of the electrode functional layer whereas it is stabilized in SOFC mode after 2000h of simulated time. Therefore, as expected, a noticeable Ni migration away from the electrolyte interface is calculated after 2000h of simulation in SOEC mode whereas no Ni migration is detected from the position of the mass center in SOFC mode after 2000h. This result points out that the gradient in contact angle estimated according to the proposed mechanism in SOEC mode is able to trigger a substantial Ni redistribution away from the electrolyte interface for a time of simulation similar to the experimental one. Therefore, this simulation result is consistent with the post-mortem observations of the tested cell (evolution of 7% of the mass center position), which have revealed a strong Ni depletion at the electrolyte interface for the same operating conditions at 750°C and -1 A.cm<sup>-2</sup> (evolution of 5% of the mass center position). Moreover, the gradient of contact angle in SOFC mode is not able to drive a significant Ni redistribution in SOFC mode. According to these modeling results, the mechanism is able to predict a strong Ni redistribution under SOEC condition and a very slow Ni migration in SOFC mode that could be detected only after a very long-term durability experiment (> 5000h).

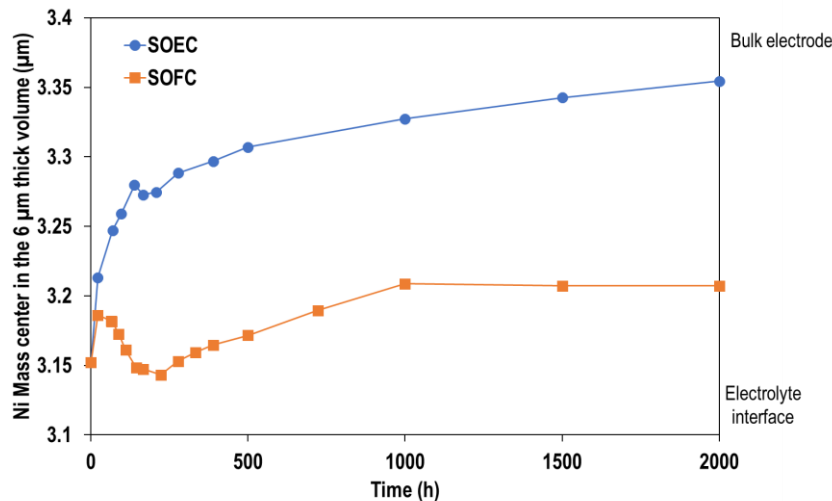


Figure 4-15: Evolution as a function of time of the mass center calculated over the electrode thickness for the Ni phase for an operation in SOEC ( $-1 \text{ A.cm}^{-2}$ ,  $p\text{H}_2/p\text{H}_2\text{O} = 0.1/0.9$ ,  $12 \text{ Nml.cm}^{-2}.\text{min}^{-1}$  and  $750^\circ\text{C}$ ) and SOFC ( $1 \text{ A.cm}^{-2}$ ,  $p\text{H}_2/p\text{H}_2\text{O} = 0.9/0.1$ ,  $12 \text{ Nml.cm}^{-2}.\text{min}^{-1}$  and  $750^\circ\text{C}$ ) with the Ni/YSZ contact angle gradients calculated in Figure 4-11 b).

To go further into the analysis and to explore in detail the Ni migration, the local variations of the phase volume fractions have been measured on the simulated microstructures. They are plotted in Figure 4-16 a) and b) for the SOEC and SOFC modes respectively as a function of the position in the electrode thickness (i.e. in the direction perpendicular to the electrolyte interface). This result confirms first that local rearrangements of Ni particles arise in the microstructure due to the coarsening of the initial inhomogeneous microstructure whatever the operating mode. The plots obtained for the simulated microstructures in SOEC mode at  $t = 1000 \text{ h}$  and  $2000 \text{ h}$  are compared to the reference one in Figure 4-16 a). It can be noticed that the Ni depleted zone extends from the electrolyte interface over a distance of around  $\approx 1.5 \mu\text{m}$  in the functional layer with a decrease from 0.3 to 0.1 of the Ni volume fraction at the electrolyte interface (slightly above  $0 \mu\text{m}$ ) between the reference and the SOEC ageing. It is followed by a second region in the electrode where the cermet is enriched by the Ni coming from the depleted zone (at about  $4\text{-}5 \mu\text{m}$  from the electrolyte interface). The extent of Ni depletion due to the migration in SOEC mode is roughly consistent with the experiments. Indeed, in the experimental condition, the depleted zone was found to spread over a distance of around  $2 \mu\text{m}$ . Besides, it can be speculated that the microstructural change due to the Ni migration can affect the electrochemical response by changing the repartition of the overpotentials in the electrode thickness (since a zone close to the electrolyte interface must become inactive due to the Ni loss). From this point of view, it would be necessary to improve the model with a staggered resolution integrating both electrochemical and phase-field simulations. In this case, the gradients of contact angle should be calculated at each time when a noticeable microstructure change is obtained with the phase-field model. Moreover, it cannot be fully excluded that Ni migration also occurs

in the gas phase resulting in a higher depleted zone. Nevertheless, Lei et al. [24] have found that the mechanism based on the  $\text{Ni}(\text{OH})_2$  gas diffusion is not sufficient to explain the Ni redistribution at  $800^\circ\text{C}$ . Finally, the profiles of Ni volume fraction obtained for an operation in SOFC mode are plotted in Figure 4-16 b). As foreseen after 2000h of operation in SOFC mode, there is no significant Ni redistribution in the electrode. The evolution is attributed to the Ni agglomeration in the microstructure. This statement confirms that the Ni enrichment can be observed only after a very long-term durability experiment. This behavior is due to the small gradient in the Ni/YSZ contact angle calculated in SOFC mode.

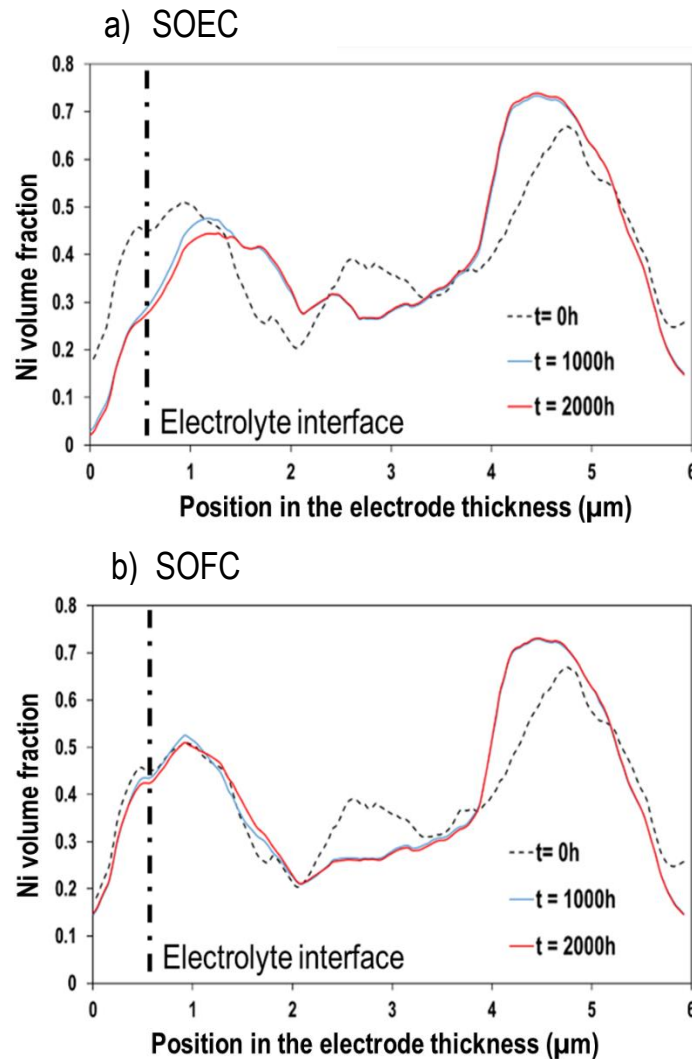


Figure 4-16: Phase fraction evolution of the Ni phase for the reference and after 1000h and 2000h of simulation in a) SOEC ( $-1 \text{ A}\cdot\text{cm}^{-2}$ ,  $p_{\text{H}_2}/p_{\text{H}_2\text{O}} = 0.1/0.9$ ,  $12 \text{ Nml}\cdot\text{cm}^{-2}\cdot\text{min}^{-1}$  and  $750^\circ\text{C}$ ) and b) SOFC ( $1 \text{ A}\cdot\text{cm}^{-2}$ ,  $p_{\text{H}_2}/p_{\text{H}_2\text{O}} = 0.9/0.1$ ,  $12 \text{ Nml}\cdot\text{cm}^{-2}\cdot\text{min}^{-1}$  and  $750^\circ\text{C}$ ) with the Ni/YSZ contact angle gradients calculated in Figure 4-11 b).

According to the phase-field model, Ni migrates from high to low contact angles in both SOEC and SOFC modes. Moreover, the rate of migration depends on the contact angle gradient, which means that higher contact angle gradient can cause a more significant Ni migration. Thanks to the proposed mechanism, a relatively high gradient in Ni wettability was calculated in SOEC mode, so that it is able to drive a significant

Ni depletion in this mode with the phase-field model. On the contrary, the gradient of contact angle estimated in SOFC mode was found to be insufficient to trigger a noticeable Ni redistribution.

Regarding typical porous electrodes, it appears that the mechanism is consistent with our experimental results and most of the ones reported in literature [18] [25] [6] [26]. Indeed, for cells operated in SOEC mode below 900°C, a large Ni depletion is usually observed at the electrolyte interface [18]. However, a reverse behavior has been observed at 950°C with a Ni relocation at the electrolyte interface. In this particular condition, it has been suggested that Ni can be transported in the gas phase with a Ni accumulation at the electrolyte interface [5]. On the other hand, in SOFC mode, no significant Ni redistribution is observed after operation. For instance, using the same type of cermet, Trini et al. [18] have detected a Ni migration only in SOEC mode and not under SOFC polarization. Nonetheless, few authors have found a Ni enrichment at the electrode interface after SOFC operation. Menzler et al. [6] have detected a slight Ni migration toward the electrolyte after an operation of 100,000 h. This microstructural evolution could be still compatible with the low wettability gradient estimated in this work. However, Parikh [28] observed a substantial Ni enrichment for an operation at 800°C, 860°C and 925°C after 8000 h. In this case, the low wettability gradients calculated with the model could failed to explain this experimental result. Regarding patterned nickel-film electrode, Jiao et al. [7] observed a Ni detachment in SOEC mode, which is consistent with the interface weakening due to the accumulation of oxygen vacancies in the double layer. Under fuel cell polarization, they observed a higher wettability of Ni onto YSZ. Even though this evolution is coherent with the change of Ni/YSZ interface energy due to the change in oxygen vacancy concentration, it is expected to be very limited in this case. Therefore, it could be explained by another modification of the Ni/YSZ interface, which remains nowadays unclear (segregation of impurities, etc...). In other words, the change of the Ni/YSZ interfacial energy, which has been attributed to a modification of the electrochemical double layer, could be also induced by other physico-chemical processes controlled by the electrode polarization.

Aside from the mechanism based on wettability gradient, it has been proposed in [29] that the detached Ni particles, which are no longer polarized, could migrate via  $\text{Ni}(\text{OH})_x$  surface or gas species depending on the temperature. This mechanism is well consistent with the experiment of Jiao et al. [30] However, as pointed out by Lei et al [17] this hypothesis 'is unlikely to explain those experiments in fuel cell mode which report Ni enrichment near the electrolyte layer' as it 'relies on a significant loss of contact between Ni particles and between Ni and YSZ. Moreover, this mechanism does not explain the Ni migration observed under dry  $\text{CO}_2$  analysis [31] [32] Therefore, it can be suspected that both mechanisms could coexist in order to explain all the experiments results. One of the two could become predominant depending on the operating conditions, the cermet microstructure and/or the properties of the Ni/YSZ interface (e.g. interfacial energy depending on impurities at interface).

From this discussion, it appears that the underlying mechanisms for Ni migration are complex and involve several processes depending on the experimental conditions or tested cermet. Even if modeling results of this work seem consistent with most of the experimental results conducted on porous cermet, further simulations, experiments and post-test characterizations are still required to validate the mechanism proposed in this thesis. Therefore, it is clear that additional investigations are still needed to clarify the mechanism of Ni migration by taking into consideration other phenomena such as the segregation of impurities under polarization for instance.

## 4.5 Conclusion

This chapter was dedicated to the simulation of the Ni migration with a phase-field model developed in this work. The proposed mechanism to account for the Ni migration is based on the impact of the electrode overpotential and the oxygen vacancies in the electrochemical double layer on the Ni wettability onto YSZ. This mechanism yields gradients in Ni/YSZ contact angle that drive a Ni migration from low wettability to high wettability regions (i.e. from high to low Ni/YSZ contact angles).

In this work, the multi-scale electrochemical model has been used to assess the local electrode overpotentials in the electrode thickness and to calculate the gradients of Ni/YSZ contact angle in the same conditions than the experiments. These gradients together with the reconstruction of the pristine electrode were used as input data in the phase-field model. Indeed, a phase-field model has been developed and validated to simulate accurately the Ni redistribution in the electrode in SOEC ( $-1 \text{ A.cm}^{-2}$ ,  $p\text{H}_2/p\text{H}_2\text{O} = 0.1/0.9$ ,  $12 \text{ Nml.cm}^{-2}.\text{min}^{-1}$  and  $750^\circ\text{C}$ ) and in SOFC ( $1 \text{ A.cm}^{-2}$ ,  $p\text{H}_2/p\text{H}_2\text{O} = 0.9/0.1$ ,  $12 \text{ Nml.cm}^{-2}.\text{min}^{-1}$  and  $750^\circ\text{C}$ ). The simulations have shown that a substantial Ni depletion occurs after an operation of 2000h in SOEC mode. Moreover, the simulated depleted zone has been found in the same range of magnitude than the experimental one (albeit lower). To complement the modeling results, simulations have been performed in reverse conditions in SOFC mode. In this case, only a negligible Ni redistribution with no visible Ni enrichment at the electrolyte interface has been found. The simulations based on the implemented mechanism are thus consistent with the observations of the cells aged in SOEC and SOFC modes. They are also coherent with the experimental studies, which have reported a substantial Ni depletion in SOEC mode after a rather short time of ageing and a very moderate enrichment in SOFC mode after a long time of ageing. However, the mechanism still needs to be fully validated. From, this point of view, further experimental and modeling investigations are still required to better understand the complex underlying mechanism controlling the Ni migration.

## Bibliography of the chapter 4

- [1] E. Da Rosa Silva, M. Hubert, B. Morel, H. Moussaoui, J. Debayle, and J. Laurencin, 'A Dynamic Multi-Scale Model for Solid Oxide Cells Validated on Local Current Measurements: Impact of Global Cell Operation on the Electrodes Reaction Mechanisms', *ECS Trans.*, vol. 103, no. 1, pp. 893–907, Jul. 2021, doi: 10.1149/10301.0893ecst.
- [2] G. Sassone, E. Da Rosa Silva, M. Prioux, M. Hubert, B. Morel, A. Léon and J. Laurencin, 'Multiscale Modelling of Solid Oxide Cells Validated on Electrochemical Impedance Spectra and Polarization Curves', *ECS Trans.*, vol. 111, no. 6, pp. 649–661, May 2023, doi: 10.1149/11106.0649ecst.
- [3] M. G. H. M. Hendriks, J. E. ten Elshof, H. J. M. Bouwmeester, and H. Verweij, 'The defect structure of the double layer in yttria-stabilised zirconia', *Solid State Ion.*, vol. 154–155, pp. 467–472, Dec. 2002, doi: 10.1016/S0167-2738(02)00484-8.
- [4] O. A. Marina, L. R. Pederson, M. C. Williams, G. W. Coffey, K. D. Meinhardt, C. D. Nguyen and E. C. Thomsen, 'Electrode Performance in Reversible Solid Oxide Fuel Cells', *J. Electrochem. Soc.*, vol. 154, no. 5, p. B452, 2007, doi: 10.1149/1.2710209.
- [5] T. Sasaki, K. Matsunaga, H. Ohta, H. Hosono, T. Yamamoto, and Y. Ikuhara, 'Atomic and Electronic Structures of Ni/YSZ(111) Interface', *Mater. Trans.*, vol. 45, no. 7, pp. 2137–2143, 2004, doi: 10.2320/matertrans.45.2137.
- [6] N. H. Menzler, D. Sebold, Y. J. Sohn, and S. Zischke, 'Post-test characterization of a solid oxide fuel cell after more than 10 years of stack testing', *J. Power Sources*, vol. 478, p. 228770, Dec. 2020, doi: 10.1016/j.jpowsour.2020.228770.
- [7] Z. Jiao and N. Shikazono, 'Study on the effects of polarization on local morphological change of nickel at active three-phase-boundary using patterned nickel-film electrode in solid oxide fuel cell anode', *Acta Mater.*, vol. 135, pp. 124–131, Aug. 2017, doi: 10.1016/j.actamat.2017.05.051.
- [8] S. Ozawa, S. Takahashi, N. Watanabe, and H. Fukuyama, 'Influence of Oxygen Adsorption on Surface Tension of Molten Nickel Measured Under Reducing Gas Atmosphere', *Int. J. Thermophys.*, vol. 35, no. 9–10, pp. 1705–1711, Oct. 2014, doi: 10.1007/s10765-014-1674-5.
- [9] L. Bernadet, 'Étude de l'effet de la pression sur l'électrolyse de H<sub>2</sub>O et la co-électrolyse de H<sub>2</sub>O et CO<sub>2</sub> à haute température', p. 239.
- [10] M. Hubert, J. Laurencin, P. Cloetens, B. Morel, D. Montinaro, and F. Lefebvre-Joud, 'Impact of Nickel agglomeration on Solid Oxide Cell operated in fuel cell and electrolysis modes', *J. Power Sources*, vol. 397, pp. 240–251, Sep. 2018, doi: 10.1016/j.jpowsour.2018.06.097.
- [11] S. Gao, J. Li, and Z. Lin, 'Theoretical model for surface diffusion driven Ni-particle agglomeration in anode of solid oxide fuel cell', *J. Power Sources*, vol. 255, pp. 144–150, Jun. 2014, doi: 10.1016/j.jpowsour.2014.01.033.
- [12] H.-Y. Chen, 'Simulation of coarsening in three-phase solid oxide fuel cell anodes', *J. Power Sources*, p. 5, 2011.
- [13] M. Trini, S. De Angelis, P. S. Jørgensen, P. V. Hendriksen, K. Thornton, and M. Chen, 'Towards the Validation of a Phase Field Model for Ni Coarsening in Solid Oxide Cells', *Acta Mater.*, p. 116887, Apr. 2021, doi: 10.1016/j.actamat.2021.116887.
- [14] Y. Wang, C. Wu, Q. Du, M. Ni, K. Jiao, and B. Zu, 'Morphology and performance evolution of anode microstructure in solid oxide fuel cell: A model-based quantitative analysis', *Appl. Energy Combust. Sci.*, vol. 5, p. 100016, Mar. 2021, doi: 10.1016/j.jaecs.2020.100016.
- [15] J. W. Cahn and J. E. Hilliard, 'Free Energy of a Nonuniform System. I. Interfacial Free Energy', *J. Chem. Phys.*, vol. 28, pp. 258–267, 1958.
- [16] Y. Wang, C. Wu, B. Zu, M. Han, Q. Du, M. Ni and K. Jiao, 'Ni migration of Ni-YSZ electrode in solid oxide electrolysis cell: An integrated model study', *J. Power Sources*, vol. 516, p. 230660, Dec. 2021, doi: 10.1016/j.jpowsour.2021.230660.

- [17] Y. Lei, Y. Lee, W. Epting, J. Mason, T. Cheng, H. Abernathy, G. Hackett and Y. Wen, 'Modeling Ni redistribution in the hydrogen electrode of solid oxide cells through Ni(OH)<sub>2</sub> diffusion and Ni-YSZ wettability change', *J. Power Sources*, vol. 545, p. 231924, Oct. 2022, doi: 10.1016/j.jpowsour.2022.231924.
- [18] M. Trini, A. Hauch, S. De Angelis, X. Tong, P. V. Hendriksen, and M. Chen, 'Comparison of microstructural evolution of fuel electrodes in solid oxide fuel cells and electrolysis cells', *J. Power Sources*, vol. 450, p. 227599, Feb. 2020, doi: 10.1016/j.jpowsour.2019.227599.
- [19] T.-L. Cheng, Y. Lei, Y. Chen, Y. Fan, H. Abernathy, X. Song and Y.-H. Wen, 'Oxidation of nickel in solid oxide cells during electrochemical operation: Experimental evidence, theoretical analysis, and an alternative hypothesis on the nickel migration', *J. Power Sources*, vol. 569, p. 232991, Jun. 2023, doi: 10.1016/j.jpowsour.2023.232991.
- [20] H.-Y. Chen, H.-C. Yu, J. Scott Cronin, J. R. Wilson, S. A. Barnett, and K. Thornton, 'Simulation of coarsening in three-phase solid oxide fuel cell anodes', *J. Power Sources*, vol. 196, no. 3, pp. 1333–1337, Feb. 2011, doi: 10.1016/j.jpowsour.2010.08.010.
- [21] X. Mantzouris, N. Zouvelou, D. Skarmoutsos, P. Nikolopoulos, and F. Tietz, 'Interfacial properties and structure stability of Ni/Y<sub>2</sub>O<sub>3</sub>-ZrO<sub>2</sub>-TiO<sub>2</sub> cermet anodes for solid oxide fuel cells', *J. Mater. Sci.*, vol. 40, no. 9–10, pp. 2471–2475, May 2005, doi: 10.1007/s10853-005-1977-9.
- [22] D. Prokoshkina, V. A. Esin, G. Wilde, and S. V. Divinski, 'Grain boundary width, energy and self-diffusion in nickel: Effect of material purity', *Acta Mater.*, vol. 61, no. 14, pp. 5188–5197, Aug. 2013, doi: 10.1016/j.actamat.2013.05.010.
- [23] J. M. Blakely and H. Mykura, 'Surface self diffusion measurements on nickel by the mass transfer method', *Acta Metall.*, vol. 9, no. 1, pp. 23–31, Jan. 1961, doi: 10.1016/0001-6160(61)90034-7.
- [24] Y. Lei, W. Epting, J. Masson, T. Cheng, H. Abernathy, G. Hackett and Y. Wen, 'Simulating Microstructure Evolution in Ni-YSZ Electrodes of Solid Oxide Cells Under Operating Conditions', in *TMS 2022 151st Annual Meeting & Exhibition Supplemental Proceedings*, The Minerals, Metals & Materials Society, Ed., in The Minerals, Metals & Materials Series. , Cham: Springer International Publishing, 2022, pp. 457–469. doi: 10.1007/978-3-030-92381-5\_42.
- [25] F. Monaco, M. Hubert, J. Vulliet, J.P. Ouweltjes, D. Montinaro, P. Cloetens, P. Piccardo, F. Lefebvre-Joud and J. Laurencin, 'Degradation of Ni-YSZ Electrodes in Solid Oxide Cells: Impact of Polarization and Initial Microstructure on the Ni Evolution', *J. Electrochem. Soc.*, vol. 166, no. 15, pp. F1229–F1242, 2019, doi: 10.1149/2.1261915jes.
- [26] M. Chen, Y.-L. Liu, J. J. Bentzen, W. Zhang, X. Sun, A. Hauch, Y. Tao, J. R. Bowen and P. V. Hendriksen, 'Microstructural Degradation of Ni/YSZ Electrodes in Solid Oxide Electrolysis Cells under High Current', *J. Electrochem. Soc.*, vol. 160, no. 8, pp. F883–F891, 2013, doi: 10.1149/2.098308jes.
- [27] A. Hauch, S. D. Ebbesen, S. H. Jensen, and M. Mogensen, 'Solid Oxide Electrolysis Cells: Microstructure and Degradation of the Ni/Yttria-Stabilized Zirconia Electrode', *J. Electrochem. Soc.*, vol. 155, no. 11, p. B1184, 2008, doi: 10.1149/1.2967331.
- [28] H. Parikh, N. Hilli, M. R. De Guire, A. H. Heuer, Z. Liu, and R. Goettler, 'Long-term microstructural changes in solid oxide fuel cell anodes: 3D reconstruction', *J. Am. Ceram. Soc.*, vol. 100, no. 4, pp. 1653–1660, Apr. 2017, doi: 10.1111/jace.14659.
- [29] M. B. Mogensen, M. Chen, H. L. Frandsen, C. Graves, A. Hauch, P. V. Hendriksen, T. Jacobsen, S. H. Jensen, T. L. Skafte and X. Sun, 'Ni migration in solid oxide cell electrodes: Review and revised hypothesis', *Fuel Cells*, p. fuce.202100072, Sep. 2021, doi: 10.1002/fuce.202100072.
- [30] Z. Jiao, E. P. Busso, and N. Shikazono, 'Influence of Polarization on the Morphological Changes of Nickel in Fuel Electrodes of Solid Oxide Cells', *J. Electrochem. Soc.*, vol. 167, no. 2, p. 024516, Feb. 2020, doi: 10.1149/1945-7111/ab6f5b.
- [31] A. Hauch, T. L. Skafte, R. Küngas, M. L. Traulsen, S. H. Jensen, (Eds. E. Ivers-Tiffée, A. Weber), 'Proc. 13th European SOFC & SOE Forum', Lucerne, Switzerland, 2018.
- [32] M. Yu, X. Sun, Y. Liu, Y. Shang, M. Chen, 'Electrochemical performance of solid oxide cells operated in CO<sub>2</sub> electrolysis', Lucerne, Switzerland, 2022.

## 5. Conclusions and perspectives

### Conclusions

The present work has been devoted to study the Ni migration in the Ni/YSZ electrode. For this purpose, a coupled experimental and modeling approach has been adopted. In particular, this thesis allowed investigating a new mechanism for the Ni migration, based on the impact of the electrode overpotential and the oxygen vacancies in the electrochemical double layer on the Ni wettability onto YSZ.

In this frame, a dedicated series of tests has been carried out to assess the impact of the operating conditions on the degradations and more specifically on the evolution of the Ni microstructure. Using a specific test bench, the initial performances have been checked in order to ensure a similar starting point for all the experiments. Through a dedicated protocol, the effects of the operating temperature, the ageing time and the operating mode have been studied. More specifically, the impact of temperature has been evaluated with three tests of 2000h conducted in SOEC mode at 750°C, 800°C and 850°C, at high current density ( $-1 \text{ A.cm}^{-2}$ ). Then the effect of the ageing time on the microstructure has been investigated with long-term tests of 1000h to 5000h in electrolysis mode at 800°C and high current density ( $-1 \text{ A.cm}^{-2}$ ). Finally, the difference between both SOEC/SOFC operating modes has been verified with an additional test performed in SOFC mode for 2000h at 800°C and  $1 \text{ A.cm}^{-2}$ . The electrochemical results acquired before and after tests have shown that the 'apparent' voltage degradation rate decreases when both operating temperature and ageing time increase. However, it has been found that the 'intrinsic' degradation rates measured at a reference condition before and after the durability experiments increase with temperature and decrease with time. The analysis of the evolution of the EIS has shown a substantial increase in the ohmic resistance as well as the polarization resistance at high frequencies in electrolysis mode. This increase is enhanced with increasing the temperature and tends to slow down with the time. The evolution of the ohmic resistance seems to stabilize after about 1000h ageing. On the contrary, the test in fuel cell mode has only revealed a slight increase of the ohmic resistance even though a strong increase in the high frequency resistance was still observed.

Besides, a multi-scale electrochemical model, validated for the cells used in this work has allowed identifying the three contributions in the impedance spectra. Indeed, the low frequency arc has been related to the gas conversion in the cermet support. The contribution at medium frequencies has been associated to the electrochemical and transport processes in the active layer of the oxygen electrode along with the gas diffusion in the cell support, whereas the contribution at high frequencies is mainly due to the processes in the active layer of the hydrogen electrode. Therefore, it has been shown that the

increase in the ohmic losses is mostly attributed to the Ni depletion while the increase of the high frequency arc is related to both Ni agglomeration and migration. Conversely, the degradation of the oxygen electrode seems to remain limited. In addition to the electrochemical analyses, post-mortem characterizations have been performed in order to study and quantify the evolution of the cermet microstructure. The post-test characterizations were composed of 2D analyses with SEM images as well as EDX analyses and FIB-SEM reconstructions for the 3D analysis. In addition, the evolution of the microstructural properties extracted from the 3D volumes has also been studied via a set of numerical tools to get all the relevant microstructural properties. From this analysis, a strong Ni depletion as well as Ni agglomeration at the electrolyte interface have been confirmed for the cells aged in electrolysis mode. Additionally, the rate of the Ni depletion at the electrolyte interface in SOEC mode was increasing with the operating temperature from 750 °C to 850 °C whereas it can be supposed that the rate of Ni depletion tends to slow down over long-time operation. On the other hand, only significant Ni agglomeration has been detected for the cell aged in fuel cell mode.

To interpret the experimental results, a numerical model based on the phase field theory has been built and coupled with a multi-scale electrochemical model to simulate the Ni microstructural evolution according to the proposed mechanism. This mechanism takes into account the effect of the electrode overpotential and the oxygen vacancies in the electrochemical double layer through the Ni wettability on YSZ. In this mechanism, the overpotentials in the electrode lead to a gradient in Ni/YSZ contact angle that drives the Ni migration from low wettability to high wettability regions (i.e. from high to low Ni/YSZ contact angles). The multi-scale electrochemical model has been used to predict the cell performances used in this work. This electrochemical model was able to estimate the gradient of Ni/YSZ contact angle as a function of the electrode thickness in the conditions of the long-term tests. This gradient was used as boundary conditions in the phase field model to simulate the microstructural evolution. The phase-field model has been first validated on a simplified microstructure before being applied to a 'real' 3D cermet reconstruction. To assess the relevance of the proposed mechanism, simulations in both SOEC and SOFC modes at respectively  $\pm 1 \text{ A.cm}^{-2}$ ,  $p_{\text{H}_2}/p_{\text{H}_2\text{O}} = 0.1/0.9$ ,  $p_{\text{H}_2}/p_{\text{H}_2\text{O}} = 0.9/0.1$ ,  $12 \text{ Nml.cm}^{-2}.\text{min}^{-1}$  and 750°C have been carried out. The results have shown that a substantial Ni depletion occurs after an operation of 2000h in SOEC mode whereas only a negligible Ni redistribution with no visible Ni enrichment at the electrolyte interface has been found in reverse conditions in SOFC mode. Deeper investigations including the study of the microstructural properties have shown that the simulated depleted zone has been found in the same range of magnitude than the experimental one (albeit lower). The simulations based on the implemented mechanism are thus consistent with the observations of the cells aged in SOEC and SOFC modes. They are also coherent with the experimental studies (this work and literature),

which have reported a substantial Ni depletion in SOEC mode after a rather short time of ageing and a very moderate enrichment in SOFC mode after a very long operating time.

## Perspectives

In this work, the relevance of a new mechanism to account for the Ni migration in both SOEC and SOFC modes has been studied based on a deterioration of the Ni/YSZ interface via an accumulation of oxygen vacancies in the electrochemical double layer. Even though this mechanism seems to reproduce the experiments, it still needs to be improved. Thanks to this work, it has been demonstrated that a modification of the Ni/YSZ interface is responsible for the decrease in the energy interface leading to the Ni migration. It can be thus claimed that the main hypothesis of this mechanism seems to be validated. Nevertheless, the origin of the change of Ni/YSZ interfacial energy is still questionable. Indeed, even though the evolution is coherent with the change of Ni/YSZ interface energy due to the change in oxygen vacancy concentration, it could be explained by other physico-chemical processes inducing a modification of the Ni/YSZ interface (such as the segregation of impurities under polarization). Furthermore, it is clear that the underlying mechanisms for Ni migration are complex and involve several processes depending on the experimental conditions or tested cermet. Therefore, additional investigations including other long-term tests, post-test characterizations and modelling are still needed to clarify the mechanism.

Indeed, another series of long-term tests should be conducted to first verify the reproducibility of the experiments and confirm the impact of the different operating parameters on the Ni microstructure evolution. Moreover, long-term tests of more than 5000h could be done to check the tendency of the Ni migration to slow-down over time, which remains unclear in this study. Finally, a very long-term test in fuel cell mode could be carried out in order to make sure that Ni tends to slowly accumulate at the hydrogen electrode/electrolyte interface.

The phase-field model validated to simulate the evolution of the Ni migration according to the proposed mechanism will be used to investigate the possible hydrogen electrode optimization that could be done in order to limit the Ni migration. Indeed, the model can be used to investigate the impact of the initial microstructural properties on the rate of the Ni migration as well as the properties of the Ni/YSZ interface (by increasing the value of the Ni/YSZ interface energy and then making stronger the adhesion between the Ni and YSZ). In this frame, the increase of the Ni/YSZ interface energy could be done using a based NiO–TiO<sub>2</sub>–YSZ alloy [1]. Moreover, other solutions such as the replacement of Ni-YSZ by Ni-GDC for the hydrogen electrode could be envisaged.

In addition, the results of the phase-field model will be used as input properties for a 3D electrochemical model, which is capable of predicting the electrochemical data (including the EIS and i-U curves) after degradation. Therefore, the phase-field model should be a powerful tool that can be used as a diagnostic tool to predict the impact of Ni microstructure evolution and especially the Ni migration on the overall cell performances.

In conclusion, a deeper and more detailed study of the complex Solid Oxide Cell technology can only be achieved by adopting a threefold methodology consisting of electrochemical experiments, microstructural characterizations and multi-scale as well as multi-physics modeling tools. In this case, relevant and efficient improvements of the Solid Oxide Cell could be achieved to fully deploy this technology in our future carbon neutral society.

[1] A. Tsoga, A. Naoumidis, and P. Nikolopoulos, 'WETTABILITY AND INTERFACIAL REACTIONS IN THE SYSTEMS Ni/YSZ and Ni/Ti-TiO<sub>2</sub>/YSZ', *Acta mater.*, Vol. 44. No. 9, pp. 3679-3692, 1996.

# APPENDIX A

## 1. First-order phase transition in Landau's theory

A first-order phase transition is from a physical point of view a transformation of the system caused by the variation of a particular external parameter (e.g. temperature, magnetic field, etc.). This transition takes place when the parameter reaches a critical threshold (e.g. melting point for a solid to liquid transition or the vaporization as illustrated in Figure 1-1). Such a first-order phase transition can be described by Landau's theory [1].

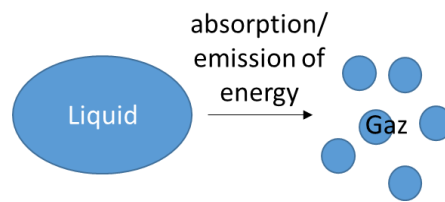
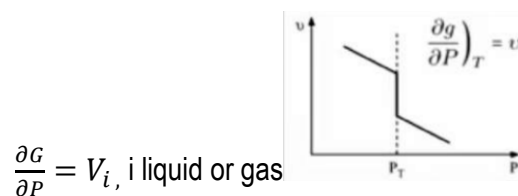


Figure 1-1: Illustration of a classical phase transition (vaporisation).

From a mathematical point of view, the first order transitions are those for which the first derivative of the free energy with respect to one of the thermodynamic variables is discontinuous. The solid/liquid/gas transitions are thus first-order transitions. Indeed, the derivative of the free energy with respect to pressure instance is equal to the volume which presents a discontinuity during the transition Figure 1-2.



$$\frac{\partial G}{\partial P} = V_i, \text{ i liquid or gas}$$

Figure 1-2: Illustration of the derivative of the free energy.

As energy cannot be transferred instantaneously between all the system and its environment, the first-order transition cannot arise at the same time. For this reason, the system is heterogeneous (e.g. when water boils, the water is not instantaneously transformed into a steam but forms a turbulent mixture of liquid water and vapor bubbles).

## 2. Fundamentals of the phase-field modeling

The objective of the phase-field modeling is to describe the evolution of moving interfaces and free surfaces, separating 2 thermodynamic phases during phase transition. This method is based on non-equilibrium thermodynamics and Landau's theory of phase transitions. Each phase of the physical system is described by a so-called phase-field variable  $\phi$ , which is related to an order parameter according to Landau's theory. Indeed, an order parameter is a parameter that characterizes the state of a physical system during a phase transition.

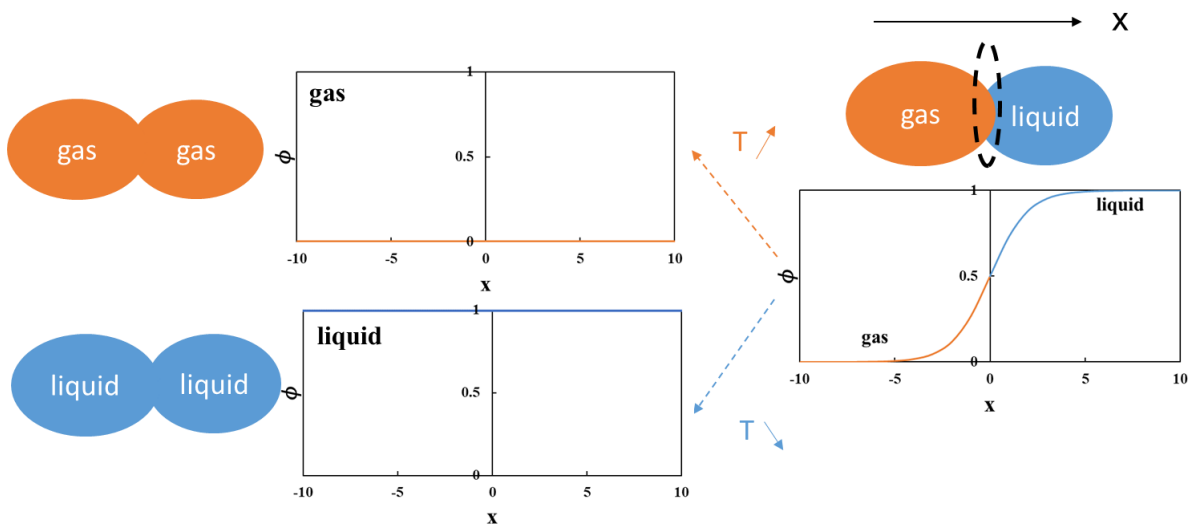


Figure 1-3: Description of the diffuse interface with the phase-field variable  $\phi(x, t)$ .

In phase field theory,  $\phi(x, t)$  locally describes the state of the material thus depends on time  $t$  and space  $x$ . In the high temperature stable disordered phase (gas for example), the phase-field variable  $\phi$  is equal to 0 and in the low temperature stable ordered phase (liquid for example)  $\phi$  is equal to 1. The microscopically abrupt interface is treated as a diffuse zone with a smooth evolution of the phase variable as shown in Figure 1-3. The free energy of the system  $G(x, t)$  is written as a function of the phase-field variable  $\phi(x, t)$ , its spatial derivatives  $\partial_x \phi$  and position  $x$   $G(x, t) = f(\phi, \partial_x \phi, x)$ .

There is an evolution of the system over the time when the system tends towards the equilibrium (that is to say when there is a decrease in the total free energy of the system). In other words, the equilibrium is reached after minimizing  $G$ :  $\delta G(x, t) = 0$ . In the phase-field model, the objective is to determine the variable  $\phi$  which locally allows minimizing the free energy under the application of an external field (temperature, electric field, stress...).

### 3. Allen-Cahn equation

#### 3.1 Expression of the energy functional

The geometric evolution of the interface during a phase transition is described by the so-called Allen-Cahn equation. In order to describe the evolution of the system, the free energy of the system is associated to an energy functional. A classical energy functional characterizing the system is expressed as follows:

$$G[\phi, \partial_x \phi, x] = F[\phi, \partial_x \phi, x] = \int_x [w g(\phi) + \frac{\epsilon^2}{2} |\partial_x \phi|^2] dx \quad 1-1$$

The minimization of  $F$  is related to the combined minimization of both terms of eq. (1). The second term,  $\frac{\epsilon^2}{2} |\nabla \phi|^2$ , allows the interface to be described continuously (where  $\epsilon$  is referred as the gradient term) by taking continuous values between  $]0,1[$  as shown in Figure 1-4.

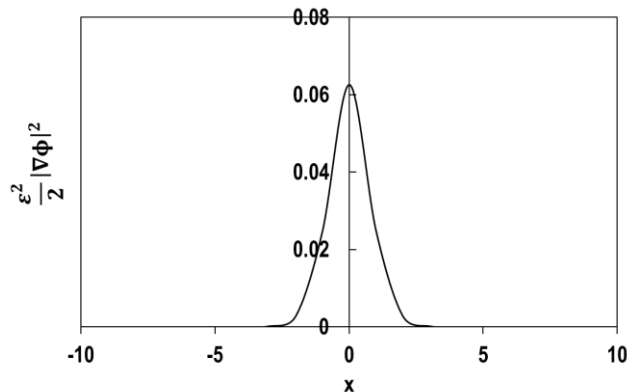


Figure 1-4: Plot of the gradient term of the energy functional as a function of the position  $x$  across the diffuse interface.

The minimization of this term allows reducing as much as possible the number of interfaces in the system as illustrated in Figure 1-5.

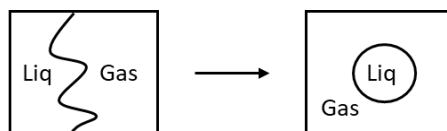


Figure 1-5: Illustration of the minimization of the second term of the energy functional by reducing the number of interfaces.

The term  $wg(\phi)$  represents the free energy density of the system (bulk description) which represents the energy barrier to pass from one phase (for example gas ( $\phi = 0$ )) to another one (liquid ( $\phi = 1$ )): Figure 1-6).

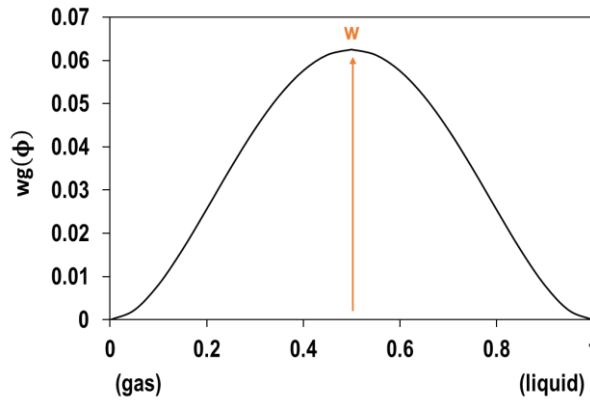


Figure 1-6: Plot of the free energy density of the system as a function of the phase-field variable.

$g(\phi)$  is a double-well potential expressed as  $g(\phi) = \phi^2(1 - \phi)^2$  and  $w$  is the height of the barrier. Then, if considering a gas to liquid transition,  $wg(\phi)$  is the energy barrier to pass from gas ( $\phi = 0$ ) to liquid ( $\phi = 1$ ) (cf. Figure 1-6). The shape of this double-well function will control the phase transition as illustrated in Figure 1-7.

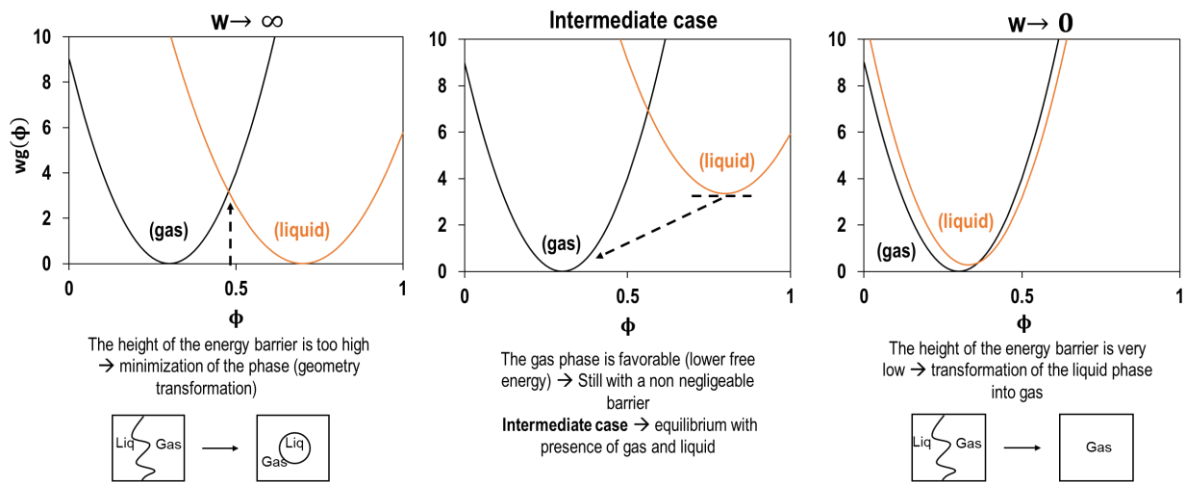


Figure 1-7: Plot of the energy barrier in different cases as a function of the phase-field variable  
 (a) there is no transition and only the interface length between solid and gas is minimized according to the gradient term of eq. (1). (b) there is a transition towards a new equilibrium between the solid and gas phases  
 (c) there is a vaporization.

### 3.2 Minimization of the energy functional at equilibrium

$\delta F[\phi, \partial_x \phi, x] = 0$  to obtain the stationary profile  $\phi(x)$

$$F[\phi, \partial_x \phi, x] = \int_x f(\phi, \partial_x \phi) dx \text{ with } f(\phi, \partial_x \phi) = w g(\phi) + \frac{\varepsilon^2}{2} |\partial_x \phi|^2 \quad 1-2$$

The equilibrium condition imposes that:  $\delta F = 0$ . The term  $\delta F$  is expressed as follows:

$$\delta F = F[\phi + \delta\phi, \partial_x \phi + \delta[\partial_x \phi], x] - F[\phi, \partial_x \phi, x] \quad 1-3$$

$$\begin{cases} F[\phi; \partial_x \phi; x] = \int_x f(\phi; \partial_x \phi) dx \\ F[\phi + \delta\phi; \partial_x \phi + \delta[\partial_x \phi]; x] = \int_x f(\phi + \delta\phi; \partial_x \phi + \delta[\partial_x \phi]) dx \end{cases} \quad 1-4$$

$$\delta f = \frac{\partial f}{\partial \phi} \delta\phi + \frac{\partial f}{\partial(\partial_x \phi)} \delta[\partial_x \phi] \quad 1-5$$

$$\text{So, } \delta F = \int_x \frac{\partial f}{\partial \phi} \delta\phi + \frac{\partial f}{\partial(\partial_x \phi)} \delta[\partial_x \phi] dx \quad 1-6$$

Integration by parts of the second term of  $\delta F$ :

$$\begin{cases} u' = \delta[\partial_x \phi] \text{ and } u = \delta\phi \\ v = \frac{\partial f}{\partial(\partial_x \phi)} \text{ and } v' = \frac{d}{dx} \left[ \frac{\partial f}{\partial(\partial_x \phi)} \right] \end{cases} \quad 1-7$$

$$\text{So, } \int_x \frac{\partial f}{\partial(\partial_x \phi)} \delta[\partial_x \phi] dx = \left[ \frac{\partial f}{\partial(\partial_x \phi)} \delta\phi \right]_{x1}^{x2} - \int_{x1}^{x2} \frac{d}{dx} \left[ \frac{\partial f}{\partial(\partial_x \phi)} \right] \delta\phi dx \quad 1-8$$

$$\text{Then, } \delta F = \int_x \left[ \frac{\partial f}{\partial \phi} \delta\phi - \frac{d}{dx} \left[ \frac{\partial f}{\partial(\partial_x \phi)} \right] \delta\phi \right] dx \quad 1-9$$

According to the equilibrium condition:  $\delta F = 0$ , the Euler-Lagrange equation is given by:

$$\frac{\partial f(\phi)}{\partial \phi} - \frac{d}{dx} \left[ \frac{\partial f}{\partial(\partial_x \phi)} \right] = 0 \quad 1-10$$

$$\left\{ \begin{array}{l} \frac{\partial f}{\partial \phi} = \frac{\partial w g(\phi)}{\partial \phi} = \frac{\partial w \phi^2 (1 - \phi)^2}{\partial \phi} = w(2\phi - 6\phi^2 + 4\phi^3) = w2\phi(1 - \phi)(1 - 2\phi) \\ \text{and } \frac{d}{dx} \left[ \frac{\partial f}{\partial (\partial_x \phi)} \right] = \frac{d}{dx} \left[ \frac{\partial \left( \frac{\varepsilon^2}{2} |\partial_x \phi|^2 \right)}{\partial (\partial_x \phi)} \right] = \frac{d}{dx} (\varepsilon^2 |\partial_x \phi|) = \varepsilon^2 \frac{\partial^2 \phi}{\partial x^2} \end{array} \right. \quad 1-11$$

We obtain the following equation in the stationary case:

$$\frac{\partial w g(\phi)}{\partial \phi} = \varepsilon^2 \frac{\partial^2 \phi}{\partial x^2} \quad 1-12$$

The stationary profile of the phase field variable  $\phi(x)$  is obtained using this equation:

$$w \frac{dg}{d\phi} \frac{d\phi}{dx} = \varepsilon^2 \frac{\partial^2 \phi}{\partial x^2} \frac{d\phi}{dx} = \frac{\varepsilon^2}{2} \frac{\partial}{\partial x} \left[ \left( \frac{d\phi}{dx} \right)^2 \right] \quad 1-13$$

Integration from  $-\infty$  to  $x$ :

$$\int_{-\infty}^x w \frac{dg(\phi)}{d\phi} \frac{d(\phi)}{dx'} dx' = \int_{-\infty}^x \frac{\varepsilon^2}{2} \frac{\partial}{\partial x'} \left( \frac{d\phi}{dx'} \right)^2 dx' \quad 1-14$$

$$w(g(\phi(x)) - g(\phi(x = -\infty))) - \left[ \frac{\varepsilon^2}{2} \left( \frac{d\phi}{dx} \right)^2 \right]_{-\infty}^x = 0 \quad 1-15$$

Boundary conditions:

$$\left\{ \begin{array}{l} g(\phi(x = -\infty)) = 0 \text{ since } \phi(x = -\infty) = 0 \text{ and } g(0) = 0 \\ \left( \frac{d\phi}{dx} \right)_{-\infty} = 0 \end{array} \right. \quad 1-16$$

$$w\phi^2(1 - \phi)^2 = \frac{\varepsilon^2}{2} \left( \frac{d\phi}{dx} \right)^2 \quad 1-17$$

$$\phi(1 - \phi) = \frac{\varepsilon}{\sqrt{2w}} \frac{d\phi}{dx} \quad 1-18$$

We introduce the tem  $\delta = \frac{4\varepsilon}{\sqrt{2w}}$  so that :

$$\frac{d\phi}{\phi(1 - \phi)} = 4 \frac{dx}{\delta} \quad 1-19$$

$$\frac{d\phi}{\phi(1-\phi)} = 4 \frac{dx}{\delta} \quad 1-20$$

$$\int \frac{1}{\phi(1-\phi)} d\phi = \int 4 \frac{dx}{\delta} \quad 1-21$$

$$\int \frac{1}{\phi} + \frac{1}{1-\phi} d\phi = \int 4 \frac{dx}{\delta} \text{ and } \tanh(z) = \frac{1-e^{-2z}}{1+e^{-2z}} \quad 1-22$$

$$\int \frac{1}{\phi} + \frac{1}{1-\phi} d\phi = \int 4 \frac{dx}{\delta} \text{ and } \tanh(z) = \frac{1-e^{-2z}}{1+e^{-2z}} \quad 1-23$$

$$\ln|\phi| - \ln|1-\phi| = \frac{4}{\delta}x + c \quad 1-24$$

$$\ln \left| \frac{\phi}{1-\phi} \right| = \frac{4}{\delta}x + c \quad 1-25$$

$$\frac{\phi}{1-\phi} = e^{\frac{4}{\delta}x+c} \quad 1-26$$

$$\phi = \frac{e^{\frac{4}{\delta}x+c}}{1 + e^{\frac{4}{\delta}x+c}} = \frac{1}{e^{-\frac{4}{\delta}x+c} + 1} \quad 1-27$$

$$\phi(x) = \frac{1}{2} \left( 1 + \tanh \left( \frac{2x}{\delta} \right) \right) \quad 1-28$$

Where  $2\delta$  is the thickness of the phase field (Figure 1-8).

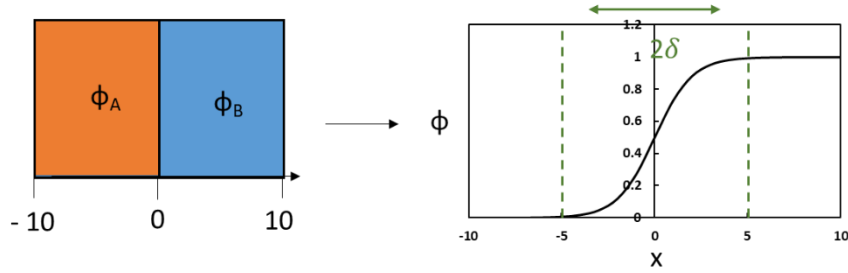


Figure 1-8: Description and plot of the smooth interface.

### 3.3 Demonstration of the Allen-Cahn equation

The Allen-Cahn equation allows describing the temporal evolution of the phase field variable up to reach the equilibrium given by equation 1-12. In this geometric description of the interface, it can be noted that it is not necessary to consider the mass conservation.

According to equation 1-1:

$$\frac{dF}{dt} = \int_v \frac{\partial}{\partial t} (wg(\phi) + \frac{\varepsilon^2}{2} |\nabla\phi|^2) dv = \int_v \frac{\partial wg(\phi)}{\partial \phi} \frac{\partial \phi}{\partial t} + \varepsilon^2 |\nabla\phi| \cdot \nabla \frac{\partial \phi}{\partial t} dv \quad 1-29$$

$$\text{Property } \nabla \cdot \left( \frac{\partial \phi}{\partial t} \nabla \phi \right) = \nabla \phi \cdot \nabla \frac{\partial \phi}{\partial t} + \frac{\partial \phi}{\partial t} \nabla \cdot \nabla \phi \quad 1-30$$

$$\frac{dF}{dt} = \int_v \frac{\partial wg(\phi)}{\partial \phi} \frac{\partial \phi}{\partial t} + \varepsilon^2 \left( \nabla \cdot \left( \frac{\partial \phi}{\partial t} \nabla \phi \right) - \frac{\partial \phi}{\partial t} \nabla \cdot \nabla \phi \right) dv \quad 1-31$$

According to the divergence theorem:

$$\iiint_v \nabla \cdot \vec{T} \cdot d\vec{s} = \iint_s \vec{T} \cdot \vec{ds} \text{ with } \vec{T} = \left( \frac{\partial \phi}{\partial t} \nabla \phi \right) \quad 1-32$$

$$\text{So, } \int_v \nabla \cdot \left( \frac{\partial \phi}{\partial t} \nabla \phi \right) dv = \int_s \left( \frac{\partial \phi}{\partial t} \nabla \phi \right) \cdot \vec{nds} \quad 1-33$$

$$\frac{dF}{dt} = \int_v \left( \frac{\partial wg(\phi)}{\partial \phi} \frac{\partial \phi}{\partial t} - \varepsilon^2 \frac{\partial \phi}{\partial t} \nabla \cdot \nabla \phi \right) dv + \int_s \varepsilon^2 \left( \frac{\partial \phi}{\partial t} \nabla \phi \cdot \vec{n} \right) d\vec{s} \quad 1-34$$

The differential of the free energy gives:

$$dF = dU - TdS \quad 1-35$$

$$\frac{dF}{dt} = P_{\text{ext}} - T \frac{dS}{dt} \quad 1-36$$

With,

$$P_{\text{ext}} = \int_s \varepsilon^2 \left( \frac{\partial \phi}{\partial t} \bar{\nabla} \phi \cdot \bar{n} \right) \bar{d}s \quad 1-37$$

$$-T \frac{dS}{dt} = \int_v \left( \frac{\partial \text{wg}(\phi)}{\partial \phi} \frac{\partial \phi}{\partial t} - \varepsilon^2 \frac{\partial \phi}{\partial t} \bar{\nabla} \cdot \bar{\nabla} \phi \right) dv \quad 1-38$$

Thermodynamics Second Principle:  $\frac{dS}{dt} \geq 0$

For a system closed at T constant:

$$\int_v - \frac{\partial \text{wg}(\phi)}{\partial \phi} \frac{\partial \phi}{\partial t} + \varepsilon^2 \frac{\partial \phi}{\partial t} \bar{\nabla} \cdot \bar{\nabla} \phi dv \geq 0 \quad 1-39$$

$$\frac{\partial \phi}{\partial t} \left( - \frac{\partial \text{wg}(\phi)}{\partial \phi} + \varepsilon^2 \bar{\nabla} \cdot \bar{\nabla} \phi \right) \geq 0 \quad 1-40$$

$$\frac{\partial \phi}{\partial t} = -L \left( \frac{\partial \text{wg}(\phi)}{\partial \phi} - \varepsilon^2 \bar{\nabla} \cdot \bar{\nabla} \phi \right) \quad 1-41$$

A positive factor is introduced, L the mobility, to verify this equation.

The Allen-Cahn equation is then deduced:

$$\frac{\partial \phi}{\partial t} = -L \left[ \frac{\partial \text{wg}(\phi^2(1-\phi)^2)}{\partial \phi} - \varepsilon^2 \frac{\partial^2 \phi}{\partial x^2} \right] \quad 1-42$$

It can be noted that this equation reduces to the stationary case at equilibrium equation 1-12 when  $\frac{\partial \phi}{\partial t} = 0$ .

### 3.4 Determination of the interfacial energy

To determine interfacial energy  $\sigma$ ,  $f(\phi)$  is integrated knowing that  $g(\phi) = \phi^2(1-\phi)^2$  does not contain a bulk contribution (in this case, it is not necessary to remove a bulk contribution):

$$\sigma = \int_{-\infty}^{+\infty} f dx = \int_{-\infty}^{+\infty} \left[ \text{wg}(\phi) + \frac{\varepsilon^2}{2} \left( \frac{d\phi}{dx} \right)^2 \right] dx \quad 1-43$$

With  $wg(\phi) = \frac{\varepsilon^2}{2} \left( \frac{d\phi}{dx} \right)^2$  (cf. equation 1-17)),  $\sigma$  is given by:

$$\sigma = \int_{-\infty}^{+\infty} \left( \frac{\varepsilon^2}{2} \left( \frac{d\phi}{dx} \right)^2 + \frac{\varepsilon^2}{2} \left( \frac{d\phi}{dx} \right)^2 \right) dx \rightarrow \int_0^1 \left( \varepsilon^2 \left( \frac{d\phi}{dx} \right)^2 \right) d\phi \quad 1-44$$

Change of variable:

$$\begin{cases} x = +\infty \rightarrow \phi = 1 \\ x = -\infty \rightarrow \phi = 0 \end{cases} \quad 1-45$$

Using equation 1-27, we obtain:

$$\sigma = \int_0^1 \varepsilon^2 \left( \frac{4}{\delta} \phi(1 - \phi) \right) d\phi \quad 1-46$$

$$\sigma = \left[ \frac{4\varepsilon^2}{\delta} \left( \frac{\phi^2}{2} - \frac{\phi^3}{3} \right) \right]_0^1 \quad 1-47$$

We define the barrier of energy as function of  $\sigma$  and  $\delta$  according to:

$$w = \frac{12\sigma}{\delta} \quad 1-48$$

In this condition, the interfacial energy is given by:

$$\sigma = \frac{\varepsilon\sqrt{2w}}{6} \quad 1-49$$

IV) Allen-Cahn and Cahn-Hilliard equations: Focus on the two temporal and spatial equations to have the evolution of  $\phi$  :

- a) Case Allen-Cahn: To describe a phase transformation such as liquid and gas composed of one chemical element  $\rightarrow$  The resolution of Allen-Cahn equation is sufficient to get the temporal and spatial evolution of  $\phi$ .

- b) Case Cahn-Hilliard: To describe the interdiffusion phenomena between two materials with different elements without phase transformation → The Cahn-Hilliard equation only is sufficient to have the temporal and spatial evolution (according to the second Fick's law).
- c) Case Allen-Cahn and Cahn-Hilliard: Need to solve both equations for a phase change and interdiffusion phenomena (ex: in the case of the solidification of an alloy).

### 3.5 Cahn-Hilliard equation

The Cahn-Hilliard equation is associated to a physical description. In order to describe the evolution of the system, we define a functional of energy representative of the system.

To describe the evolution of the system, a classical energy functional characterizing the system is expressed:

$$F[C] = \int_v [wg(C) + \frac{\epsilon^2}{2} |\nabla C|^2] dv \quad 1-50$$

Where  $C$  is the concentration or molar fraction of each species. The term  $wg(C)$  represents the free energy of the system (bulk description), and represents the energy barrier of height  $w$  that must be passed for the interdiffusion. In the volume of each phase, the concentration can vary from  $C = 0$  to  $1$ . If the concentration at equilibrium in the two phases are respectively  $C=0$  and  $C=1$ , then we can express the double-well function as follows:  $g(C) = C^2(1 - C)^2$ .

#### 3.5.1 Demonstration of the Cahn-Hilliard equation

The Cahn-Hilliard equation imposes a mass conservation during change in concentration.

The chemical potential is defined as:  $\mu = \frac{\delta F[C]}{\delta C}$  (Variation of the energy of a thermodynamic system link to the variation of the quantity of this species in the system)

According to the Fick's law:

$$\vec{J} = -M\nabla\mu \text{ and } (M = \text{mobility}) \quad 1-51$$

and mass conservation equation of Fick law:

$$\frac{dC}{dt} = -\nabla \cdot \vec{J} \quad 1-52$$

Then, the expression of the Cahn-Hilliard equation:

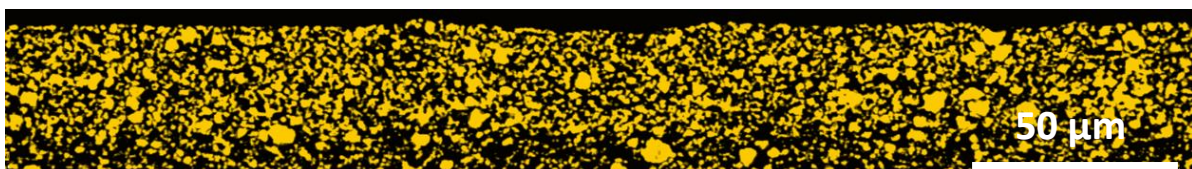
$$\frac{dC}{dt} = \nabla \cdot \left( M \nabla \frac{\delta F[C]}{\delta C} \right)$$

1-53

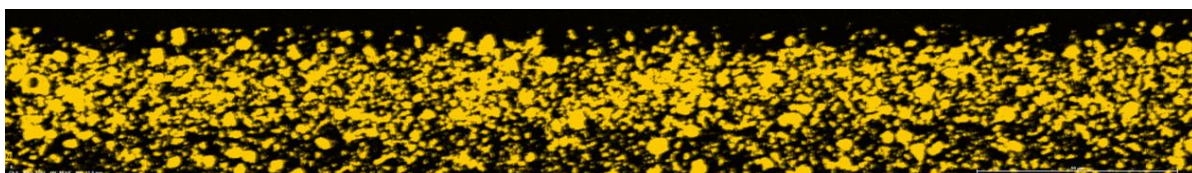
## APPENDIX B

### EDX cartography of the Ni phase for all the different experiments

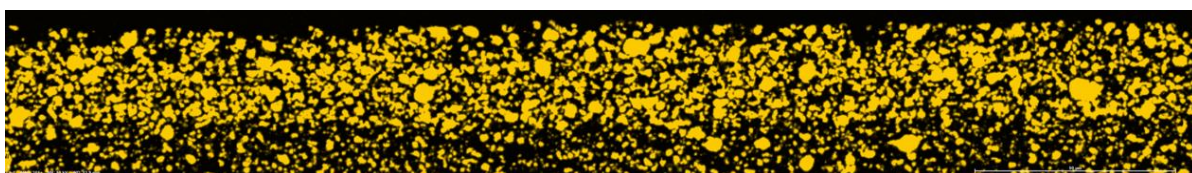
#### Reference



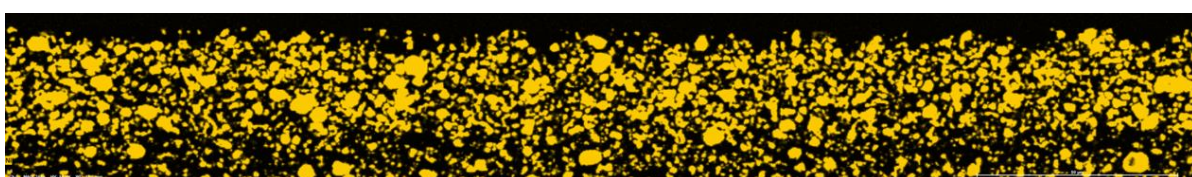
#### 1000h 800°C SOEC



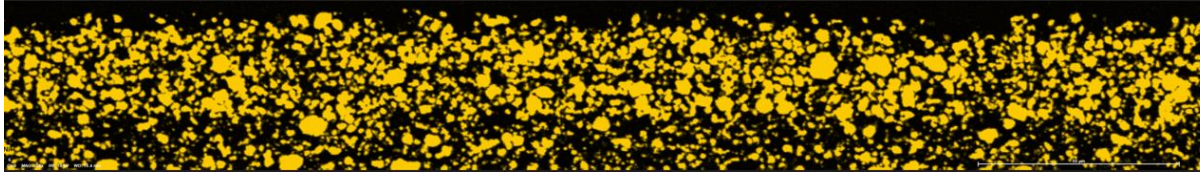
#### 2000h 750°C SOEC



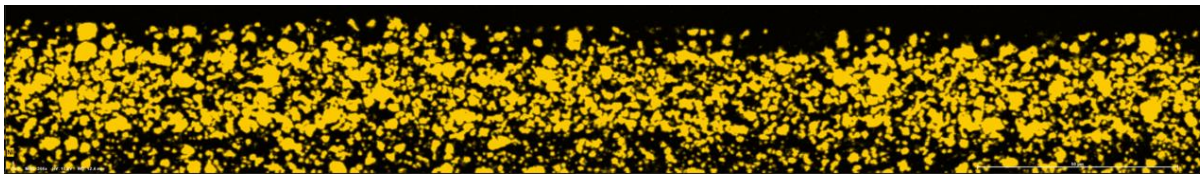
#### 2000h 800°C SOEC



2000h 850°C SOEC



5000h 800°C SOEC



2000h 800°C SOFC

